Thermal stability of nanolayers for EUV optics

Yetik, G.

Publication date
2023
Document Version
Final published version

Thermal stability of nanolayers for EUV optics

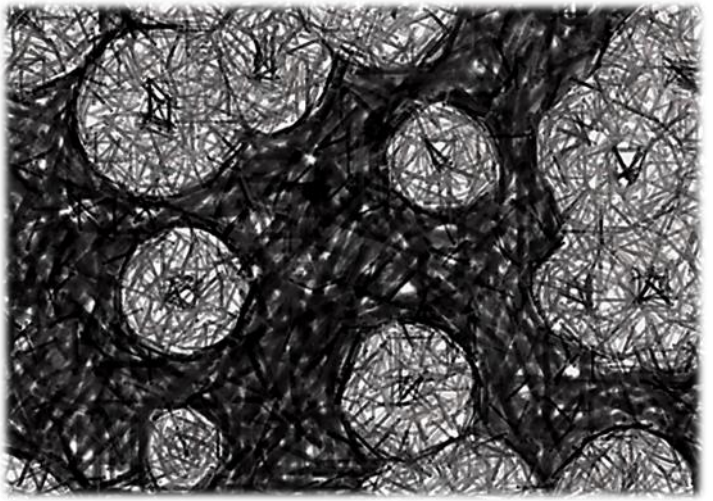

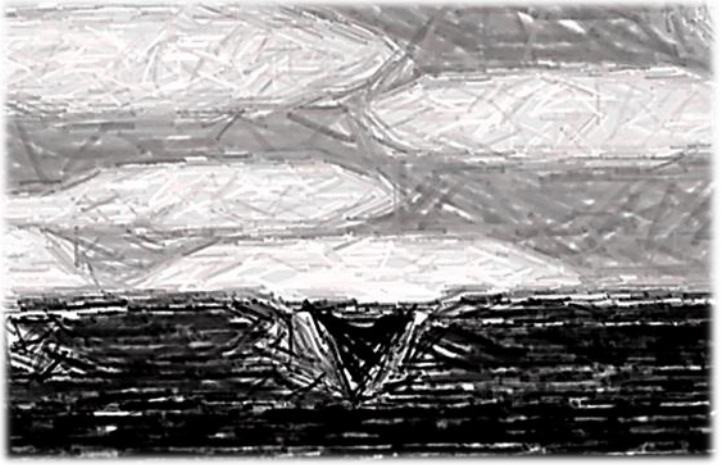

Görsel Yetik

THERMAL STABILITY OF NANOLAYERS FOR EUV OPTICS

Görsel Yetik

Ph.D. Thesis, University of Amsterdam, July 2023

Thermal stability of nanolayers for EUV optics

Görsel Yetik

ISBN: 978-94-6419-852-2

ASML

UNIVERSITEIT VAN AMSTERDAM

This work was carried out at the Advanced Research Center for Nanolithography (ARCNL), a public-private partnership of the University of Amsterdam (UvA), the Vrije Universiteit (VU), the Dutch Research Council (NWO), and semiconductor equipment manufacturer ASML.

Thermal Stability of Nanolayers for EUV Optics

ACADEMISCH PROEFSCHRIFT

ter verkrijging van de graad van doctor
aan de Universiteit van Amsterdam
op gezag van de Rector Magnificus
prof. dr. ir. P.P.C.C. Verbeek
ten overstaan van een door het College voor Promoties ingestelde commissie,
in het openbaar te verdedigen in de Agnietenkapel
op donderdag 6 juli 2023, te 16.00 uur

door
Görsel Yetik
geboren te Diyarbakir

Promotiecommissie

Promotor:	prof. dr. J.W.M. Frenken	Universiteit van Amsterdam
Copromotor:	dr. R. Bliem	Universiteit van Amsterdam
Overige leden:	prof. dr. M.S. Golden	Universiteit van Amsterdam
	dr. A. Isaeva	Universiteit van Amsterdam
	prof. dr. P. Rudolf	Rijksuniversiteit Groningen
	prof. dr. P.C.M. Planken	Universiteit van Amsterdam
	dr. Z.S. Houweling	ASML, Veldhoven

Faculteit der Natuurwetenschappen, Wiskunde en Informatica

CONTENTS

Chapter 1

INTRODUCTION

1.1Thin films

A coating is a layer of a material that covers the surface of an object and that has a thickness that is much smaller than the extension of the layer in the two dimensions parallel to the surface. Generally, coatings are used to introduce functionalities by modifying properties and adding extra ones to a material. Well-known is the coating of materials simply for decorative purposes. Paint layers form one of the first and most used examples of that type of coating. The precise origins of the application of paint are unknown, but what is clear, is that they must be very old. The oldest documented figurative paintings are estimated to be at least 40.000 years old[1–3], which is in the Paleolithic, also known as the old stone age. The non-figurative paintings go back in time even before the habitation of modern humans in Europe[3]. Thinner classes of coatings are nowadays referred to as "thin films". The first known thin metallic films are more than 5000 years old, which puts them in the middle bronze age. They were found in Egyptian tombs as the decorative gilding of death masks, sarcophagi and burial attributes[4]. In time, the types of thin films and their applications have grown into a wide variety and they can be found all around us, making them an essential part of today's products and technology. Common applications of thin metal films are to be found in household mirrors that consist of a glass plate covered at the rear side by a thin reflective metal film, and in the protective layers on touch screens of laptops and smartphones. For many practical applications, thin metal coatings are deposited on objects by straightforward techniques, such as hot-dip galvanizing, thermal spraying, electroplating and sherardizing.

In materials science, a thin film is loosely defined as a layer of material with a thickness of up to several micrometers. In this thesis, I will address the regime also referred to as "ultra-thin films", as most of the films have a thickness smaller than 20 nm. Generally, a cheap inner material covered by a thin film of a more sophisticated or expensive material provides an attractive way to combine the bulk properties of the inner material with the

superior surface properties of the coating. Applications of this approach are essential not only for decorative purposes, but also to obtain superb corrosion resistance[5], to improve electrical conduction[6–8], to reduce friction and enhance wear resistance[9–12], to reach high emissivity for infrared radiation[13,14], and to combine these properties with special optical[15,16], magnetic[17,18] and mechanical behavior[19]. In a growing number of applications, for example in the semiconductor industry, thin metallic films are not primarily used as coatings, but as essential functional device components, e.g. in microchips. In some applications, thin metal films are employed as free-standing membranes, without the support of a substrate[20,21].

Many properties of thin films are dictated or influenced by their internal structure. Thin metallic films usually do not take the form of a single crystal. Instead, most thin metallic films are polycrystalline, i.e. they consist of large numbers of differently-oriented, single-crystalline grains. Together, the grain boundaries that separate the small crystallites, form a network of locations where the perfect crystalline structure is interrupted. These defects make the metal films mechanically vulnerable in comparison with their (hypothetical) single-crystalline counterparts. Grain boundaries can also act as preferred channels for atoms and molecules to invade and traverse the material, so that chemical processes such as oxidation and other forms of corrosion take place not only at the outer surface, but also at the grain boundaries. The grainy micro- and nanostructure of thin metal films often result in surface roughness, simply because each individual grain at the surface of the film tends to evolve towards its own equilibrium shape instead of connecting to the grains that surround it in a flat and atomically smooth configuration[22]. On the small scale, this makes the surface of a polycrystalline film look more like a cobblestone road than a smooth pavement. As we will discuss below, the polycrystalline structure also plays a role in the morphological instabilities that thin films can undergo.

As the surfaces and grain boundaries of thin, polycrystalline films affect many of the film properties, the deposition, structure and evolution of thin films are subjects of intense investigation in materials and surface science. A common and conceptually straightforward method to produce thin metal films is atom-by-atom deposition. In this thesis, we will restrict ourselves to this class of deposition methods, which we will elaborate on in Chapter 3. In relation to the instabilities mentioned above, the film morphology can be affected by the heating of the metal film, even when the temperature is kept far below the melting point of the metal. The extreme surface-to-volume ratio establishes a powerful driving force for morphological changes that can result in extreme consequences, such as dewetting and agglomeration.

In this thesis, I will put a large emphasis on one particular aspect, dewetting. This behavior can be regarded as the opposite of wetting, which is the tendency of one material to

completely cover another material. Instead, in the case of dewetting, the outer material tends to break up. This can be observed on the macroscopic scale, for example when water on a glass window forms droplets instead of a continuous film. For the thin films in this thesis, the dimensions of the 'droplets' are much smaller but the underlying physics is the same. Dewetting turns the film into a collection of separate three-dimensional islands on the substrate, in full equivalence to water droplets on glass. Dewetting can be observed when the temperature is high enough to enable the large amount of atomic motion that is required for these morphological changes; how high the temperature needs to be for a film of a specific material, roughly scales with the material's melting point.

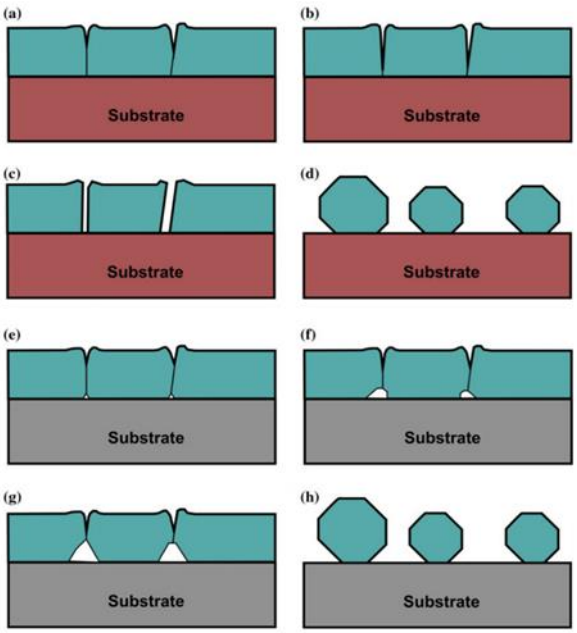

Figure 1.1 *Schematic illustration of a polycrystalline thin film on a substrate. Panels a-d illustrate grain boundary grooving from the surface inwards, whereas e-d demonstrate the same mechanism in combination with the void formation and grain boundary grooving at the interface between the film and the substrate. In both cases, the film no longer covers the substrate in the final configurations, which is referred to as 'dewetting'. Reprinted from Ref. 23.*

Like most other diffusion phenomena, dewetting is a thermally activated process. It is active already at and below room temperature, albeit that it may proceed so slowly at those temperatures that it escapes the observation. In a number of cases, dewetting can already take place during the deposition of a thin film, as a direct consequence of the mobility that the deposition process itself introduces. For the physical vapor deposition (PVD) process that is often used for the ultrathin films that are under investigation in this thesis, the transient mobilities of the arriving atoms correspond to typical migration distances below one nanometer, which are sufficiently short not to enable the films to dewet already during the deposition stage.

In order to understand the wetting properties of thin films, we need to inspect them from a thermodynamic perspective. Driving the wetting or dewetting is the reduction of the total surface and interface free energy of the film-plus-substrate system. The surface free energy quantifies the free-energy investment that is required to form a unit area of that surface out of a continuous, three-dimensional bulk arrangement of the same material. This accounts for the loss of interatomic or intermolecular interactions across the interface, which may be partly compensated by rearrangements at and close to the surface. Nevertheless, for most materials, the surfaces and interfaces come with positive free energies, which means that the materials tend to minimize the areas of their surfaces and interfaces.

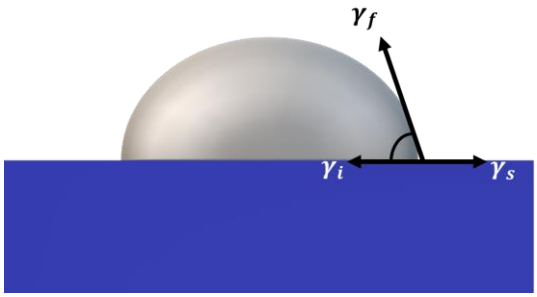

Figure 1.2 *The equilibrium shape of a material that covers a substrate incompletely, with a contact angle $\vartheta>0$, corresponding to dewetting, as described by the Young-Laplace equation.*

Energy minimization of a thin film on a solid substrate leads to the Young-Laplace equation[24].

$$\gamma_s = \gamma_i + \gamma_f \cos\theta\,, \quad (1.1)$$

where γ_s, γ_f and γ_i are free energies per unit area of the surface of the substrate material, the surface of the thin film material and their interface, respectively, and θ is the equilibrium contact angle (Fig 1.2). When $\theta > 0$, the equilibrium solution corresponds to a geometry with incomplete coverage of the substrate by the overlayer or, in other words, to dewetting. When, on the other hand, the stability condition is satisfied;

$$\gamma_s > \gamma_i + \gamma_f\,, \quad (1.2)$$

the film-substrate combination minimizes the total free energy by simply covering the substrate completely with a continuous film, i.e. by complete wetting.

In this thesis, we concentrate on Mo and Ru thin films on a Si(100) substrate with a native oxide. Below, you can find the reported free energies of clean surfaces of Mo, Ru, Si, and SiO_2, for their most prominent surface orientations. Unfortunately, Mo and Ru thin films on a Si or SiO_2 substrate do not satisfy the stability condition for a wetting film. Even when they would be deposited in a configuration, in which they completely cover the substrate, they should break up and dewet, when provided with sufficient mobility to rearrange themselves, similar to a water film on a glass surface.

Primary driving forces for dewetting are the reduction of the combination of the interfacial energies of the thin film-substrate interface, the substrate surface and the surface of the thin film, possibly complemented by the reduction in the energy involved in the mechanical stress between the film and the substrate[30]. This stress can result from the different coefficients of thermal expansion of the substrate and the thin film, which possibly puts the film under strain[24]. Especially for the thin metal films on the Si substrate, the thermal expansion coefficient is, generally, 2 to 3 times higher for the metals. In the case of a native oxide, this difference is reaching almost an order of magnitude. Table 1.2 shows the coefficient of thermal expansions for Ru, Mo, Si and SiO_2.

Material	Surface	Surface free energy (J/m^2)	Reference
Mo	110	2.92	[25]
Mo	100	3.34	[25]
Mo	211	3.11	[25]
Mo	111	3.24	[25]
Ru	100	3.32	[26]
Ru	111	2.90	[26]
Si	111	1.40	[27]
Si	100	2.14	[28]
Si	110	1.52	[28]
SiO_2 (native oxide)	100	0.52	[29]

Table 1.1 *Surface free energies at room temperature of the materials that are the subject of this thesis.*

Material	Coefficient of thermal expansion ($\mu m \cdot m^{-1} \cdot K^{-1}$)	Reference
Ru	6.4	[31]
Mo	4.8	[31]
Si	2.6	[32]
SiO_2	0.56	[32]

Table 1.2 *Coefficient of thermal expansion for the materials that are the subject of this thesis.*

There are various scenarios for the dewetting of a thin film that, ideally, would start out from an initially flat and continuous configuration. It can be shown on theoretical grounds, that a freestanding sheet of material is intrinsically unstable with respect to equilibrium fluctuations in thickness with wavelengths that exceed a certain length scale – this scale is directly related to the surface free energy of the material and the thickness of the film[33–35]. This means that, given a sufficient amount of time, spontaneous, longer-wavelength thickness variations are bound to reduce the film thickness locally to zero. At that point, the finite contact angle θ, dictated by the Young-Laplace equation for a non-wetting film, will stabilize the zero-thickness region and enable the film break open further. In addition to this scenario, most thin films contain specific locations where the energy barrier is reduced for the formation of the first 'holes' through the film. These special places should be regarded as 'defects' and can originate from the geometry, morphology and internal structure of the substrate[36–38], but mostly come from the geometry and atomic-scale structure of the thin film itself[39]. A dominant class of such defects is related to the strong tendency that was mentioned above, for most metals to crystallize. This organizes most metal films into conglomerates of small crystallites, all with different orientations, which introduces grain boundaries where these grains are in contact with each other. These grain boundaries can be regarded as internal surfaces and, like the other interfaces in the system, a free energy cost is associated with each of them. Thin films tend to minimize this cost by introducing height variations at their surfaces, with grooves decorating the grain boundaries and thus minimizing their areas. When provided with sufficient mobility, for example at elevated temperatures, this grain boundary grooving can proceed from the surface all the way down to the substrate[40–42], as is schematically illustrated in Figure 1.1 (a-d). When the interfacial energy between the film and the substrate is sufficiently high, additional grooving can even take place from the film-substrate interface, leading to the formation of voids and again leading to regions where the initially continuous thin film gets interrupted[23,43]. In both cases, it is again the value of the equilibrium contact angle θ that determines whether or not these regions open up further and act as the starting points for the dewetting of the film.

Dewetting of thin films can cause problems in the fabrication of these films or in their applications, for example in the field of integrated circuits, where such dewetting can take place not only for thin metallic films[44–46], but also for thin films of metal silicides[47,48] and silicon-on-insulator (SOI) structures[49,50]. In some cases, dewetting of thin-film structures can be suppressed by using capping layers[51,52], by modifying the substrate on which the thin film is deposited[53], or by using nanoparticles[54]. Unfortunately, no ultimate solution exists by which dewetting is prevented completely.

A special class of applications in which dewetting can be problematic is formed by the thin-film components that are used in state-of-the-art machines for photolithography with

extreme ultraviolet (EUV) light (Figure 1.3). These machines are used for the production of the most refined processor and memory chips to date. In the context of this technology, 'EUV' refers to a wavelength of 13.5 nm. Examples of critical components of these machines that contain thin films are multilayer mirrors and pellicles (Figure 1.4). The mirrors are curved and act as lenses. They are used instead of conventional refractive optics that are of no use at 13.5 nm, because of the extreme absorption they would introduce at this wavelength. The curved mirrors are decorated with a multilayer stack in order to reach an acceptable fraction of reflected light at or close to normal incidence. In these stacks, each interface contributes a small amount to the reflected light amplitude, while a careful choice of the thicknesses of the layers ensures constructive interference of all partial reflections at normal incidence. At 13.5 nm, Si and Mo are used for these multilayer structures in view of their combination of acceptable absorption and relatively high optical contrast at this wavelength. When a precise period of 6.9 nm is chosen for each bilayer, the reflectivity of a single multilayer mirror can, in principle, be as high as 74%[55], but in practice, recorded values reach up to 69.5%[56]. EUV pellicles are ultrathin, freestanding membranes. These protect other elements in the lithography machines, such as the reticles – these are the masks with the 'blueprints' of the semiconductor device that is produced – that can become useless as the consequence of only a single particle landing in the 'wrong' place. The pellicles need to combine a high transmission for the EUV light, in order to minimize the loss of this light, with a high infrared emissivity, in order to limit the heating of the pellicle itself that results from the absorbed fraction of the EUV light.

Often, multilayer mirrors and pellicles for EUV lithography are covered by a Ru capping layer. This layer serves a double purpose. It is meant to protect the delicate, underlying structures from direct exposure to the harsh conditions within the lithography machines, in which the cocktail of EUV photons and gasses, even at low partial pressures, can lead to chemical changes, such as oxidation, and other forms of degradation. And for the pellicles, it also serves to introduce a high infrared emissivity. When exposed to EUV light, the Ru film may warm up to temperatures at which it is prone to dewetting.

The application of EUV mirrors and pellicles forms the motivation for the particular focus of this thesis on structures made of Si, Mo and Ru. We will investigate the thermal stability of these structures down to the atomic scale, in order to understand the dewetting phenomena at play, with a keen eye for potential solutions.

Figure 1.3 *Artist impression of an ASML EUV lithography machine. The optical trajectory of the EUV light is highlighted in purple, with the EUV source position on the far right, the reticle in the upper part and the illuminated semiconductor wafer in the center of the picture (Image source: ASML).*

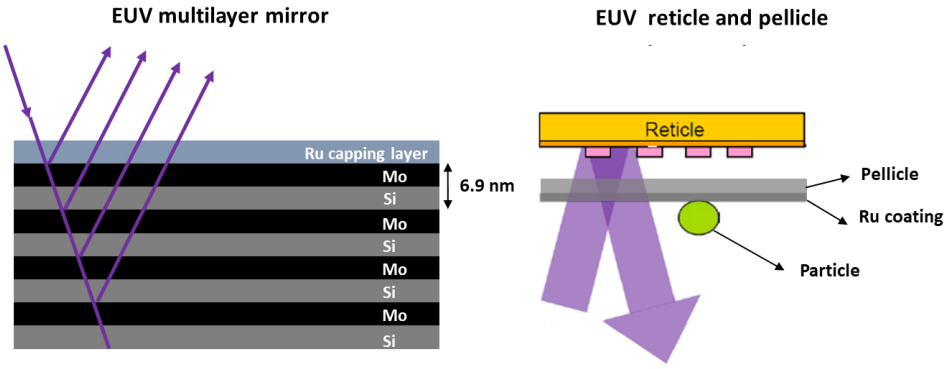

Figure 1.4 *Schematic illustrations of a multilayer EUV mirror and of the use of an EUV pellicle to protect the reticle (mask) from the arrival of particles that would otherwise be imaged sharply on the semiconductor wafer in the lithography process. Both multilayer mirrors and pellicles are typically covered by a capping layer, usually in the form of a Ru film with a thickness in the order of a few nanometers.*

The elements Mo and Ru exhibit similar properties. They both are transition metals, located in period 5 of the Periodic Table and their electron configuration ends with $5s^1$. Their standard atomic weights, melting points, densities and other chemical properties are quite similar. Apart from these similarities, there are also some essential differences between these two elements. For example, their crystal structures are different, namely body-centered cubic (bcc) for Mo and hexagonal close-packed (hcp) for Ru. From a chemical perspective, Mo has a much stronger tendency to oxidize than Ru, which makes it unfavorable in oxidizing environments, such as those in EUV lithography machines. But Mo absorbs light at 13.5 nm less strongly than Ru, which is, of course, highly desirable for application in EUV lithography technology.

The second chapter of this thesis will address the growth and stability of elemental films of Mo and Ru and of Ru-Mo bilayers on Si substrates with a native oxide. The thermal stability, especially with respect to the grooving of grain boundaries and the de-wetting of the ultrathin films, is investigated by bringing the films to

elevated temperatures and inspecting the result by various forms of microscopy and spectroscopy.

Chapter 3 will review the literature about more radical, possible solutions to the grooving behavior, introduced by the grain boundaries of thin, polycrystalline metal films. Most importantly, we will discuss possibilities to produce films of Mo and Ru with no grains at all, in the form of a metallic glass. For this, it is essential to familiarize ourselves with the thermodynamics and the evolutionary dynamics of amorphous and polycrystalline metal alloys. In addition to this, we will briefly review the fabrication methods, properties and limitations of such metallic glasses.

As we will see in Chapter 3, usually, elemental metals cannot easily be made and kept amorphous, in practice. This is why Chapter 4 will focus on binary metal alloys, in particular, consisting of Ru and Mo. We will provide evidence that it is possible to obtain a truly amorphous alloy of these two metals.

Chapter 3 explains that an amorphous configuration does not establish a genuine thermodynamic phase and that it is inherently unstable or, at best, metastable with respect to crystallization. This natural tendency for crystallization may be accelerated by heating or other forms of aging of thin amorphous films, potentially with detrimental effects on many properties of such films. In chapter 5, we will investigate the effect of heating on the atomic-scale structure, chemical composition and surface morphology of thin, metallic glass films.

1.2 Experimental methods

Sample preparation

A Polyteknik Flextura M506 S[57] system was used in the NanoLab facility of our neighbor institute AMOLF, for the sputter deposition[58] of all thin films in this work. In contrast to Ru-Mo growth studies reported in the literature[59,60], our substrates were kept at room temperature. All films were deposited on p-doped Si(100) substrates; the native oxide on these substrates was not removed prior to deposition. For the production of thin Mo_xRu_{100-x} alloy films, Mo and Ru were co-deposited from separate sources by RF and DC sputtering, respectively. We used different types of power supplies for the two metals for practical reasons, but we do not expect this to influence the results significantly. The base pressure of the sputter deposition system was 1×10^{-7} mbar and the argon (Ar) pressure was 2×10^{-3} mbar or higher during the deposition. In addition to the alloy films, also regular films of pure molybdenum and pure ruthenium were deposited by DC sputtering. During deposition, the substrates were rotated, in order to optimize the homogeneity of the deposition.

Table 1.3 provides typical examples of the sputter-deposition conditions employed for the production of the alloy films discussed in this thesis. The first column shows the resulting compositions that were derived from the energy-dispersive x-ray spectroscopy (EDX) measurements in our scanning electron microscope (SEM, see the next page).

Alloy composition (EDX)	Power level (W) and type of power supply for Ru	Power level (W) and type of power supply for Mo	Ar pressure (mbar)	Deposition rate (nm/s)
Pure Ru	200 DC	–	2×10^{-3}	0.30
$Ru_{77}Mo_{23}$	75 DC	100 RF	2×10^{-3}	0.16
$Ru_{43}Mo_{57}$	75 DC	250 RF	2×10^{-3}	0.28
Pure Mo	–	75 DC	1.33×10^{-2}	0.15

Table 1.3. *Pure and alloy film compositions, measured by SEM-EDX, in combination with the employed deposition powers, the working gas pressures used, and the types of power supplies (DC versus RF) used in the sputter deposition process. The deposition rates in the final column were derived from the measured film thicknesses.*

Characterization

Measurements of the thicknesses of the deposited metal films were carried out in the following way. Prior to metal deposition, which was usually done simultaneously on multiple substrates, one of these substrates was partly coated by a photoresist film. After the metal deposition, the resist was washed off by acetone and isopropanol and this cleaning procedure also removed the deposited metal film from those parts of the substrate that had first been coated by the resist, while the metal film on other parts of the substrate stayed in place and remained unaffected. This procedure enabled us to accurately measure the height difference between the bare regions where the resist was removed and the regions that had not been coated by the resist and that were covered by the thin metal film. These height difference measurements were done by use of a profilometer and by atomic force microscopy (AFM). This provided us with accurate measurements of the film thicknesses. Samples used to measure the film thickness were not utilized for further experiments to avoid possible contamination from the employed chemicals and their residues. The films used in this thesis had thicknesses typically ranging from 4 to 30 nm.

We used AMOLF's FEI Verios 460 SEM system[61], with a Schottky field electron gun, for the inspection of substrates and thin films with scanning electron microscopy. The SEM images were taken at an electron energy of 5 keV and a beam current of 100 pA, unless indicated differently, and the samples were placed at approximately 4 mm distance from the analyzer. For all SEM images, we used the immersion field mode, in order to optimize the spatial resolution[62].

As an additional imaging technique, in particular for detailed measurements of the surface topography[63], the film thickness (see above) and the surface roughness, we performed tapping mode AFM, using a Bruker Dimension Icon AFM[64] system in ScanAsyst-air mode with silicon tips on silicon nitride cantilevers of Bruker's SCANASYST-AIR or SCANASYST-AIR HR type. AFM image processing was done by use of the NanoScope Analysis version 2.00 software, Gwyddion, and a custom Python script.

We used two techniques to measure the composition of the deposited alloy films. The first of these was energy-dispersive x-ray spectroscopy (EDX)[65], for which we used an Oxford Xmax 80 detector, placed inside AMOLF's scanning electron microscope. Typically, the EDX measurements were performed at multiple locations on the sample.

The second technique that we employed to measure the surface composition of the thin films was X-ray photoelectron spectroscopy (XPS)[66]. Measurements with this technique were performed *ex-situ* with X-rays emitted from a monochromatic Al-K_α (1486.6 eV) source operating in an ultrahigh vacuum setup (base pressure better than 1.0×10^{-9} mbar) equipped with a Scienta Omicron R4000 HiPP-3 analyzer (swift acceleration mode, 1 mm

slit entrance) for elemental and chemical characterization of the surfaces of the films. Measured XPS peak shapes and intensities were fitted using the software KolXPD from Kolibrik[67]. Whereas the composition measured by XPS is characteristic of the outermost atomic layers of the investigated surfaces and thin films, the SEM-EDX results should be regarded as averaging over the entire thickness of the films that we investigated.

Additional structural information came from standard, grazing-incidence X-ray diffraction (GI-XRD) measurements that were performed with Cu-kα radiation (wavelength of 0.15406 nm), using a Panalytical X'Pert MPD diffractometer. The incidence angle was set at a constant, low value of 0.5° with respect to the sample's surface plane, for all measurements.

Transmission electron microscopy (TEM)[68] measurements were performed at the Zernike Institute for Advanced Materials of Groningen University. For this purpose, cross-sectional specimens were prepared in Groningen, with an FEI Helios G4 CX dual beam system at 30 kV ion energy and polished at 5 keV and 2 keV to remove residual surface damage. These specimens were analyzed with a double-aberration-corrected FEI Themis Z scanning transmission electron microscopy (STEM) system at 300 kV. High-angle annular dark-field (HAADF) STEM images were recorded with a probe current of approximately 200 pA, at a convergence semi-angle of 21mrad and with HAADF collection angles of 61–200 mrad. EDX spectral imaging was performed with a probe current of 1 nA, where the spectra were recorded with a Dual-X system, providing in total 1.76 sr EDX detector.

Chapter 2

THERMAL STABILITY OF MOLYBDENUM AND RUTHENIUM THIN FILMS

This chapter presents a study of the growth and evolution of ultrathin films of elemental Mo and Ru on Si substrates with a native oxide. Thermal stability, especially the grooving of grain boundaries and the de-wetting of the ultrathin films, is investigated by bringing the film structures to elevated temperatures and focusing primarily on the morphologies and microstructures of the thin films. Initially, the thin films exhibit a grainy surface as a result of their polycrystalline structure. For both metals, the grains of the films start to coarsen already at temperatures as low as 300°C, while they show complete dewetting at 700°C and 800°C for Ru and Mo respectively. In an attempt to influence this dewetting behavior, we further investigate the high-temperature behavior of bilayers, consisting of a thin Ru film on top of a thin Mo layer, on Si substrates with a native oxide. We observe that the bilayer system exhibits significantly better thermal stability compared to its counter-parts with pure Mo and pure Ru.

2.1 Introduction

Surfaces and interfaces make thin films energetically less favorable than a three-dimensional bulk arrangement of the same material. This can lead to the instabilities of thin films, such as dewetting. Dewetting is the phenomenon that a thin film breaks up into separate, three-dimensional clusters and leaves the underlying substrate exposed. The energetic driving force for dewetting resides in the differences in surface and interface-free energies of the thin film and the substrate, possibly in combination with driving forces deriving from mechanical stress between the film and the substrate. This phenomenon can be a major concern, especially for applications in which the film serves to protect the underlying structure and applications in which the precise layer geometry is essential and needs to be preserved. From the perspective of the interfacial free energies that are involved in the configuration of a film on a substrate, two possible scenarios should be considered, dictated by the difference in Gibbs free energy, ΔG, specified in Equation 1.2. (1) If the substrate surface free energy is higher than the sum of the surface free energy of the thin film and the free energy of the interface between the substrate and the film, the stability condition ('complete wetting') is fulfilled and the film will tend to cover the substrate, even under conditions that allow it to rearrange Itself. (2) For thin films for which the sum of the surface free energy of the thin film and the free energy of the interface between the substrate and the film is higher than the surface free energy of the substrate, the situation is reversed and the driving force is towards configurations in which the thin film adopts the shape of an ensemble of 'droplets' and it no longer covers the substrate. These considerations play a dominant role in the behavior of thin Ru and Mo films that is under investigation in this chapter.

Thin metal films have a strong tendency to crystallize, which leads to an internal structure of differently oriented, single-crystalline grains. The grain boundaries between these crystallites are special regions in this structure, where the perfect crystallinity is interrupted. These regions are associated with interfacial free energy, the grain boundary energy, that makes the thin polycrystalline film seek for ways to reduce its total (internal) area. There are three ways to do so, namely reorientation of grains and grain boundaries into lower-energy grain-boundary configurations, coarsening of the grain structure and the corresponding reduction in the grain boundary density and the reduction of the grain boundary heights by the introduction of a groove at the location of each grain boundary that ends at the surface of the film. Due to the latter effect, each of the outer grains of the film is no longer flat at its surface, but develops into a portion of the equilibrium crystal shape. When the temperature is high enough for the surface atoms of the polycrystalline film to exhibit sufficient mobility, these energetic preferences will drive the grain boundary grooving and the surface of the film will become rough. The grain coarsening effect makes

all dimensions of the grains increase, adding to the roughness and depth of the grooves. When the grooves become deep enough to reach the interface with the substrate, the two scenarios that were discussed above become relevant. In the case of complete wetting, the grooving process should come to an abrupt standstill when the interface is reached. In that case, the film exhibits significant thickness variations, but it keeps covering the substrate completely, while the grain coarsening should stop. By contrast, in the non-wetting case, the free energy is lowered further when the groove opens up at the interface and the substrate is progressively exposed. This pathway towards dewetting should be regarded as an extra vulnerability of all polycrystalline, non-wetting films.

From a chemical point of view, Ru has a strong resilience against oxidation. This property makes that Ru is used as the material for capping layers to protect other materials in various applications. Ru also has reasonable transparency for EUV light, which makes this material extra interesting for capping applications in the context of EUV lithography. However, at elevated temperatures, thin Ru films are prone to dewetting, also on Si and SiO_2 substrates, on which Ru films are often applied. The surface energies in Table 1.1 indicate that the surface free energies of Ru surfaces are higher than those of Si and SiO_2 substrates. As a consequence, films of Ru on Si or SiO_2 substrates will, eventually, suffer from the phenomenon of dewetting, introduced above. In the PhD thesis of C. Sfiligoj[69], the thermal stability and wetting properties were investigated of elemental Ru thin films with various densities that were deposited on Si(100) substrates, covered with a native oxide. As was shown in that work, all Ru thin films dewet this substrate when annealed at temperatures between 700 and 800°C, which disqualifies Ru as a protecting layer on oxidized Si substrates in high-temperature applications. Figure 2.1 shows 5 nm thick Ru films on a Si(100) substrate, before and after annealing at 600°C. The annealing is clearly seen to lead to grain growth and coarsening with deeply grooved grain boundaries. In some regions, the depth of the grooves is so large that they reach the interface with the substrate, which results in the formation of holes; this is the first stage of dewetting.

In this chapter, we investigate whether Mo thin films can be employed as a potential anchoring or adhesion interlayer between the oxidation-resistant Ru capping layer and the oxidized Si substrate, in an attempt to improve the thermal stability of configurations with a Ru top layer.

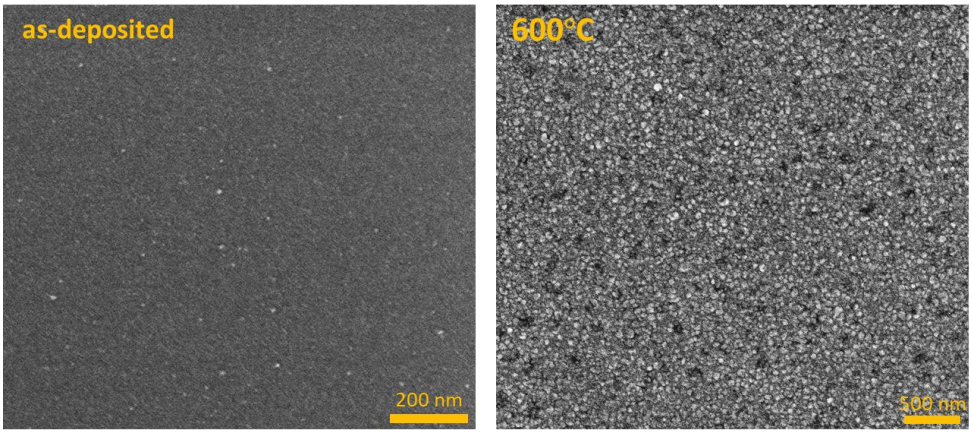

Figure 2.1 *SEM micrographs of 5 nm thick Ru films on a Si(100) substrate with a native oxide, directly after deposition (left) and after annealing for 1 hour at 600°C (right). Note that the scales of the two images are different.*

Based on the numbers in Table 1.1, one might expect Mo thin films on Si or SiO_2 substrates to exhibit similarly strong dewetting behavior as Ru, since the surface energies of Mo are similarly high as those of Ru. In spite of this similarity between the two refractory metals, Mo thin films may still introduce two advantages with respect to Ru that could lead to significantly reduced dewetting. The first of these has to do with the formation energy of the metal-Si (or SiO_2) interface, which we may expect to be more favorable, i.e. lower, for Mo, due to its stronger tendency to form a silicide, which readily takes place when Mo atoms are deposited on a Si surface, even at room temperature[70]. The second is that, as was discussed in Chapter 1, dewetting requires surface mobility, for the thin film to re-shape itself under the influence of the thermodynamic driving forces. Since diffusion co-efficients depend more or less on the ratio between the temperature and the melting point of a material, the surface mobilities of Mo atoms on a Mo surface or at an interface between Mo and another material should be expected to be significantly lower than those for Ru at the same temperature, given the fact that the materials have similar properties but the melting point of Mo is almost 300°C higher than that of Ru. In other words, we should expect dewetting at the same temperature to proceed orders of magnitude more slowly for Mo than for Ru, or for it to happen at the same pace only at a significantly higher temperature.

Prior to introducing Mo as an adhesion layer, we first investigate the thermal stability of Mo thin films on oxidized Si substrates, in order to verify the above expectations with

respect to possible compound formation and raised dewetting temperature. After introducing the Mo layers, we continue to follow the thermal behavior of bilayers of Mo and Ru, in which the Mo serves as the adhesion layer for the Ru capping layer.

The Mo thin films in this thesis were obtained by DC sputter deposition on Si substrates. For this combination, other studies report the formation of a 1.2 to 1.9 nm thick, amorphous interlayer of molybdenum silicide[71–73]. Even though the thickness of this silicide is known, the atomic-scale details of the formation process remain to be understood. What we know, is that after, or maybe also due to the arrival of the Mo atoms on the surface, the Si atoms appear to have sufficient mobility to engage with the Mo atoms and form a compound[74,75]. This process is governed by the free energies of the surface and interface of all materials involved, i.e. of the Si substrate, the silicide film and the pure metal, by the formation enthalpy of the silicide and by the activation energies of the diffusion and reaction steps that are required for the formation of the compound. It is possible to avoid the interfacial silicide formation, simply by leaving the Si substrate covered by its native oxide, prior to Mo deposition. This thin oxide layer can act as a diffusion barrier and prevent the direct interaction between the Mo and Si atoms up to a certain temperature. However, further heating may still enable the system to overcome the activation energies for diffusion and silicide formation, resulting in the growth of an interfacial $MoSi_2$ layer at a temperature of 520°C[76]. For this process, different activation energies were reported of 4.1 eV[76] and 2.4 eV[77].

In this chapter, we address the evolution of films of elemental Mo, and bilayers consisting of Ru on top of Mo, on Si substrates with a native oxide. We use SEM and AFM to follow the thermal stability, in particular the grain coarsening, the grooving of grain boundaries and the dewetting of the thin films. Our study reveals a surprising stability of the Ru-Mo bilayers against dewetting, beyond the stability of Mo films and Ru films. In addition, we report unusual silicide structures that form at high temperatures for Mo and Mo-Ru films on oxidized Si substrates.

2.2 Thermal stability ultra-thin molybdenum thin films

In this section, we investigate the thermal evolution of Mo thin films with a thickness of 5 nm, deposited by DC sputter deposition on a Si(100) substrate with a native oxide. Details regarding the sample preparation can be found in the experimental methods section of Chapter 1.

Before metal deposition, we characterized our Si(100) substrates with ellipsometry and AFM. From the ellipsometry data, we obtained the thickness of the native oxide to be 1.5 nm. As we will see, this oxide acts as a diffusion barrier. But it also introduces modest roughness, which we measure by AFM to be 0.27±0.06 nm. All roughness values reported in this thesis are defined as the root-mean-square (RMS) height variation with respect to the average surface plane.

The surface morphology and internal structure of freshly deposited and subsequently annealed Mo thin films on Si(100) with a native oxide were investigated by SEM and AFM. Figure 2.1 presents SEM micrographs of the thermal evolution of a 5 nm thick Mo film. The first image was taken directly after

deposition at room temperature, i.e. prior to annealing, and shows a relatively smooth thin Mo film that appears to cover the substrate completely. Elemental characterization by XPS did not show any signal from Si, which confirms that the film is fully closed. Within the modest contrast of the SEM micrograph, we recognize granular structures, which should be regarded as the typical signature of the nanoscale polycrystallinity of the metal film.

The corresponding, first AFM image in Fig 2.2 for the freshly deposited Mo film is consistent with the polycrystalline film structure. From the image, we obtain an average lateral grain diameter of 7.4 nm. This grain size somewhat exceeds the thickness of the film, indicating that the entire film has the thickness of single grains, a typical result for ultrathin, polycrystalline films[78]. From the image, we measure a surface roughness of 0.35±0.03 nm. This height variation is larger than that of the underlying substrate, but it is still relatively modest, for example when compared to the roughness encountered when Mo is deposited on Si(111) without an oxide[75]. We interpret this in the context of the oxide's role as a diffusion barrier that prevents silicide formation, which would otherwise lead to the buildup of extra roughness. The observed roughness is therefore a genuine surface topography that is directly correlated with the grooves in the grain structure of the polycrystalline film and it has a relatively modest value as a direct consequence of the limited, average grain size. We will come back to this point later in this chapter.

After inspecting the as-deposited film, we annealed the sample in a vacuum oven with a base pressure of 5×10^{-7} mbar to various, increasing temperatures, each time for a duration

of 60 minutes. Figure 2.1 presents SEM images after the annealing to four subsequent temperatures, showing changes in contrast and in characteristic shapes that set in already at a low temperature. Between the freshly deposited film and the situation after annealing at 200°C, the contrast reduced, suggesting that the annealing made the film smoother. However, at higher temperatures, between 200°C and 550°C, the SEM micrographs indicate larger and rougher grains, suggesting that at these temperatures grain coarsening and grain boundary grooving take place. This is a well-known behavior that was reported and explained by Rost et al.[22]. To obtain quantitative information on the changes in surface roughness, we also conducted AFM measurements on the annealed samples; see Figure 2.2.

Up to 200°C, we indeed observe a decrease in surface roughness. Upon annealing of the sample to a higher temperature of 300°C, the roughness is found to increase again. In figure 2.2.d we plot the variation in surface roughness as a function of temperature. The sequence of an initial decrease of roughness, followed by an increase at higher temperatures is reminiscent of the observations by Rost *et al.* for the evolution of a thermally evaporated film of Au on a quartz substrate[22]. Even though the deposition methods and the metals differ, we believe that the physics that underlies the observed evolution is the same in both cases. At higher temperatures, the roughness decreases again. This is not observed for the Au films and has a different origin that we will discuss later.

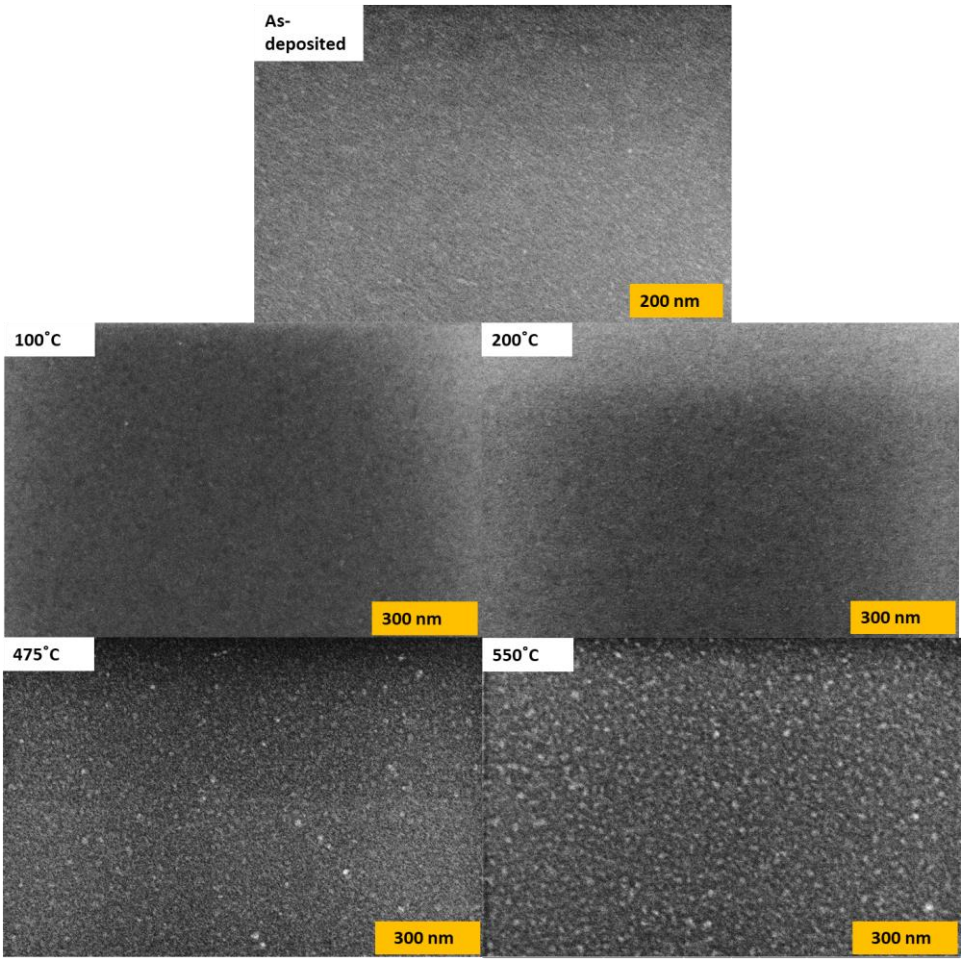

Figure 2.1 *SEM micrographs of the 5nm Mo film DC-sputter-deposited at room temperature on a Si(100) substrate with a native oxide. The first image is for the freshly deposited film. The other four images were taken after subsequent annealing for 60 min, each time at a higher temperature, as indicated in the images. The yellow bars indicate the length scales of the images; note that the first image is zoomed in further than the others.*

The physics of the evolution of a polycrystalline metal film already starts during the formation of the initial film structure. During the deposition of the film, the arriving atoms have no more than limited and largely transient mobility. This enables them to find each other and nucleate small adatom clusters that serve as the starting points for the grains that make up the film. Upon further deposition, these grains merge to fill out and close the layer. The limited mobility makes it practically impossible for these initial grains to optimize their orientations with respect to the substrate and their neighbors. The unfavorable, high-free-energy grain boundaries between these grains, lead to relatively deep grain boundary grooves and correspondingly large height variations in comparison with the small grain sizes. If the atoms arrive with higher kinetic energy, so that they have more transient mobility or they impart more energy and mobility into the grain structure that is already present, the film can develop larger grains with lower-energy grain boundaries during the deposition. This is why the surface morphology of the as-deposited thin films is strongly dependent on the detailed settings of the sputter deposition parameters[79].

After deposition, the film can be made to evolve by subsequent annealing. This supplies the adatoms with surface mobility and can also enable the motion of grain boundaries. The latter type of mobility makes it possible for the film to undergo grain re-orientation, thus lowering the average free energies of the boundaries between the grains, of their surfaces, and of their interfaces to the substrate, and it leads to grain coarsening, thereby reducing the total amount of grain boundary area per unit of surface area. The removal of high-energy grain boundaries reduces the average depth of the corresponding grain boundary grooves, which explains our observation of the initial drop in surface roughness up to 200°C, in full analogy with the observations for polycrystalline gold films[22]. The subsequent grain growth at even higher temperatures leads to a scaling up of the height differences, in proportion to the coarsening of the average grain size, thus making the roughness increase again, also following the observations in ref. 78 for gold films. Below, we will report this behavior also for the thin bilayer film.

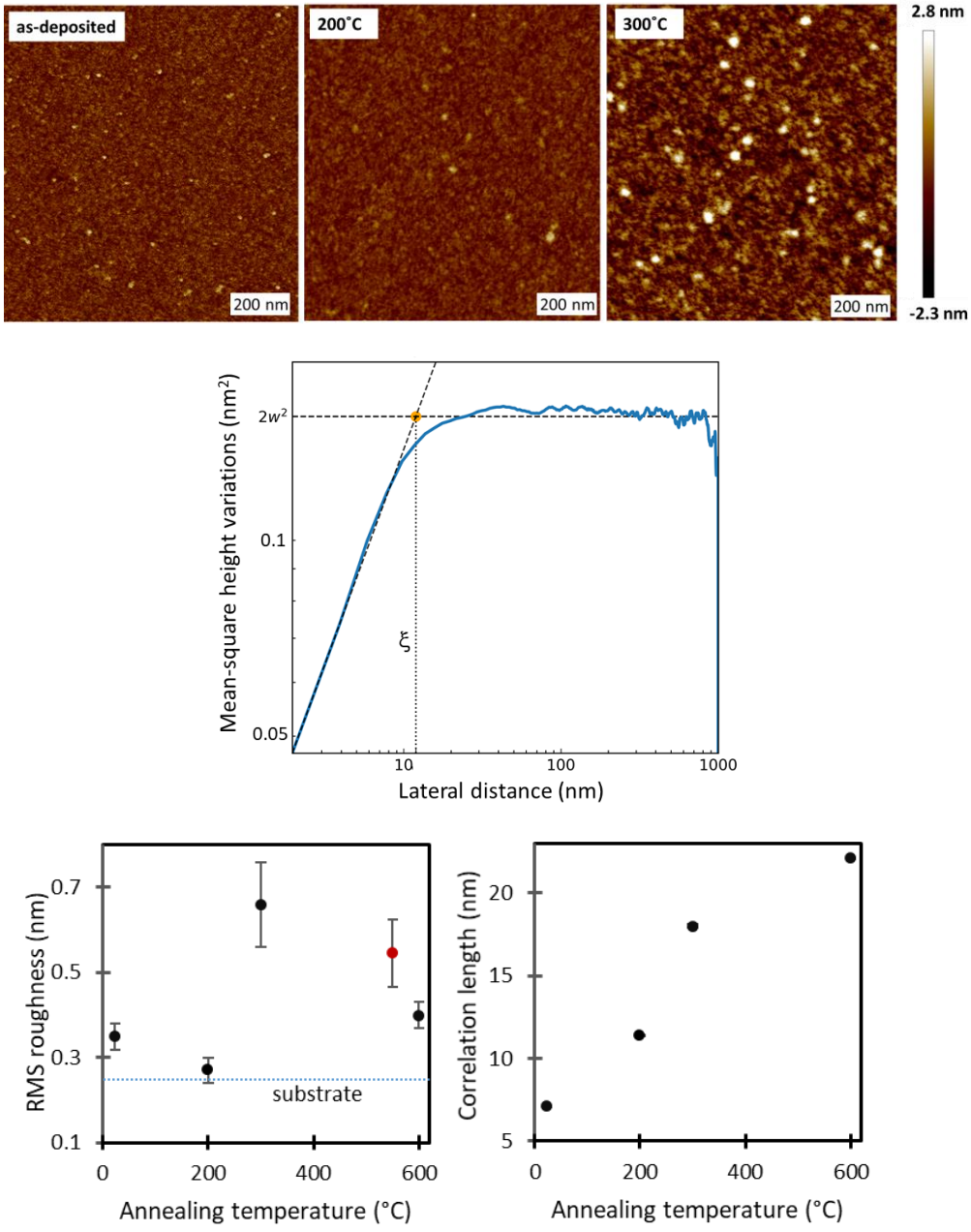

Figure 2.2 *AFM images obtained on the 5 nm thick film of elemental Mo, DC-sputter-deposited on a Si(100) substrate with a native oxide. In addition to the freshly deposited film, the morphology is shown after annealing at two temperatures, each time for 60 minutes. All images*

have dimensions of 1 µm × 1 µm and they are all displayed with the same conversion of height variations into colors, as indicated by the color bar. The middle panel presents the height correlation function, measured from the AFM image of the Mo layer after annealing at 200°C. The dashed lines represent the corresponding fits for the asymptotic and power-law regions where w is the surface roughness (RMS) of 0.27 nm and x is the correlation length of 11.9 nm. The measured root-mean-square height variations and correlation lengths are plotted versus the annealing temperature in the bottom panels. Please note that the red data point for the RMS roughness at 550°C is taken from a larger image of 10 µm x 10 µm. Due to stronger data-averaging effects in AFM images with larger distances between pixels, RMS roughness values from larger scan size images tend to show somewhat lower values for the roughness.

At temperatures of 600°C and above, we observed strong deviations in the film evolution from mere grain coarsening. Figures 2.3.a-b are SEM micrographs that show the formation of nearly perfectly circular shapes on the surface with a distinct SEM contrast (lower yield). Where two isolated 'dark' structures meet, they are seen to merge in a way that suggests that the combined shape is the result of a line tension and a finite mobility. The radii of the (isolated) circles in these SEM observations vary between 0.5 and 0.8 µm. We have not observed any long-range order or pattern in the distribution of the circular structures over the surface. Figure 2.3.b demonstrates a smaller scan size with a higher resolution that provides an observation of modest differences between the granular structures inside the darker circular regions and in the surrounding, brighter areas.

The high contrast in the SEM micrographs indicates a significant difference in the yield of secondary electrons emitted by the regions inside and outside the circles. This difference in secondary electron yield must be originating from a difference in either the material composition, its density, or the surface topography. Unfortunately, elemental characterization by EDX mapping is inconclusive for such an ultra-thin film because of the long mean free paths of the impinging (SEM) electrons and the emitted X-rays. Topographical differences should be visible in the AFM images. Figure 2.3 c shows the topographical AFM image. Panel-e shows the height profile along the 300 nm long blue line in Panel-c. Whereas much of the 'contrast' in the height image derives from subtle differences in the pattern of height variations inside and outside the circles, there is a modest difference in height, the inside of the circles being roughly less than 0.1 nm lower than the regions outside the circles. It is not very probable that these topographical subtleties would be responsible for the distinct, high contrasts in the SEM images, which leaves differences in material properties, in particular the composition or the density, as the most probable origin of the contrast in secondary electron yields. This is supported by the AFM phase image in Figure 2.3.d. Phase shifts in tapping-mode or non-contact AFM measurements reflect to what extent the tip-surface interaction deviates from being

purely elastic and are therefore a measure for the energy dissipation that the tip motion encounters. Systematic differences in this phase shift between different regions of the surface indicate mechanical differences between these regions, the surface systematically absorbing more energy in some regions than in others. The phase contrast in Figure 2.3.d should be interpreted as a clear indication of differences in material that the tip interacts with inside and outside the circles.

The most straightforward way to explain the combination of evidence from the SEM and AFM data is that the annealing at 600°C has enabled the Si and Mo to come into contact with each other and form a compound: molybdenum silicide. This would require diffusion of one of these species through the native oxide, or the decomposition of the oxide in favor of silicide formation. The circular shape strongly suggests that the material conversion proceeds in the form of a radially expanding reaction front, starting independently at the center of each of the circles. The low density of circles immediately shows that the process can only begin at special locations on the surface. This is typical for processes that are starting at defect sites, which, in this case, could be defects in the oxide layer that could establish easy diffusion channels for the Si atoms at and above 600°C. Such defects can be present in the native oxide already at room temperature. But they might also form upon annealing as a consequence of the large differences between the coefficients of thermal expansion for Mo, Si and SiO_2, of 4.8, 2.6, and 0.56 $\cdot 10^{-6}$ K^{-1}, respectively. These numbers indicate that the oxide layer will be under significant tensile stress, as it would tend not to follow the expansion of the substrate and the Mo film. Such stress can cause localized deformations in the oxide layer, such as local thinning, which relieves part of the tensile stress[80] and might result in the formation of voids in the oxide layer that act as the diffusion channels and allow the Si to migrate to encounter the Mo atoms.

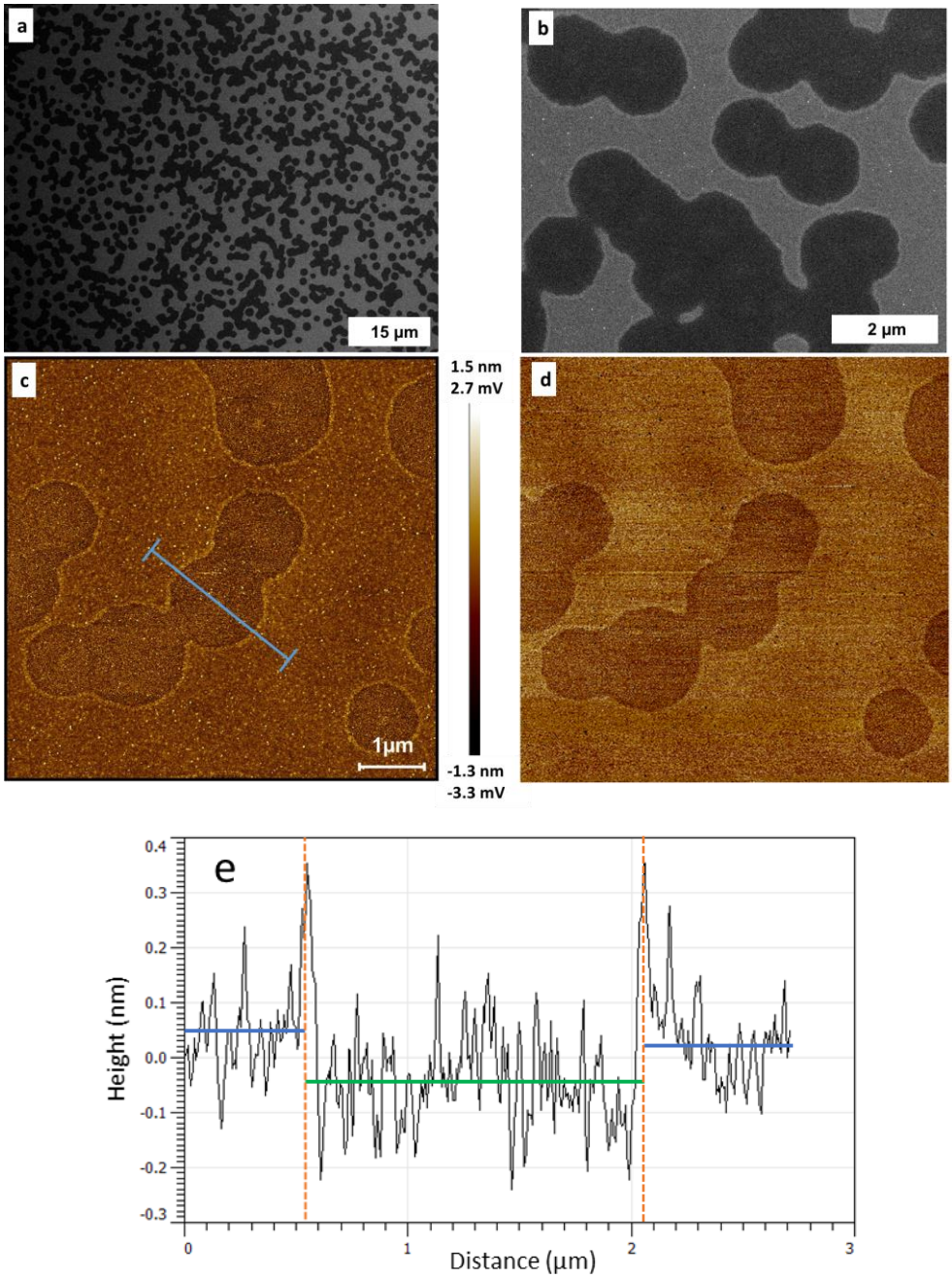

Figure 2.3 *SEM (a,b) and AFM (c,d) images obtained on a 5 nm thick Mo layer DC-sputter-deposited on a Si(100) substrate with a native oxide, after annealing for 60 minutes at 600°C. The two AFM images display the height (c) and phase signals (d). They are displayed with the*

conversion of height (height sensor) and voltage variations (phase image) into colors, respectively, indicated by the color bar. Panel (e) shows the height profile along the blue line in the height image (c), where the two vertical lines indicate the locations of the perimeter of the dark region that is traversed by the profile and the green line and blue lines indicate the average height within the dark region and the average height around it respectively.

A few extra words are in place on the evolution of surface roughness. It was found to start at a value of 0.35 nm for the as-deposited 5 nm Mo film and, after an initial decrease, the roughness rapidly increases at temperatures above 200°C (see Figure 2.2). Whereas we expected the rising trend of surface roughness at elevated temperatures to continue, the AFM micrographs after annealing at 600°C display surface roughness values of 0.41 and 0.37 nm for the circles and the surrounding surface, respectively. Averaged over the entire surface, the roughness amounts to 0.40 nm, which is almost equal to that of the as-deposited film, within the error margin. This reduction of roughness goes against the typical evolution of thin, polycrystalline metallic films that exhibit progressive surface roughening at elevated temperatures due to grain boundary grooving. The smoothening is indicative of a significant change in the atomic arrangement. The obvious scenario for this change in structure is that the silicide that is forming at these high temperatures (see above) is amorphous and therefore contains no grain boundaries. This would immediately remove the energetic driving force for roughening and actually favor a smooth surface. Indeed, it is well known that Mo silicide formation can result in an amorphous structure up to certain film thicknesses[74,81]. The surface smoothing of polycrystalline Mo thin films was also observed in another study by subsequent annealing to increasing temperatures, as a result of the reduction in the grain size[82] but in contrast, the correlation length is found to be gradually growing at elevated temperatures in our case (Figure 2.2).

Despite the observation of the unusual silicide formation, we have not found any sign of dewetting up to a temperature of 600°C. Both AFM and SEM images are still manifest of a closed film, covering the entire substrate without any holes or separated 3D islands.

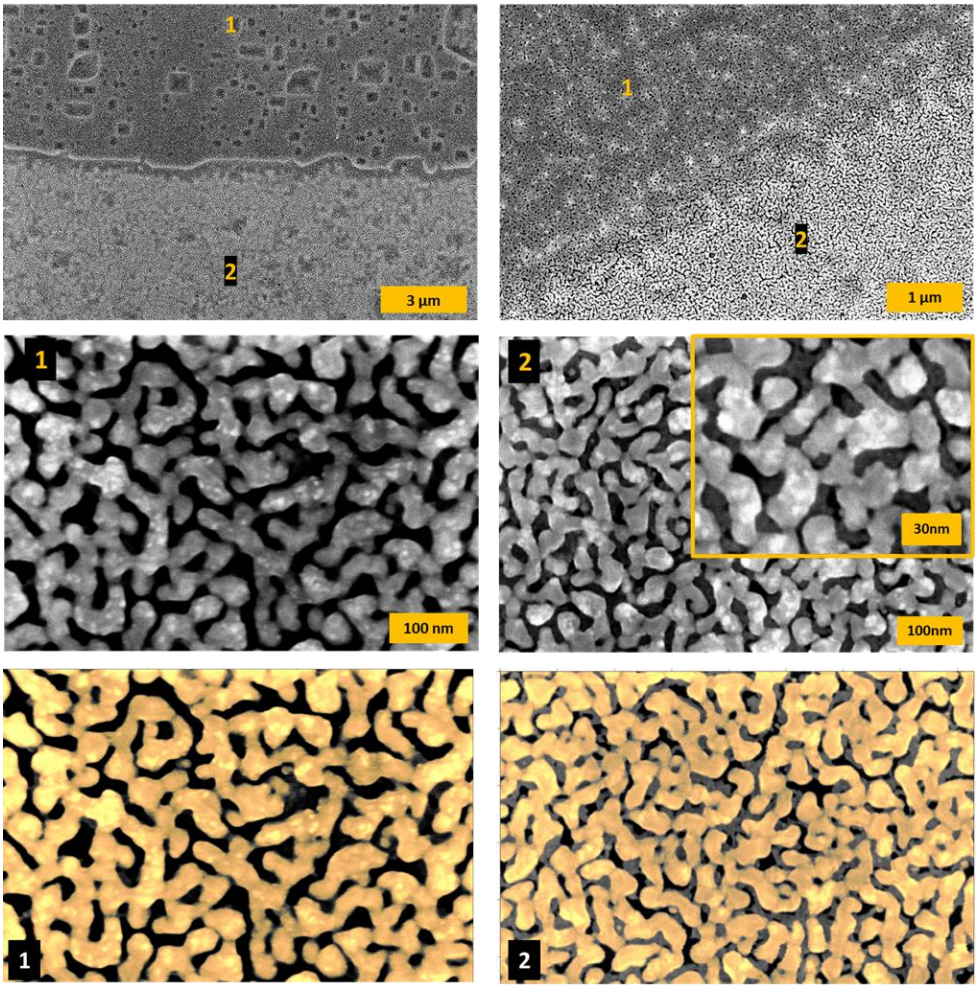

Figure 2.4 *SEM micrographs obtained for the pure Mo thin film after annealing at 800°C. The upper panels are large-scale views that reveal the simultaneous presence of two different types of regions, labeled 1 and 2, with a distinct contrast between them. The two middle panels contain higher-resolution detail on these different regions. The two bottom panels are colored versions of the middle panels, meant to bring out correspond to darker, single-layer dewetting and lighter areas, double-layer dewetting, respectively.*

The next stage in our experiment was to anneal a freshly prepared sample at 800°C. Figure 2.4 presents the corresponding SEM micrographs. The upper left panel contains a large-size scan that covers two distinct regions, labeled 1 and 2. Here, we first discuss these two different types of regions. A somewhat higher-magnification view on a different part of the surface in the upper right panel brings out the network of worm-like structures and holes in both regions, which we associate with dewetting. In general, dewetting of a film goes through three subsequent stages. The first is the formation of holes. In this phase, fluctuations in the film thickness, for example those that are introduced by grain boundaries, lead to places where the film thickness is reduced to zero, at which locations the film starts to rupture. The second stage is the labyrinth stage. This stage consists of the growth of the sizes of these holes and their coalescence, the latter making the film take the shape of a labyrinth of worm-like structures83,84. This seems to be precisely what we observe in Figure 2.4. The labyrinth stage is followed by island formation, which forms the final stage of dewetting. In this stage, the coating breaks up into droplet-like, separated islands. Since no droplet-like structure is observed in Figure 2.4, we conclude that the dewetting of the Mo film has not reached the final stage yet at 800°C.

In order to understand the noticeable contrast between regions 1 and 2, we present higher-magnification SEM micrographs for both regions in the middle panels of Figure 2.4. The left panel, region 1, is typical for dewetting of a film on a substrate. In the middle right panel, region 2, an additional brightness level is visible. This is easier to distinguish in the bottom versions of the two middle images, in which we colored the top level in yellow and recognize the intermediate level as grey. It is the dominant presence of this intermediate level and the somewhat higher brightness of the brighter level that make the average brightness of region 2 higher than that of region 1, which is what can be seen in the two upper panels of Figure 2.4. I refer to the situation with two different contrast levels in the SEM images as “double-layer dewetting”. We speculate that the situation at 800°C has some resemblance to that at 600°C. The two types of regions at 800°C may correspond to the inside parts and the outside parts of large circles, where each circle is a reaction-diffusion front, similar to the ones observed at 600°C. At the higher temperature, the entire surface must already be converted from pure Mo into a silicide layer. But it may well be that, at least on part of the surface (region 2), we see the simultaneous presence of two silicides, each with a distinct composition. Differences in their dewetting behavior at 800°C might then explain the double-layer dewetting appearance in the SEM images.

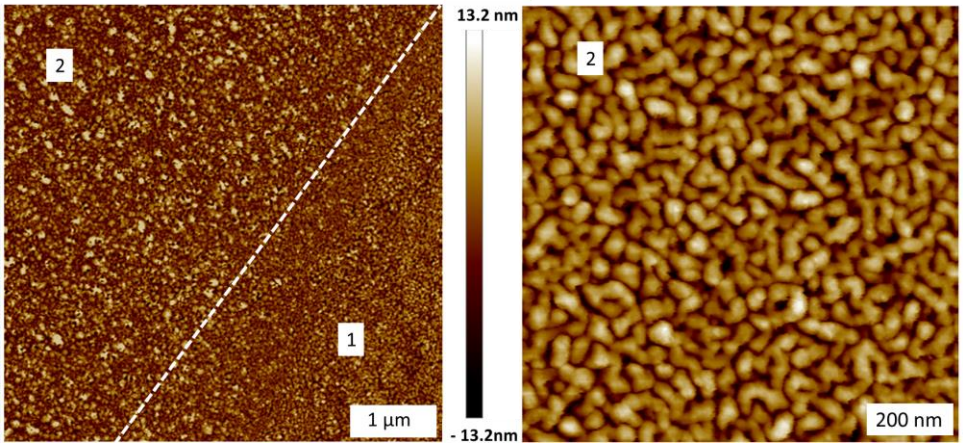

Figure 2.5 *AFM images, obtained on 5 nm thick layers of elemental Mo after annealing at 800°C. The right panel displays a higher-resolution scan on region 2. Both images are displayed with the same conversion of height variations into colors, as indicated by the color bar in the middle.*

The AFM image in the left panel in Figure 2.5 displays the morphologies of two distinct regions that we separated for clarity by the diagonal dashed line. The image looks similar to the SEM images in Figure 2.4 and the difference between regions 1 and 2 is mostly due to the heights of the protrusions, which may reflect a characteristic difference between single-layer and double-layer dewetting. The protrusions are larger, both laterally and vertically, for region 2, where regions 1 and 2 exhibit roughness values of 3.2 and 3.8 nm, respectively. The right panel of Figure 2.5 displays a higher-resolution micrograph of region 2.

XPS measurements on a 5 nm thick elemental Mo film after annealing to different temperatures start to show Si at 600°C as a result of silicide formation. Interestingly, despite significant dewetting and structural changes in the film morphology, XPS spectra exhibit less silicon after further annealing at 800°C. Similar behavior has been observed in other studies, where it was explained as the consequence of the partial sublimation of the silicide from the surface [83,84]. Based on this, we interpret the drop in the Si signal in our XPS-spectra as a result of the accompanying formation of a more Mo-rich silicide, Mo_3Si, which is indeed expected to be more stable at higher temperatures[76]. This change in composition provides some support to the scenario, suggested above for the difference between regions 1 and 2, in terms of the presence of at least two different silicide compositions.

We conclude that our 5 nm thick Mo film no longer covers the substrate completely at 800°C. Compared to Ru layers, Mo layers exhibit a more stable morphology at elevated

temperatures. This is due to a stronger interaction with the substrate, as a result of Mo-silicide formation at the interface. In the last chapter, we will demonstrate why Ru-silicide formation cannot provide a similar adhesion between a Ru layer and a Si substrate with a native oxide.

2.3 The influence of a molybdenum interlayer on the wetting properties of ruthenium thin films

In this section, we introduce an ultra-thin Mo thin film as an anchoring layer between a Ru top layer and the oxidized Si substrate, in an attempt to maintain the benefit of the high oxidation resistance of a Ru capping layer up to higher temperatures.

Mo films with a thickness of 3 nm were deposited on Si(100) substrates with a native oxide, which was followed by the deposition of a 3 nm Ru film without breaking the vacuum of the sputter deposition chamber. A DC power supply was used for the depositions of both materials. Details regarding the sample preparation can be found in the experimental-methods section of Chapter 1. After the deposition of the films, thicknesses were confirmed by profilometer and AFM measurements. Below, I describe the evolution of the bilayer thin film with increasing temperature, as followed by SEM, AFM and XPS. We will find that the bilayer displays superior thermal stability when compared with thin films consisting of only Mo or only Ru. In addition to this, we observe the formation of flower-like structures on the surface residing on pyramidal pits that form spontaneously inside the substrate, when the bilayer samples are annealed at 700°C.

Figure 2.6 displays SEM micrographs of the bilayer on Si(100) with a native oxide at various annealing stages, where the samples were kept at each temperature for a duration of 60 minutes. The first image shows the freshly deposited bilayer film that is characterized by a fine texture. The XPS spectrum confirmed that the surface is fully covered by Ru, as we concluded from the absence of Si or Mo signals. For the as-deposited and annealed samples, the SEM micrographs display sufficient contrast to distinguish the differently oriented grains of a polycrystalline structure of the topmost layer, i.e. the Ru, in the bilayer configuration.

The first AFM image in Fig 2.7 for the as-deposited bilayer film also demonstrates the relatively flat starting structure of the polycrystalline film. We measured an average lateral grain diameter of 7.1 nm, see Figure 2.9, and a surface roughness of 0.35 nm, very similar to the values that we found for the pure Mo film that we investigated in the previous section.

The combination of the SEM and AFM micrographs demonstrates that the surface roughness is decreased by annealing up to a temperature of 300°C, which is followed by progressive roughening at the higher annealing temperatures. This goes hand-in-hand with the reorganization of the top layer into larger structures that suggest a coarsening of the film into larger grains with well-developed grain boundary grooves. This scenario is reminiscent of that for the pure Mo film, for which a detailed explanation was given in the previous section. However, for the pure Mo film, we observed the initial fine texture and uniform morphology to evolve into a more visible and distinctive texture already at 300°C, whereas the bilayer starts to show this evolution only above this temperature. This suggests that the bilayer film exhibits better stability even at this stage. Figure 2.9 presents the evolution of the correlation length and the surface roughness as a function of temperature. The roughness initially decreases up to an annealing temperature of 100°C, after which it remains nearly constant up to 300°C, before exhibiting the familiar, progressive roughening, that was also suggested by the coarsening in the SEM micrographs. Over this temperature range, the correlation length shows a modest increase, which we attribute to the increase in grain size.

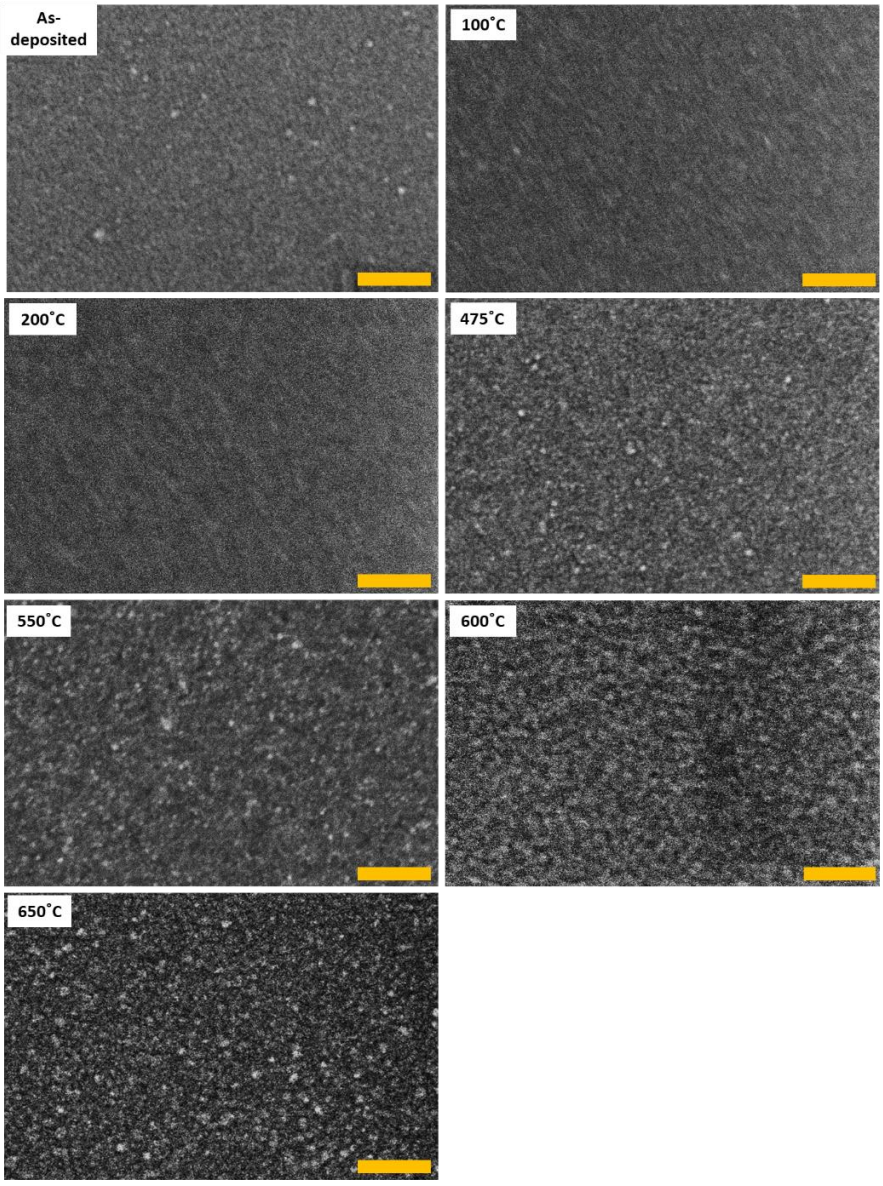

Figure 2.6 *SEM images obtained for the Mo + Ru bilayer structure on a Si(100) substrate (with native oxide), after annealing at various temperatures. The dimensions of the images are indicated by the yellow scale bars, which are all 100 nm long.*

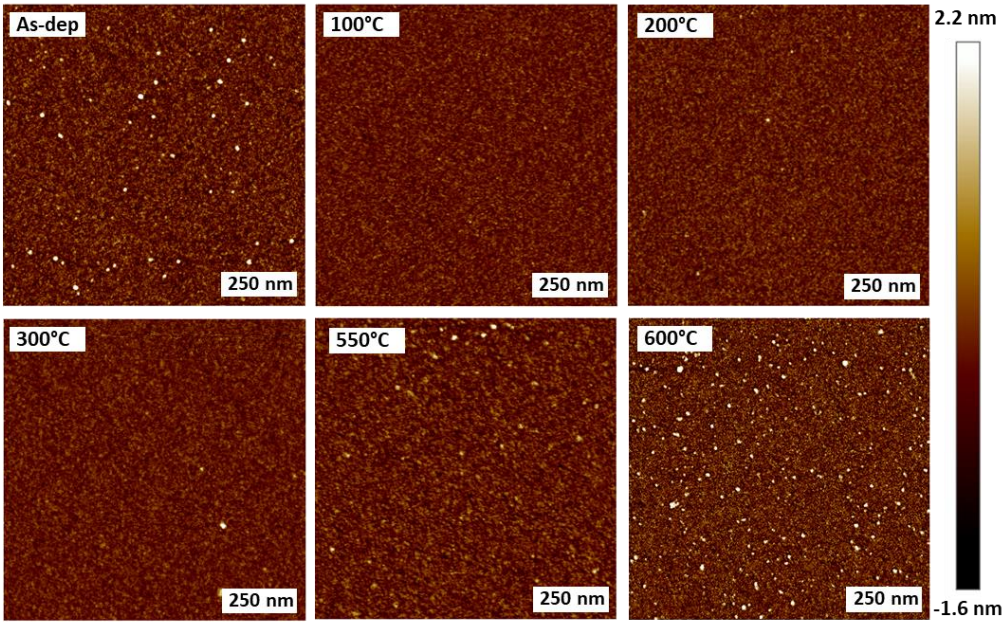

Figure 2.7 *AFM images for the Mo + Ru bilayer structure on an Si(100) substrate (with native oxide), after annealing at various temperatures. All images have dimensions of 1 µm × 1 µm and they are all displayed with the same conversion of height variations into colors, as indicated by the color bar on the right.*

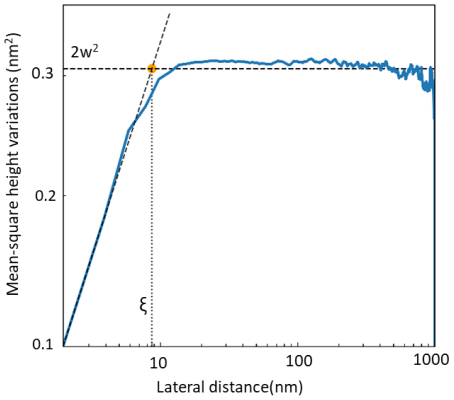

Figure 2.8 *Height correlation function of a freshly deposited Mo-Ru bilayer on a Si(100) substrate (with native oxide). The dashed lines represent the corresponding fits for the asymptotic and power-law regions where w is the surface roughness (RMS) and x is the correlation length. The height correlation values were measured from an AFM image with an RMS roughness of 0.39±0.06 nm.*

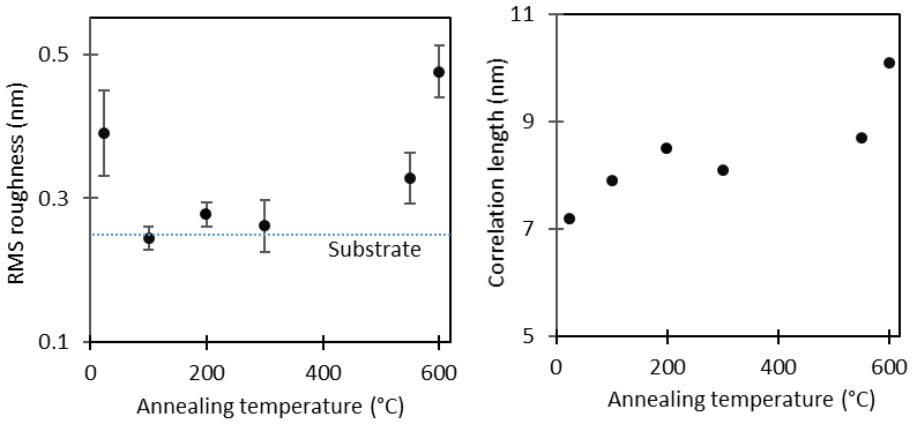

Figure 2.9 *Surface roughness and correlation length for a Mo + Ru bilayer structure on a Si(100) substrate (with native oxide) as a function of annealing temperature, obtained from the height-correlation-function analysis of the AFM images in Figure 2.8.*

Apart from the modest evolution of the grain size, the bilayer film preserved its initial structure up to 600°C. Significant changes were observed, when the sample was annealed at 700°C for an hour. Figure 2.10 displays SEM and cross-sectional SEM images, in which we see that the flat surface is interrupted by bright, spiky, circular structures. We refer to these structures as 'nano-flowers'. In its center, each nano-flower contains a square structure that appears darker, indicating a reduced secondary electron emission from these regions. All squares are in the same orientation, which, together with their symmetry, indicates that their origin is directly connected to the lattice structure of the underlying substrate. We will come back to this point later.

Additionally, we inspected the sample with AFM. The image in Figure 2.11 demonstrates that the nano-flowers have diameters between 0.4 and 1.0 μm and that they are protruding approximately 4 to 8 nm above the rest of the surface. In the AFM-images, the center of each nano-flower is on average somewhat higher (order of magnitude 1 nm) than the rest of the flower). Interestingly, the AFM-images show no square structure in the middle of each nano-flower, which would be the equivalent of the dark square that each nano-flower has in the SEM micrographs. This means that these squares in the SEM images are not a topographical surface feature and suggest that they reside below the surface. Indeed, whereas the AFM tip only probes the very surface, the SEM's electron beam penetrates several nanometers deep into the sample and the secondary electron emission image originates within the bilayer film and even deeper, i.e. inside the substrate.

This is why we proceeded to investigate the cross-sectional profiles of the sample with SEM. A diamond pen was used to make a scratch on the rear side of the substrate along one of the <110> crystal directions and modest pressure was applied to break the sample. This enabled us to take a side view of the sample, simply by using the SEM to image the cleavage plane, perpendicular to the surface. Examples of such cross-sectional SEM images are shown in the bottom two panels of Figure 2.10. These reveal that each square structure is actually the base of an inverse pyramidal pit inside the substrate. The silicon atoms that originally were inside these regions, must have migrated out of there. To our surprise, all flower structures, including those that were intersected by the cleavage plane, survived the breaking, even though these are nanometer thin, freestanding structures, which testifies to their mechanical strength.

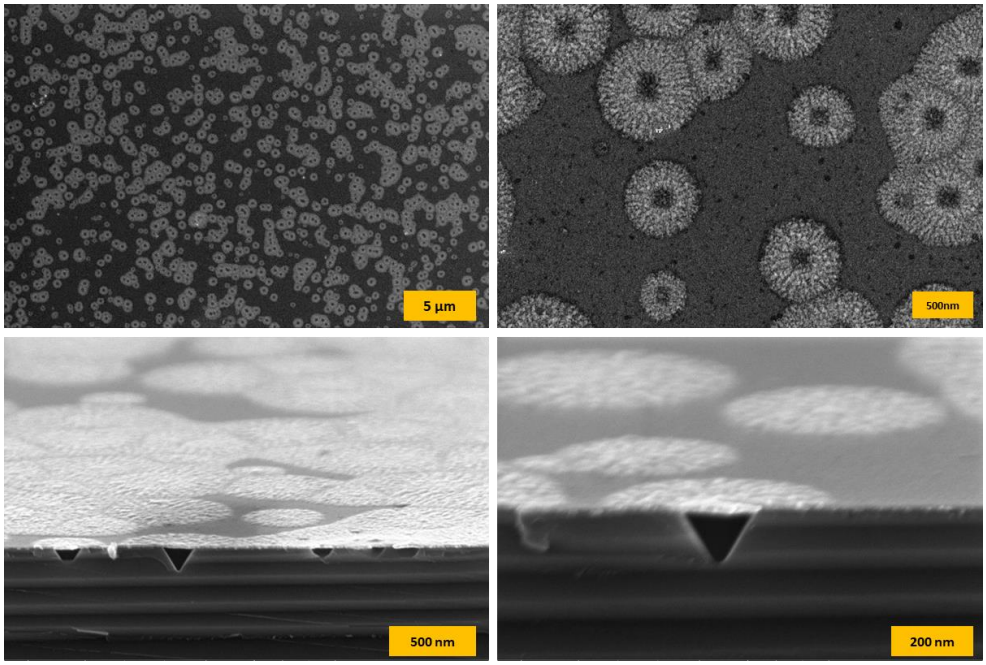

Figure 2.10 *SEM micrographs of the Mo + Ru bilayer structure on a Si(100) substrate (with native oxide) after annealing at 700°C for an hour. The upper and lower panels show regular and cross-sectional SEM images, respectively. The dimensions of the images are indicated by yellow scale bars.*

A schematic impression of the structure of these flowers can be found in Figure 2.12. We already mentioned the strong interaction between Mo and Si atoms. Even though the bilayer was deposited on a native oxide of silicon, in order to prevent silicide formation, the thickness of the oxide was only around 1.5 nm and the high temperature appears to have provided sufficient atomic mobility for atoms to cross this ultrathin barrier. The cross-sectional SEM images indicate that silicon atoms are the dominating diffusing species, resulting in the transformation of the Mo and possibly also the Ru film into a silicide. The observation that this transformation did not take place uniformly over the entire surface, indicates that the transport of Si atoms from the substrate to the metal bilayer must have taken place via a limited number of defects in the native oxide, which could either be pre-existing defects or defects that were induced by the stress that resulted during the annealing from the large difference in the coefficient of thermal expansion between SiO_2 and Mo. The local 'supply' of Si atoms originating from these defects at the oxide-metal interface, would then naturally explain the circular shapes of the nano-flowers, compound formation then proceeding in the form of radially expanding reaction fronts, each one starting independently at the defect site in the center of a circle. This scenario explains the overall circular shapes of the nanoflowers, but not their internal spike-like patterns. A few extra words are in place on the shape of the inverse pyramidal craters. We have measured the angles of the side walls of these structures to be consistent with the angle of 54.7° of the {111) lattice planes of the Si crystal with respect to the (100) surface plane. The {111} surfaces are the lowest-free-energy surfaces of Si[85–87], making the inverse pyramids the lowest-free-energy pits in a Si(100) surface. Indeed, inverse pyramidal craters are well-known etching structures in Si(100).

By combining the regular and cross-sectional SEM micrographs with the two-dimensional AFM height profiles, we discovered that the volume of the nano-flowers is in agreement with the volume of the underlying inverse pyramidal pits, with an error margin of only 2%. In this calculation, we assumed that the compound formed is $MoSi_2$, which seems most appropriate, given the annealing temperature. The other molybdenum silicide compounds, in particular Mo_3Si, would be expected to form only at higher temperatures of at least 1000°C[76]. The volume match of the pyramids and the nano-flowers provides additional confidence that the missing silicon ended up in the flowers as $MoSi_2$ and no material sublimed from the sample at 700°C. The densities of the materials that were used for this calculation and the other compounds that may potentially form are presented in Table 2.1.

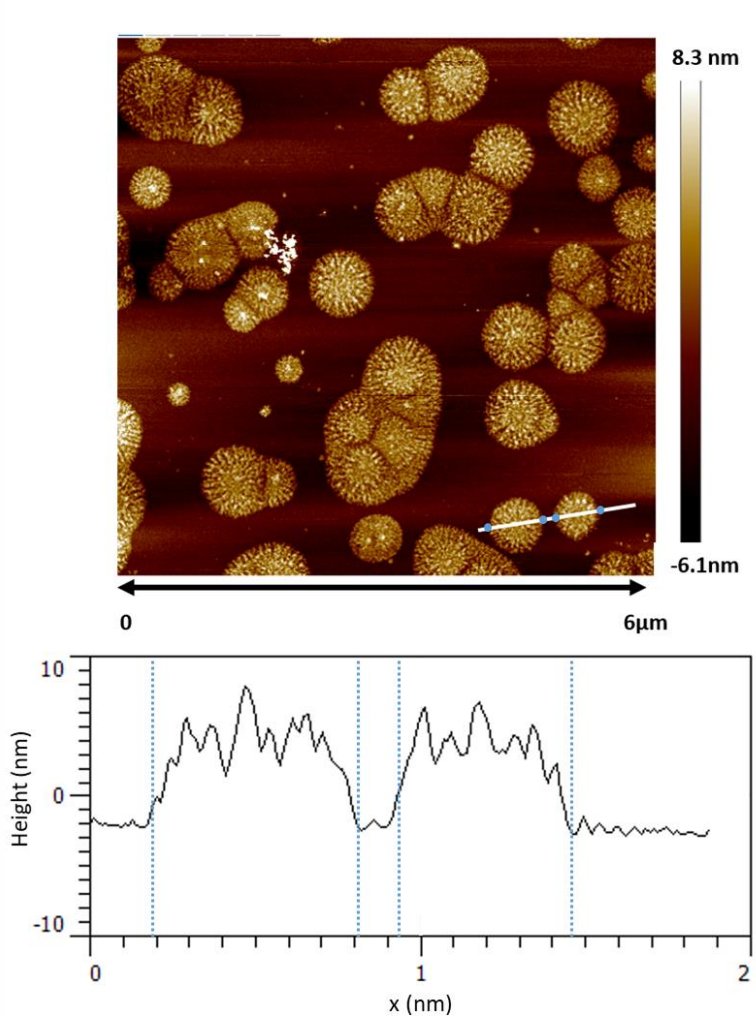

Figure 2.11 *AFM image of the surface of the bilayer thin film after annealing at 700°C for an hour. The AFM image reveals a pattern of partly overlapping nano-flowers. The bottom figure shows the height profile corresponding to the white line in the upper panel, across two neighboring nano-flowers. Blue dots on the white line correspond to the borders of the nano-flowers that are indicated as vertical dashed lines in the height profile.*

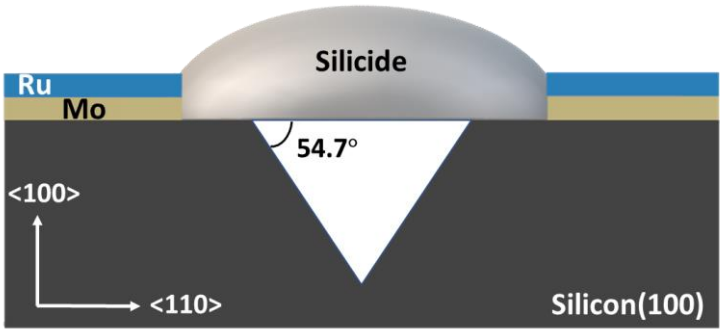

Figure 2.12 *Schematic illustration of the structure of a nano-flower in combination with the underlying inverse pyramidal pit, formed after annealing at 700°C of a Mo + Ru bilayer on Si(100) (with native oxide).*

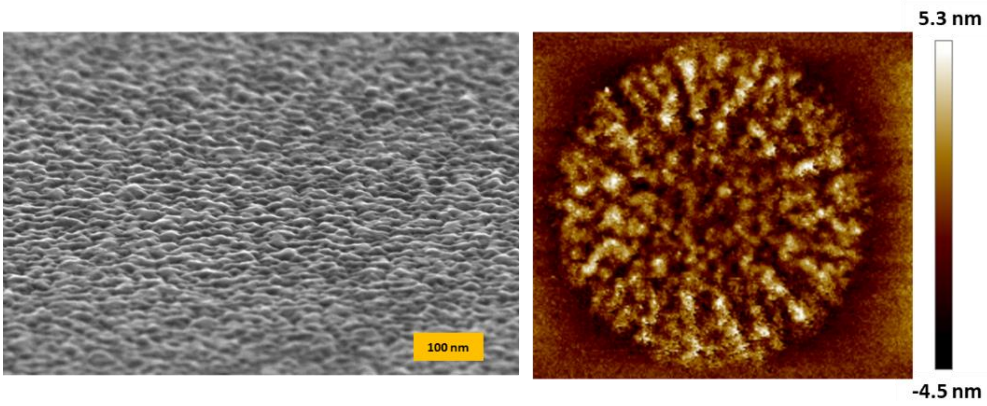

Figure 2.13 *Two images of nano-flowers obtained by annealing the bilayer at 700°C. The left panel shows an SEM image of a nano-flower at a sample tilt angle of 30°. The AFM image on the right emphasizes the spikey nature of the nano-flower. The dimensions of the SEM image are indicated by the scale bar. The AFM image has a dimension of 1 µm × 1 µm and the color bar on the right indicates the conversion to heights.*

Material	Density (g/cm^3)
Mo	10.28
Ru	12.45
Si	2.33
MoO_3	4.69
MoO_2	6.47
RuO_2	6.97
SiO_2	2.65
SiO	2.13
$MoSi_2$	6.26
Ru_2Si_3	6.96

Table 2.1 *Densities of possible materials to be considered as potential compounds resulting from the annealing of the Mo + Ru bilayer on the silicon substrate (with native oxide).*

Figure 2.14 shows the surface composition of the Mo + Ru bilayer sample on the Si(100) substrate, measured by XPS. Only modest changes in surface composition are seen up to 600°C. From room temperature up to 600°C, the XPS spectra indicate the surface to consist of nearly pure Ru with a very low and slowly rising fraction of Mo. This modest increase might not even have to be due to the migration of Mo through Ru, but it could even reflect the effect of the grain boundary grooving of the Ru overlayer. When the temperature is further raised to 700°C, the XPS spectra reveal a significant amount of Si, which is enriched at the surface at that temperature to as much as 19%. Also, the surface concentration of Mo has increased at that temperature, to 12%, while that of Ru has dropped to 69%. From the XPS spectra, it is difficult to conclude whether or not Ru is still fully covering the surface at 700°C, but, in combination with our earlier observation that the missing Si from the pyramidal pits formed part of the nano-flowers, it is now safe to conclude that these structures consist of at least Mo and Si and, possibly, Ru. $MoSi_2$ is known to form within the temperature range of 520-800°C, which would be consistent with the volume consideration, discussed above. The reduced Ru signal could indicate that at least part of the Ru overlayer has engaged in a ternary compound with the Si and Mo.

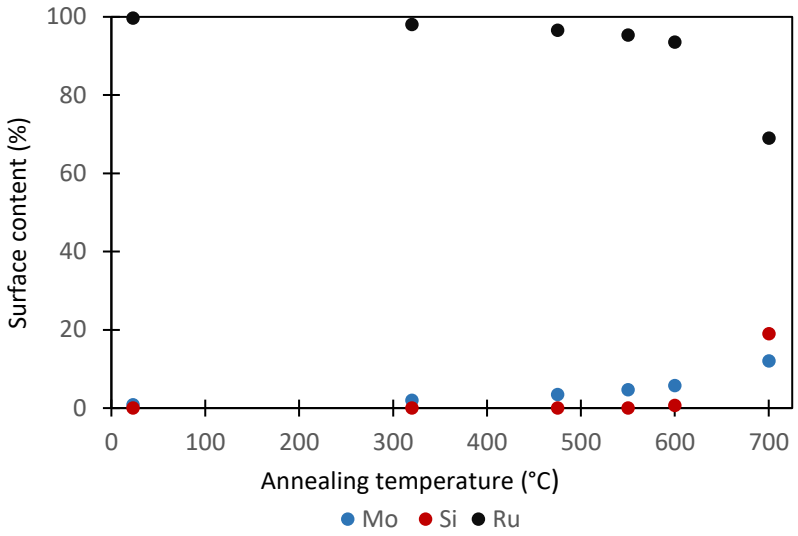

Figure 2.14 *XPS-measurements of the surface composition of the Mo + Ru bilayer on Si(100) substrate as a function of annealing temperature, at which the samples were kept each time for 60 minutes. Grey, blue and orange symbols represent Ru, Mo and Si, respectively.*

Additional annealing at 750°C was found to lead to almost complete nano-flower coverage of the surface, as shown in Figure 2.15. The SEM images still show inverse pyramidal pits beneath the nano-flowers, while the AFM topography images demonstrate that the nano-flower heights and the internal height variations due to the spiky shapes remain very similar to those at 700°C. The shapes of many of the nano-flowers deviate from circular at the highest temperature, due to the nearly complete filling of the surface with these structures.

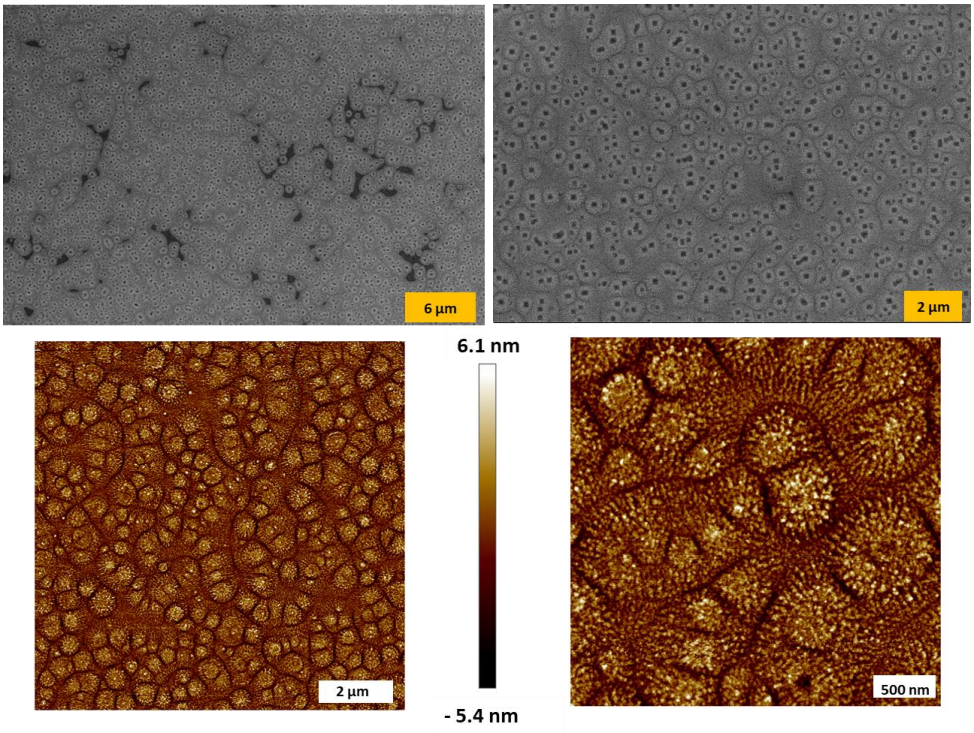

Figure 2.15 *The Mo + Ru bilayer on Si(100) after annealing at 750°C for an hour. The upper and lower panels show SEM and AFM images, respectively. The two AFM images are displayed with the same conversion of height variations into colors, indicated by the color bar. The dimensions of the images are indicated by scale bars.*

We further increased the annealing temperature to 800°C. Figure 2.16 presents SEM and AFM images after annealing at this temperature for one hour. After this treatment, the surface is fully covered by nano-flowers. Their shapes are drastically distorted by their coalescence into a tightly packed network, making it increasingly difficult to distinguish the individual structures. In addition, even though the craters can still be observed, most of them are severely distorted and no longer show a square basis. The AFM images also show the strong deviation of the nano-flowers from well-defined, circular shapes, but the height profiles exhibit nearly the same height variations as at lower temperatures, originating from the spike-like patterns. This indicates that at this temperature, the nano-flowers retain the character that we already recognized at 700°C, but that their areal density is simply higher.

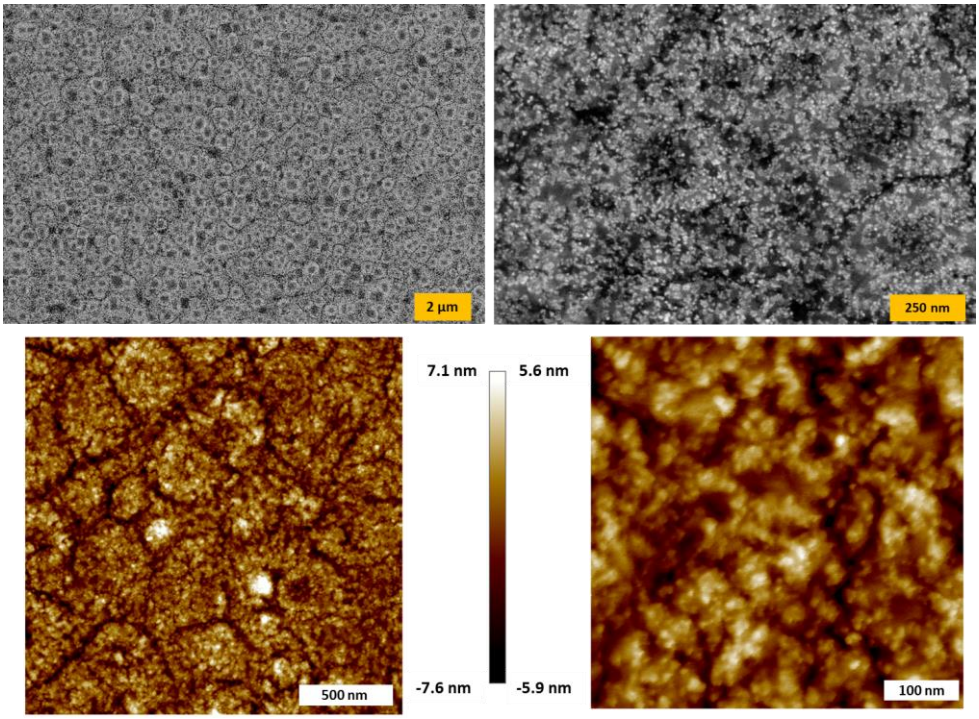

Figure 2.16 *SEM (upper) and AFM (lower) images of the Mo + Ru bilayer on Si(100) after annealing at 800°C. The dimensions of the images are indicated by scale bars and the color bar indicates the height variations in the two AFM images.*

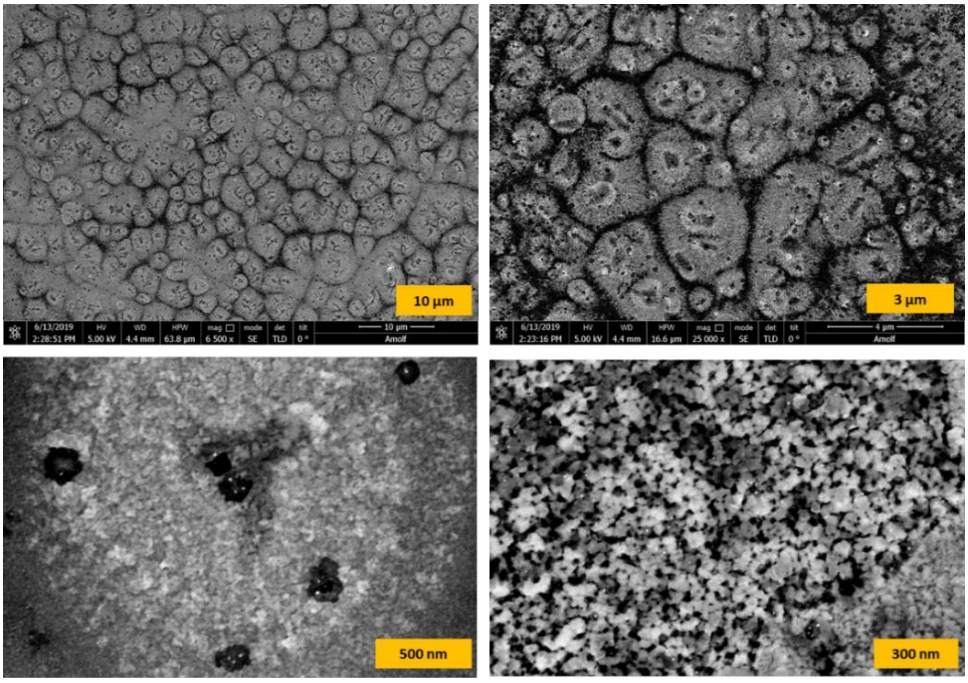

Figure 2.17 *SEM images of the Mo + Ru bilayer on the silicon substrate after annealing for 1 hour at 900°C. The dimensions of the images are indicated by yellow scale bars. The dense nano-flower pattern is interrupted by holes, both inside and outside the nano-flower clusters. The excessive surface roughness made it nearly impossible to image the surface with AFM.*

Finally, only when we annealed the bilayer sample at 900°C, did we observe the first signs of degradation, as illustrated by the SEM images in Figure 2.17. At this temperature, the surface became excessively rough, which made it impossible for us to complement the SEM images with meaningful AFM observations. In Figure 2.17, we recognize that the nano-flowers, or what is left of them, seem to form clusters, separated by relatively deep grooves. In addition, we observe holes in the film, both inside the nano-flowers (bottom left panel) and between them. This appearance of holes and the increased height differences are indicative of the first stages of dewetting at this temperature.

2.4 Conclusion

In this chapter, we explored the microstructure and thermal evolution of ultrathin films of elemental Mo and Ru as well as bilayers, Ru top on Mo, deposited on Si(100) substrates with a native oxide. DC sputter deposition provides a very flat initial surface (roughness

below 0.4 nm) with fine polycrystalline texture for all the as-deposited films. The primary purpose of this study was to follow the natural process of dewetting of a Ru layer on Si and to investigate whether an intermediate Mo layer affects this behavior. Dewetting is the inevitable fate for a thin film that has a higher surface free energy than the substrate. Unfortunately, almost all metals have a higher surface free energy than Si or SiO_2, so that most metal-on-silicon combinations are expected to undergo dewetting. In our experiments, films of 5 nm thick Ru started to develop holes at 600°C. On the other hand, Mo thin films were found to exhibit higher thermal stability and only dewet at 800°C, adopting a labyrinth morphology. For some applications, the optical properties and oxidation resistance of Ru would be desirable in combination with the higher thermal stability of Mo. This motivated us to introduce a Mo interlayer between a Ru top layer and a Si(100) substrate with a native oxide. Our expectations were based on two main arguments. First, the surface free energies of Mo and Ru are nearly the same. Since the two metals also interact well with each other, we may expect the tendency for each of them to dewet the other to be rather weak. Second, the good adhesion of Mo to Si, via the formation of an interfacial silicide makes the Mo-Si interface more robust against dewetting than Ru-Si. In combination, these elements suggest that a bilayer with a thin Ru layer on top of a thin Mo layer that is in direct contact with the (oxidized) Si substrate would combine the desired surface properties of Ru with improved thermal stability against dewetting.

Our results seem to support this hypothesis. The SEM and AFM observations demonstrate that the bilayer behaves differently from single layers of either Mo or Ru. Only at the highest annealing temperature of 900°C, did the bilayers exhibit the first signs of dewetting, whereas single Ru films and single Mo films of the same total thickness exhibit full dewetting on the same substrate already at lower temperatures, between 700°C and 800°C.

In addition to this, we observed that 5 nm thick Mo thin films develop a special morphology with circular structures at temperatures as low as 600°C. By combining SEM, AFM, and XPS, we identified these structures as regions that were converted into molybdenum silicide. The silicide formation, possibly even involving two different silicide compositions, seems to play a decisive role in the dewetting behavior at 800°C, which seems to show two distinct dewetting levels, a configuration that we refer to as double-layer dewetting.

In spite of the improved thermal stability against dewetting, also the metallic bilayer shows special behavior at high temperatures, in the form of the appearance of flower-like structures at and above 700°C, which we refer to as nano-flowers. Further inspection revealed that each nano-flower is a free-standing structure that spans over an inverse pyramidal crater in the Si(100) substrate, a well-defined etch pit with {111} faces. The Si missing from these craters was found to be accounted for by the volume of the nano-flowers, which is

consistent with a scenario in which Si is incorporated into the nano-flowers through the formation of either $MoSi_2$ or a silicide containing both Mo and Ru.

Chapter 3

GLASSES AND METALLIC GLASSES

What is the nature of the transition between a fluid or regular solid and a glassy phase? "The deepest and most interesting unsolved problem in solid-state theory is probably the theory of the nature of glass and the glass transition.

P. W. Anderson

Thin metallic films are of great importance in a wide variety of practical applications, for example requiring excellent electrical conductivity, high emissivity for infrared radiation, optical transparency, high magnetization or enhanced fracture resistance. In some of these applications, such films degrade by natural processes, which can be aggravated under operation conditions. For example, at high temperatures, a metal layer may dewet the substrate on which it resides, i.e. it breaks up into separate metal islands. Energetically, this process is driven by the differences in free energies between the surface and the substrate, that of the metal film and that of the interface between the two, while there can also be a role played by mechanical stress in the film. These free energy differences become relevant once the film has locally become so thin that its surface 'meets' the substrate. This may seem an extraordinary configuration, but we believe that such configurations occur abundantly due to the polycrystalline structure of most metal films. This polycrystallinity introduces grain boundaries that can act as the natural starting points for film break-up and dewetting. If this is indeed the case, amorphous films might provide an advantageous alternative. Even though they don't remove the

primary, energetic driving force for dewetting, they may improve the metastability of the film significantly through the absence of these natural starting points. Unfortunately, pure metals usually cannot be made amorphous in practice. The combination of atomic-scale mobilities and the energetic gain involved in crystallization almost invariably leads to structures that consist of crystalline grains, at 'best' small grains in the nanometer regime, albeit these actually introduce even more grain boundaries. One might think that the transition from polycrystalline to amorphous is gradual, but from the viewpoint of the grain-

boundary density, it is not! In order to appreciate the results in the rest of the thesis, it is important to familiarize oneself with the current level of understanding of the thermodynamics and evolution of amorphous and polycrystalline metal alloys. This is why this chapter provides an introductory overview of this rich field of research.

3.1 Introduction

Polycrystalline thin films consist of grains with different crystal orientations and therefore contain interfaces between these crystallites, known as grain boundaries. Grain boundaries are classified as 2D defects in a crystal lattice and they modify many properties, such as mechanical, chemical, electrical and thermal. For example, grain boundaries are the weakest parts in the strong structure of a crystal and they have a strong influence on yield strength. They are also preferred channels for atoms to go in and out of the material, as is essential for corrosion and oxidation[88] and effectively makes the film more reactive. At the same time, these planar defects decrease thermal and electrical conductivity. In Chapter 2, I already discussed the evolution of grain boundaries as a function of temperature. The results showed that thin films of elemental Mo and Ru exhibit grain boundary grooving, which causes the local thinning of the films and eventually hole formation. Depending on the balance between surface and free energies, this can make the film dewet on the underlying substrate, by breaking up into separate islands and leaving part of the substrate uncovered. In Chapter 2, we explored the possibility to suppress the dewetting of Ru thin films by adding an interlayer of Mo. However, this merely postpones the problem of dewetting to somewhat higher temperatures.

Our observations and those in the literature[24,89] strongly suggest that further suppression or even 'full' prevention of dewetting might be possible with films that have no grain boundaries at all and are completely free of crystalline defects. We can imagine two extreme configurations that meet these conditions. One is that of a perfect single-crystal thin film, i.e. a film in which the lattice is perfectly repeated over macroscopic distances, without local or extended defects. The alternative configuration that has no grain boundaries is that of a perfectly amorphous thin film.

Let us start by considering the first configuration. As I mentioned already, metals have a strong tendency to crystallize, which is why most metallic films are (poly)-crystalline. The step to a perfect single crystal may seem trivial, but, in practice, no method exists by which a thin metal film that is truly single-crystalline over macroscopic distances can be deposited on a typical substrate. Only in the special case that the film grows perfectly epitaxially on the substrate and that this substrate is perfectly single-crystalline itself, can one reach the desired perfection in the film, but this special case should be regarded as too restrictive for most applications. We could apply a variety of methods to increase the average grain size of a polycrystalline metallic thin film, which would decrease the density of the grain boundaries and triple points. However, this would be a far cry from the ultimate

solution and, at best, only 'postpone' the problems to higher temperatures or longer times.

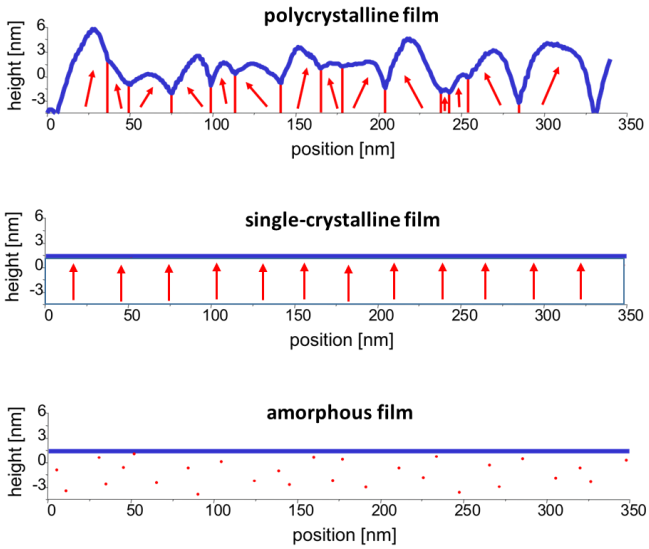

Figure 3.1 *The upper panel shows a measured STM height profile of a thin, polycrystalline metal film. Red arrows are indicating the hypothetical crystal orientations of differently oriented grains, while the vertical lines indicate the locations of the grain boundaries where the grains are joined. Note that each grain boundary is accompanied by a cusp in the surface profile, the grain-boundary groove. The middle and lower panels show a schematic illustration of a single-crystalline and an amorphous thin film, respectively. The polycrystalline film exhibits surface roughness caused by the differently oriented grains, whereas the single-crystalline and the amorphous thin films lack grain boundaries, which decreases the surface roughness significantly for these films. Image reproduced from ref 22.*

The second solution is that of a truly amorphous metallic thin film. Here, we are confronted with the strong, natural tendency of metals to order on the microscopic scale into crystallites. The accompanying increase in packing density provides a significant driving force for crystallization, while the energy barriers for atomic-scale rearrangements towards local crystalline arrangements are particularly low for metals. As a consequence, it is close to impossible to avoid crystallization either during or after the deposition of elemental metal films and these films are usually polycrystalline. This is certainly the case for the metals of interest to this PhD thesis, namely Mo and Ru. As suggested by Motorin[90] in 1983, it might be possible to cast elemental metals into an amorphous structure by quenching them from the melt with a tremendous cooling rate of at least 10^{12}-10^{13} K/s.

More recent experiments demonstrate that nanometer-size 'particles' of elemental metals that would normally crystallize in the body-centered structure can be produced as metallic glass under extreme conditions that correspond to an ultra-fast cooling rate of 10^{14} K/s [91]. The extreme process conditions make this approach unpractical, as does the particle size limitation. In addition, as explained above, one may expect these elemental, amorphous particles to be extremely prone to crystallization, which should strongly undermine the stability of their amorphous structure.

In spite of the difficulties, mentioned here, which seem to preclude the application of thin, amorphous metal films, there is a practical approach to producing such films and these films can have surprisingly good stability against degradation, e.g. crystallization. The key element in this is to step away from elemental metals and work with alloys: mixtures of two or more metals (and possibly other atom species). The 'recipe' is to mix two or more metal elements in the liquid or vapor phase, followed by rapid cooling to avoid segregation and crystallization. For the mixture, the crystalline configuration may still be energetically preferred. But this preference is reduced with respect to that of elemental solids because of the contribution of the mixing entropy of the alloy to the free energy. Hindering crystallization is that, for many compositions, crystallization is only possible in combination with segregation, leading to ensembles of crystalline grains, each enriched in one of the constituting atom species. In addition, the size difference between the atom species may frustrate the internal mobilities and, hence, slow down the diffusion that is required for crystallization significantly. And this should be seen in combination with longer diffusion trajectories that are required with respect to the crystallization of elemental metals because most crystalline alloy structures contain ordered sub-lattices of their elemental constituents and thus require more significant rearrangements and the segregated grains require even larger diffusion lengths.

3.2 Amorphous Solid

Traditionally, we classify atomic and molecular matter into three aggregation states or phases: (crystalline) solid, liquid and gas. Thermodynamically, the amorphous configuration does not represent a genuine phase. Nevertheless, it is instructive to regard it in the context of the three thermodynamic phases, as it obviously shares characteristics both with the solid phase and with the liquid phase

The classical aggregation states or phases of matter distinguish themselves from each other by the spatial arrangements of the atoms, which is accompanied by major differences in atomic mobilities. In the gas phase, the atomic density is low, atoms are in completely random positions and they exhibit ballistic motion. This behavior is extremely different for a crystalline solid, where the atoms are arranged in an ordered pattern with

long-range periodicity at a high packing density, while the diffusion coefficient is minimal. The liquid is in between. It has a relatively high density, but the structure has only short-range order and the atoms have high mobility. Often, glasses or amorphous solids are referred to as a separate (non-classical) state of matter. Even though this is strictly speaking incorrect and these solids would lower their free energies by crystallization, possibly involving segregation, they can have extreme lifetimes and thus be of genuine, practical use. The word "amorphous" originates from classic Greek and means "without shape". In our context of condensed matter physics, it refers to a non-crystalline solid, without the long-range periodicity of a crystal. When the temperature is far enough below the melting point, the viscosity can become so high that the material no longer flows and behaves as a solid, even though it lacks the long-range order of a crystalline solid and its structure is closer to that of a liquid. This transition, between the undercooled liquid and the glass configuration and vice versa, is referred to as the "glass transition"[92]. This transition is not a first-order phase transition in the Ehrenfest classification, and it is considered a second-order kinetic transition, governed by viscosity. This solid-like situation is often referred to as if it were a thermodynamic phase, for example with words such as "the glass state". In the remainder of this chapter and the rest of this thesis, I will conform myself to this jargon and adopt the same, strictly incorrect wording. In practice, the glassy structure can be reached from the liquid phase, if the liquid is cooled down rapidly enough to quench flow and diffusion more or less completely and thus avoid crystallization. For this, the temperature should be low enough to make the viscosity sufficiently high. Despite the fact that it possesses a liquid-like atomic configuration, its high, solid-like viscosity, makes that glass perceived as and referred to as a solid. In spite of the absence of long-range order, glasses may possess a high degree of short-range order with a preference for arranging into local atomic polyhedra[93].

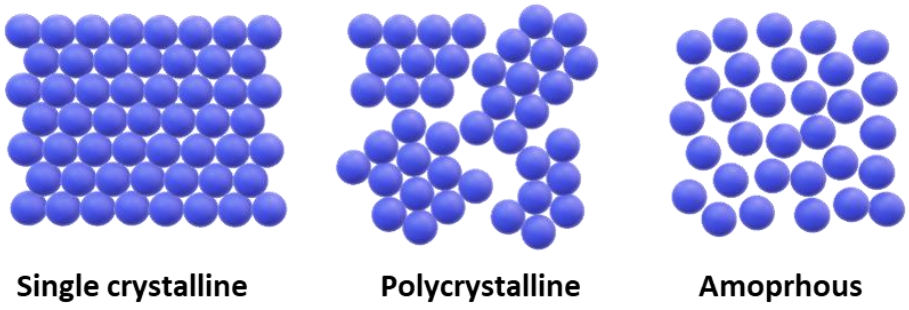

Figure 3.2 *Schematic illustration of the atomic structures in single-crystalline, polycrystalline and amorphous materials. The single crystal is characterized by long-range order, while the polycrystalline solid exhibits crystalline order up to the length scale of individual grains. The amorphous structure presents a liquid-like, random atomic stacking.*

Conventional and most common glasses are oxides, often derivatives of silica. For these glasses, the continuous random network can be formed by various types of bonds, e.g. ionic or covalent, much the same as the corresponding, regular network of crystalline solids. The special bonding character of metals[91], typically makes metallic glasses less stable with respect to crystallization than the oxides.

There is a persistent misconception that there would be no difference between glasses and amorphous materials. The case of silicon helps us to illustrate the difference. As pointed out by Poate *et al.*[94], the regular and random networks of crystalline and amorphous silicon are both based on tetrahedral, covalent bonding, with the silicon atoms being four-fold coordinated. By contrast, both liquid and glassy silicon have a higher atomic density and exhibit metallic bonding geometries, in which the silicon atoms are eight- to twelve-fold coordinated[94–96]. The glassy form is close to a quenched liquid and is very different in structure, density and electronic properties from the amorphous form.

Gupta described glasses and amorphous solids as two different classes from the perspective of thermodynamics[97]. He highlighted differences in structure and in behavior upon heating. The free energy of the glassy form is higher than that of its liquid counterpart at any temperature, but at the glass transition temperature, its free-energy-versus-temperature curve runs tangential to the corresponding curve of the liquid. The amorphous solid situation is different, and its free energy curve may go below the liquid curve at low temperatures. Gupta points out that a glass and a liquid exhibit similar short-range order, whereas the amorphous solid is distinctly different.

3.3 Formation of a glassy structure

From a conceptual point of view, metallic glasses are completely equivalent to glasses made of ceramics, oxides or polymers, as they can all be viewed as-quenched liquids. However, from a practical perspective, there is a serious difference, since the formation of a metallic glass from its melt requires significantly higher quenching rates of typically 10^{14} K/s[91]. When a liquid is cooled down, all its properties, such as free energy, specific heat, viscosity and density are progressively changing. Figure 3.3 is separated into three different temperature regimes to explain the evolution of these properties. In regime (A), the material is liquid. Regime (B) is that of the undercooled liquid or super-cooled melt. In regime (C), the material is in the fully 'solid' phase. In this regime, the viscosity is so high and the diffusion rate is so low, that the structure is effectively frozen in, even when it is not at the lowest possible free energy. Regimes (A) and (B) are joined at the melting temperature (T_m) and in the case of an alloy, this boundary is determined by the freezing temperature (T_f). This reflects that for alloys, crystallization in regime B is often accompanied by segregation. In practice, this leads to the behavior that the freezing does not take place

at a single temperature, but over a temperature range, commencing at T_f. Such a freezing temperature range is observed for most alloys but not for pure metals. For simplicity, a freezing range is not shown in Figure 3.3. Regimes (B) and (C) are separated by what is referred to as the glass-transition temperature (T_g). In fact, the transition occurs over a range of temperatures, which can be surprisingly narrow, over which the viscosity changes significantly, thus changing the behavior of the material from that of a viscous liquid, above this temperature range, to behavior that has many of the characteristics of a solid, below, even though the internal organization of the material is hardly changing over this temperature range.

In order to bring material into the glass state, the cooling rate should be high enough to prevent nucleation of crystallites, while traversing regime (B). The driving force for crystallization is proportional to the amount of undercooling in regime B.

Figure 3.3.a shows how the volume per unit mass evolves as a function of temperature. In temperature regime A, the specific volume of the liquid decreases continuously with decreasing temperature down to T_m. Starting at high temperatures, we recognize that the expansion coefficient of the liquid is significantly higher than that of the crystal. The 'normal' situation is that at the freezing temperature, there is a sharp drop in the specific volume as the liquid crystallizes, which is followed, as cooling is continued below T_m, by a further decrease in volume, typically at a lower pace than for the liquid. If crystallization is avoided and the liquid is undercooled below T_m, the specific volume follows a completely different curve in region B, which is a continuation of the curve for the liquid in region A.

Figure 3.3.c shows how the free energy per mole, G, varies in this process. As the temperature of the liquid is lowered in temperature regime A, the free energy increases. Close to T_m, this variation can be approximated as linear, simply due to the reduction of the entropic contribution to the free energy with decreasing temperature. T_m is the temperature at which the curves for the liquid and the crystalline solid intersect. As a result, in region B, the lower-free-energy choice is for the solid and a first-order phase transition is associated with T_m. If, however, the transition is avoided, the system stays on the upper free-energy curve in region B and the liquid is supercooled. In a sense, region B should be regarded as the 'unsafe' temperature regime for this undercooled situation. As soon as the system finds a way to nucleate a small crystallite, the mobilities are sufficiently high to transform the melt into a crystalline solid. The latent heat of solidification that is released in this process, provides additional assistance for this process. If, however, the cooling rate is high enough for the system to traverse temperature region B completely without such nucleation, the configuration of the undercooled liquid is frozen in. This is caused by the strong temperature dependence of the viscosity of the (undercooled) liquid, which becomes so high when this liquid approaches T_g, that apart from vibrations, atomic motion

effectively stops (note that the viscosity in Figure 3.3.b is displayed on a logarithmic scale). Flow and diffusion then take place on prohibitively long timescales so that they can be ignored from a practical perspective. In this way, the liquid-like configuration demonstrates a long lifetime, which makes the medium behave as if it were in a thermodynamically stable, rigid, i.e. solid phase. At which temperature precisely the configuration can be considered as frozen in, depends on the cooling rate at which region B is traversed. Faster cooling results in a higher effective temperature at which the last atomic-scale rearrangements take place, than slower cooling. The glass transition is not a thermodynamic phase transition and the associated transition temperature is not sharply defined; it depends on the cooling rate. Below the glass transition, in region C of the temperature scale, the subtle internal relaxations that would take place in the supercooled liquid, if it had enough atomic-scale mobility for such rearrangements, would make the hypothetical free-energy curve continue along the metastable path, indicated by "ideal glass" in Figure 3.3.c. However, the nearly complete absence of such relaxations in the glass, forces the free energy to actually evolve along a higher path. The sequence, described here, is also reflected in the variation of the specific volume of the material. Whereas the ideal glass would continue to shrink strongly down to the lowest temperatures, the absence of internal rearrangements (see above) below the glass transition reduces the expansion coefficient of the real glass to a modest value, similar to that of the crystalline solid. The dependence of the effective transition temperature on the cooling rate therefore also makes the density of the resulting glass vary with that cooling rate, a higher rate leading to a lower density of the glass, as has been described in detail for $Pd_{40}Cu_{30}Ni_{10}P_{20}$ metallic glasses by Hu et al.[98].

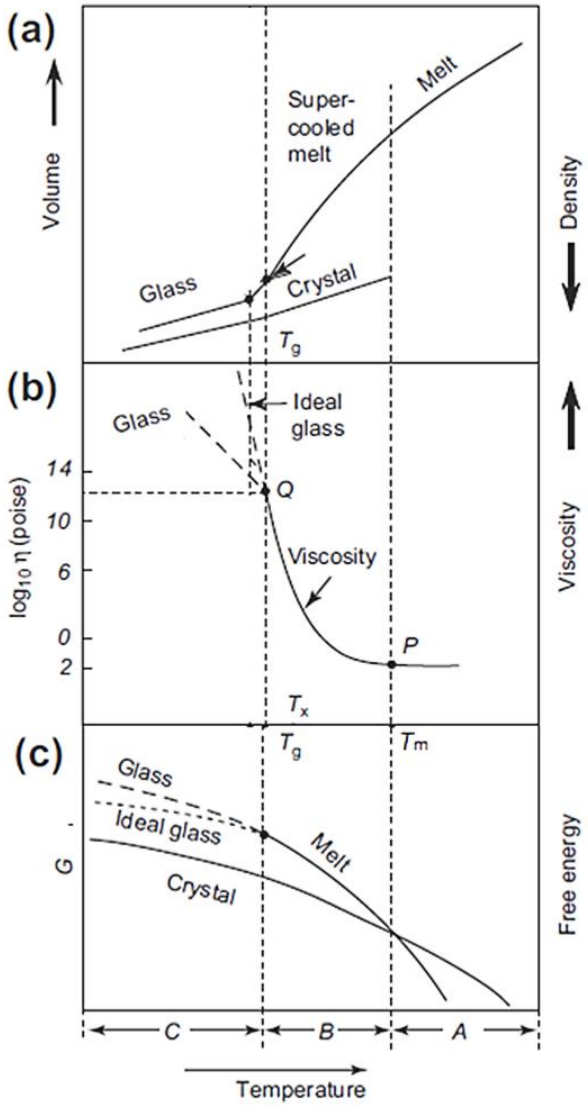

Figure 3.3 *Evolution of several physical properties from liquid to crystal or glass as a function of temperature. (a) Specific volume, (b) viscosity, (c) free energy. Whereas the transition temperature Tm between the crystal (region B) and the liquid (region A) is well defined, the glass transition temperature Tg that separates regions C and B is not sharply defined and depends on the cooling rate at which region B is traversed. The rate of cooling also determines the final atomic structure99. Figure adapted from ref. 99.*

3.4 First metallic glasses

Amorphous metallic alloys of silver and copper were reported for the first time in a study in 1960 by P. Duwez et al[100]. X-ray diffraction scans from the alloys showed no sharp peaks, as one usually obtains from crystalline phases. Instead, a broad 'halo' was observed, which is since then regarded as the diffraction signature of a liquid-like structure. In the same year, Klement et al. from the same group reported another amorphous alloy, AuSi, obtained by quenching from the liquid phase[101]. Both studies demonstrated that avoiding the nucleation and growth of the crystalline phase can be achieved in metal alloys. Since then, many other metallic glasses have been obtained. These discoveries involved further pioneers in this field of metallurgy and materials science, such as H.S. Chen and D. Turnbull[102]. They pointed out the resemblance, especially for the changes in specific heat and viscosity at the glass transition temperature of metallic glasses (MGs) to non-metallic glasses, such as silicates, ceramic glasses and polymers.

In spite of this interesting development, these first-generation MGs came with severe limitations, such as the maximum object sizes that could be cooled into the glass form, that were in the order of mere micrometers, and the required high quenching rates, that were still in the order of 10^5–10^6 K/s. Note, that the maximum cooling rate that is achieved in practice, is limited by the surface-to-volume ratio. As a consequence of these limitations, the MGs were initially produced only in small batches and in geometries with a very high surface-to-volume ratio, such as thin ribbons, thin wires, and thin films.

All these developments in MGs paved the way for the first *bulk* metallic glass (BMG). The term BMG is used for MGs that can also be obtained in geometries with less extreme surface-to-volume ratios. A BMG usually contains three or more elements and requires a lower cooling rate, so that it can be produced in much thicker forms. Consequently, in contrast to the traditional MGs, BMGs remove the restriction on the surface-to-volume ratio and do not require special shapes, such as thin ribbons and thin wires. We should note that there is no sharp distinction between BMGs and MGs, the difference being mostly associated with the practically achievable length scale rather than with truly physical properties. The first BMG was achieved with a Pd-Cu-Si alloy[103], of which a millimeter-diameter, glass rod could be obtained at a relatively low cooling rate of 10^3 K/s. Other BMGs followed with even larger thicknesses, such as amorphous Pd-Ni-P[104,105]. $Pd_{40}Cu_{30}Ni_{10}P_{20}$ can be made at the largest cylinder diameter, known to date, of 7.2 cm[106], which is in strong correlation with the glass-forming-ability, a concept that will be introduced later. The sizes at which metallic glasses can be formed are still significantly below those for non-metallic glasses. Progress in the development of MGs and BMGs gradually led to increased interest in amorphous metallic alloys and their potential applications.

In view of its relevance to potential applications, part of the research on MGs aims for the deposition of thin films of these materials. Early work on thin-film metallic glasses (TFMGs) only focused on immiscible binary systems, which cannot be produced by conventional methods to obtain MGs and BMGs. Leamy and Dirks succeeded in the co-electron-beam deposition of several rare-earth and transition-metal metallic glasses[107]. Other physical vapor deposition methods followed. Rivory and Frigerio used sputter deposition from an alloy target to grow thin, amorphous Cu-Zr films[108]. Chu et al. reviewed the early TFMG systems and their properties in detail[109]. In a later stage, it was found that sputter deposition can be used to achieve concentrations of elements in an amorphous alloy beyond the regular bulk solubility limits and that the resulting alloy can have a higher glass-forming ability (GFA)[110–112]. The glass-forming ability of a material is a qualitative indication of its metastability as a supercooled liquid and of the ease with which it can be made to traverse region B from T_m to T_g in Figure 3.3 and arrive in the glassy 'phase', without the nucleation of crystallites. A quantitative parameter that is connected to the GFA is the minimal or critical cooling rate (R_c), with which the liquid or vapor has to be cooled to achieve this.

The cooling that one should associate with the atom-by-atom (sputter)-deposition of thin films proceeds at the maximum possible rate, due to the extreme surface-to-volume ratio for each individual atom that arrives at the surface of the growing film. The use of sputter deposition not only increases the number of combinations of elements that can form a glassy structure, but also widens the ranges of composition over which the alloys can be made to form an MG.

Obviously, R_c depends very strongly on the width of region B, which is at the basis of the so-called Turnbull criterion that crystallization of the supercooled melt can be avoided when the reduced glass transition temperature T_{rg} is above a certain value.

$$T_{rg} \equiv \frac{T_g}{T_m} > 2/3 \quad (3.1)$$

This rule of thumb is also known as the 2/3 law[113,114]. This criterion has been useful in the search for many MGs and BMGs. In addition to Turnbull`s rule, other criteria have been proposed to predict the GFA of metallic glasses[115–119]. Inoue et al. show the relation between the glass transition temperature and the onset crystallization temperature (T_x)[120], which is the heating-rate dependent temperature at which crystallization starts when the MG is warmed up (See Sect 3.10). $\Delta T = T_x - T_g$, can be regarded as a practical temperature process window for the supercooled melt. These studies were followed by empirical rules for the achievement of a high GFA, proposed by Inoue[121] and Johnson[114];

1) Multicomponent alloy systems work best and should preferably contain three or more elements.
2) Differences in the atomic sizes of the constituting elements noticeably contribute to the GFA when they are 12% or larger.
3) The alloy should have a strong preference to remain atomically mixed, which means that the enthalpy of mixing of the elements in the alloy should be negative.
4) The system should exhibit a relatively low eutectic temperature in order to satisfy Turnbull's criterion for T_{rg}.

Greer refers to the three-or-more-element concept of the first of these rules as "*confusion by design*"[122] and states that including more elements in the alloy enhances the GFA by reducing the stochastic probability for viable crystal structures to form spontaneously within the supercooled liquid. The large number of configurations that can be adopted locally within the melt simply outnumbers the few configurations that could serve as crystalline nuclei. This entropic advantage not only reduces the free-energy advantage of the crystalline phase but also greatly suppresses the nucleation rate of the crystal from the supercooled melt. Inoue and Takeuchi add a further aspect to this explanation, which is an additional stabilization of the supercooled liquid by the formation of non-trivial amorphous configurations with higher packing densities[123,124]. The second criterion is largely originating from the frustration of the atomic-scale motion deriving from the size differences. In addition, large differences in size also reduce the energetic preference for solid solutions of atoms from the alloy into the regular lattices of individual constituents, thus severely restricting the solubility limits. This frustrates the crystal lattices that could form and reduces the free-energy disadvantage of the glassy state[114].

The third rule is the basic thermodynamic requirement that the combination of elements lowers its free energy by mixing uniformly. In the case of positive enthalpy, the mixture would tend to phase separate, which would work against glass formation. We will address the fourth criterion in the next section.

Finally, there are some exceptions to the above, empirical rules. Among these are the unique GFAs of Al-rare earth metals MGs with $T_{rg} < 0.5$[125] and some binary systems, such as Ni-Nb[126] and Cu-Zr[127].

3.5 Glass formation and the eutectic point of binary alloys

Why glass formation seems only possible for metallic alloys of specific compositions still remains to be explained. This is related to the last of the four rules of Inoue and by Johnson, namely that the system should have a deep eutectic, i.e. a low eutectic temperature. Due to the entropy of mixing, alloys always have melting temperatures below the melting

points of the separate components in the alloy[128]. The eutectic temperature is the lowest melting temperature that can be achieved as a function of the precise composition of the mixture, see Figure 3.4. The eutectic point in this binary phase diagram is defined by the combination of the eutectic temperature and the corresponding eutectic composition.

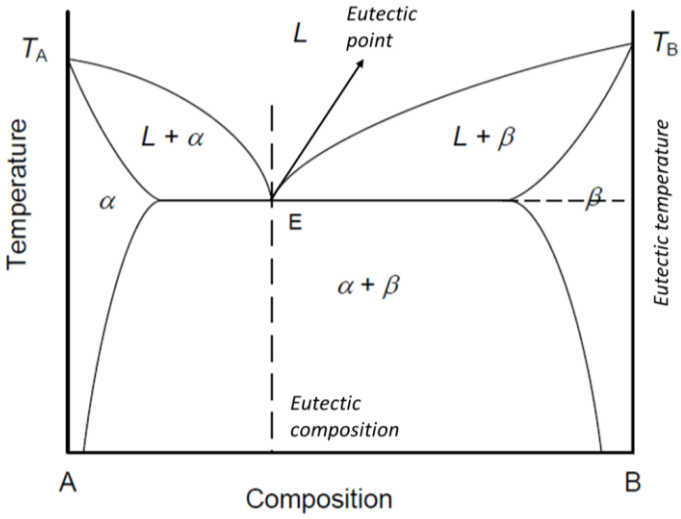

Figure 3.4 *Binary phase diagram for hypothetical alloys of elements A and B, illustrating the various phases and combinations of phases, as well as the eutectic composition, eutectic temperature and the eutectic point. At higher temperatures, the alloy is in the liquid phase (L) and all compositions are stable. At sufficiently low temperatures only phases α and β are stable. These are solid solutions of B-atoms in a crystalline A-matrix and of A-atoms in a crystalline B-matrix, respectively. In the three regions that show combinations of phases, the system is unstable and tends to decompose into the two neighboring stable phases, e.g. all points in the "α + β" region of the diagram should tend to segregate into a fraction of α and a fraction of β. Image modified from ref.129.*

Cohen and Turnbull were the first to propose a correlation between the eutectic point in the binary phase diagram and the composition for which a binary amorphous alloy can be obtained most readily[130]. Their suggestion is strongly supported by a simple kinetic argument. The eutectic point corresponds to the minimum temperature where the alloy can still be stable in a liquid form. Therefore, this is the point in the liquid part of the phase diagram that is closest in temperature to the glass transition. In other words, for the eutectic composition, section B in Figure 3.3 is the narrowest, the relative glass transition temperature T_{rg} is the highest, and the required critical cooling rate R_c is the lowest. Several experimental studies provided evidence in favor of this argument[131–133],

demonstrating that the glass-forming region in the phase diagram is indeed located at and around the eutectic composition, even though alloys are also known that do not satisfy this criterion[134–137].

Related and competing with the formation of an MG at or close to the eutectic composition, is the so-called 'coupled growth', where the alloy does not segregate into separate, macroscopic α and β grains, but adopts an alternative, symbiotic crystallization route, in which a superstructure emerges of simultaneously growing, microscopic α and β regions, typically in the form of thin lamellae, as seen in Figure 3.5. This type of structure is referred to as a 'eutectic structure'. The region in the temperature-composition diagram where this coupled growth takes place, called the 'coupled growth zone', is determined by the competition between the growth speeds of segregated α and β crystallites on the one hand and coupled, eutectic structures on the other. Here, we view the simple case of a binary mixture, for which this zone is more or less symmetric around the eutectic composition, knowing that in some cases, it is strongly skewed, with the coupled structure appearing at compositions that differ from the eutectic composition for temperatures sufficiently far below the eutectic temperature. Figure 3.6.a shows a typical binary phase diagram for eutectic alloys[138].

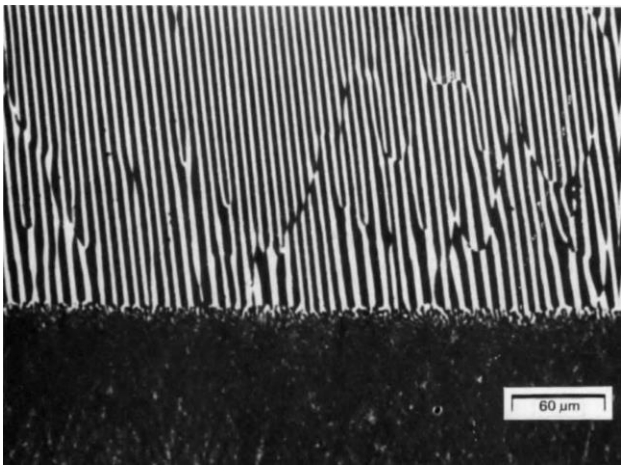

Figure 3.5 *Eutectic growth of quenched Al-CuAl2 alloy. Image reproduced from ref. 139.*

Ma et al. investigated the glass-forming ability of Pd-Cu-Ni-P and La-Cu-Ni-Al alloys that have symmetric and asymmetric coupled eutectic zones, respectively. They found that, whereas the critical cooling rate for glass formation is lowest at the regular, eutectic composition of the Pd-Cu-Ni-P alloy, it has its minimal value at an off-eutectic composition for the La-Cu-Ni-Al system[138,140].

To understand the influence of the coupled zone and the eutectic composition on the glass-forming ability, we first pay attention to the nucleation and crystal growth in the alloy. The eutectic coupled zone determines the growth characteristics, which can lead either entirely to α and β crystallites, or entirely to eutectic structures or combinations of the two, based on the growth conditions, most importantly temperature and composition[139]. Figure 3.6.b illustrates the typical temperature dependences of the growth velocities of the eutectic structure and separate α and β crystallites, for a composition in the coupled zone. At sufficiently high temperatures, growth will be fully eutectic. Figure 3.6.c shows how strongly this changes with composition. If we move to an off-eutectic composition, for example to the right, the temperature at which β-crystallites can form, increases strongly and so does the growth velocity of these crystallites.

Up to this point, we discussed the competition between the eutectic structure, and separate α- and β-crystallites during solidification. In addition to these locally ordered structures, we must now introduce another player in this game, which is the amorphous 'phase'. As expressed in terms of the temperature-growth-speed diagrams in Figure 3.6, we should expect to obtain a glassy structure in the alloy, if its 'growth speed' is even higher than the growth speeds of the other structures. For the amorphous phase, the growth speed is not a meaningful concept. Nevertheless, we can indicate the glass transition temperature (T_g) in the diagrams by a horizontal line, as the temperature below which the system is effectively frozen in, when it is successfully reached without nucleation or growth of either of the crystalline phases, i.e. either the α- and β-crystallites, or the eutectic structure. The diagrams show the maximum speeds for each of these that need to be overcome, for this condition to be satisfied. Together with the minimal size of the object that is to be quenched into the amorphous phase, this calls for a minimal cooling rate to achieve that phase safely. It is clear from the diagrams in Figure 3.6, that the situation is most favorable for the eutectic composition, in accordance with the argument already provided by Cohen and Turnbull. In the example of Figure 3.6, the relatively high growth temperature of β-crystallites at the indicated, off-eutectic composition would require a higher cooling rate for glass formation. Below this cooling rate, the alloy would solidify to either β-crystallites or eutectic phases.

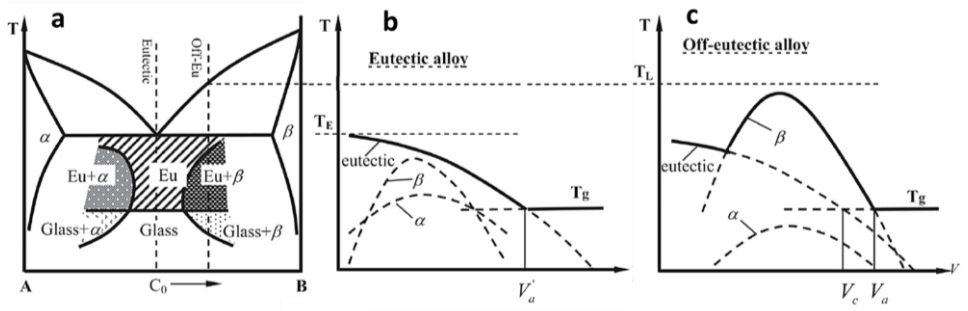

Figure 3.6 *(a) Phase diagram for a fictitious binary mixture of A and B with a symmetric coupled zone, displayed with various crystal growth regimes. (b) Relation between temperature and growth speed of various phases at the eutectic composition, (c) Similar to (b), for a B-rich, off-eutectic composition. Illustration adapted from ref. 138*

3.6 Metal-metal and metal-metalloid MGs

As we have discussed before, the only practical way to obtain a metal in a glassy configuration is for the metal to be an alloy of at least two elements. Metallic glasses are often divided into two groups, namely metal-metalloid glasses and metal-metal glasses. There are also other ways in which metallic glasses can be classified. Experiments show that metal-metalloid glasses are typically formed with atomic compositions of approximately 80% metal and 20% metalloid, such as Si, B, P and Ge. Both the metal and the metalloid components can consist of more than a single element. However, this ratio may apply differently to bulk metallic glasses, including those consisting of three elements and high entropy alloys. In the case of metal-metal glasses, there seems to be much less restriction on the composition, with the concentrations of individual components varying over large ranges, e.g. from 10% to 90%[141]. In practice, metal-metal glasses are usually more challenging to produce, and the number of successfully produced metal-metal glasses is therefore limited, especially for the binary systems and bulk metallic glasses.

The main structural difference between metal-metal and metal-metalloid metallic glasses is in the local atomic configurations. In most cases, metal-metal alloys locally adopt icosahedral structures, in order to optimize the packing density[142–146], whereas metal-semimetal alloys exhibit more complex network-like structures based on trigonal prisms[147].

3.7 Production of metallic glasses

As was mentioned before, the atoms in an MG can be frozen collectively, e.g. by rapidly cooling down a liquid metal alloy. But they can also be frozen in atom by atom. Here, we briefly describe three categories of production methods for metallic glasses: traditional quenching from the melt, solid-state transformation processes and deposition-based processes.

Quenching from the melt

Duwez and colleagues were the first who used the technique of rapid cooling of a liquid metallic alloy to obtain a metallic glass[148]. Their method was used also for the production of various other metallic glasses. Anantharaman and Suryanarayana reviewed the technique, as well as derived methods, elaborately[149]. Here, I summarize the main approaches.

Water quenching method

Water quenching is the rapid cooling of material in water and it is the simplest conventional quenching method. It has been in use for centuries to harden steel. In this method, the iron ore is cooled down from melt through its eutectic temperature in the phase diagram. In order to obtain a lower eutectic point, the material is alloyed with other elements. Lowering the eutectic point does not influence the kinetic barrier for phase transformation. Since this technique is more efficient for the system with a high surface area to volume ratio, the metallic glass to be obtained can only be in the form of a thin sheet or wire. The typical cooling rate, reached by this technique, is 10^2K/s, which is only useful in combination with materials with an extremely high glass-forming ability, much higher than typical metal alloys. Therefore, the water quenching method is irrelevant in practice for the production of metallic glasses.

Rapid solidification processing (RSP)

This is the traditional approach, in which a liquid is rapidly cooled below its freezing temperature. At a sufficiently high cooling rate – typically around 10^6 K/s or faster for a suitable metallic alloy – crystallization may be avoided and a metallic glass is obtained. This was the first technique by which a metallic glass was formed. In practice, there are several methods to reach such high cooling rates, involving the cooling of liquid droplets and liquid jets and rapid surface-melting-and-freezing processes. The most successful RSP method is the melt spinning technique which is frequently used in industrial applications. In this technique, the liquid alloy is poured on a rapidly spinning cold wheel, which deforms the stream of liquid into a thin ribbon that is cooled very efficiently to a temperature below T_g, due to its intimate contact with the wheel. The fast rotation of the wheel accelerates

the ribbon tangentially and makes it detach from the wheel at high speed so that it can be collected easily[149].

Solid-state processes

Annealing-induced solid-state amorphization and mechanical alloying are the most common solid-state processes that can lead to metallic glass.

Annealing-induced solid-state amorphization

Schwarz and Johnson reported that solid-state amorphization could be achieved by annealing-induced reactions of pure, polycrystalline metals[150]. To achieve metallic glasses by this technique, the metals that are to be alloyed should have a large negative heat of mixing and an enormously rapid diffusion of at least one element. The method is then to deposit a glass-forming thin film stack of the elements that are to be alloyed, typically by sputter deposition or thermal evaporation. Subsequently, this structure is annealed at a temperature that is still below T_g, but high enough for one of the elements to exhibit rapid diffusion[151]. The negative heat of mixing drives the formation of the alloy, which, once it is formed, is not only completely disordered, but also immobilized, since the temperature remains below T_g throughout the entire process.

Mechanical alloying

This solid-state, powder metallurgy technique is based on a controlled, brute-force approach, involving e.g. hot-pressing[152], cold welding or fracturing and re-welding of mixed powder particles. These particles are blended in a special grinder which is called high-energy ball mill[153]. This technique can be used for the production of various non-equilibrium phases.

Deposition-based processes

Building up a material atom by atom makes it possible to achieve the ultimate cooling rate, in which the excess energy that is introduced by every newly arriving atom is conducted away at maximum efficiency by the cold surface on which the atom lands. We distinguish a variety of atomic deposition methods, usually classified as either physical or chemical deposition.

Physical deposition techniques

Physical vapor deposition (PVD) stands for a collection of thin-film deposition processes in which a material is transported from a source, usually a solid or a liquid to a substrate on which it lands[154].

Sputter deposition; the metals to be deposited are introduced in a vacuum chamber as sputtering targets. Sputter deposition is a plasma-based deposition process where energetic ions, usually Ar^+, are formed that are accelerated by a potential difference towards the sputtering target. When they bombard the target, the ions remove atoms from the target surface. These liberated metal atoms can travel as atoms or ions via the plasma to the growth substrate, which is in the same vacuum system. There, they deposit in the form of a growing thin film. In order to obtain a metallic glass, we need to deposit at least two different elemental metals simultaneously. This can be achieved either by sputter deposition from a single target of premixed[108] metallic alloy or by sputter co-deposition from at least two separate, single-element targets[155].

Electron-beam deposition; in this method, an energetic electron beam is focused in a vacuum system on a metal target that locally heats up to a sufficiently high temperature to either sublime atoms from the solid phase or to melt and evaporate atoms. These then deposit on the nearby growth substrate[156,157]. In order to avoid preferential deposition of a single element, this method is usually not applied with premixed alloys. Deposition of an alloy requires co-deposition from separate sources.

Thermal evaporation; heating of materials in a vacuum system can also be achieved by direct heating methods, for example with the material contained in a crucible, from which it sublimes or evaporates towards the nearby growth substrate[158]. Again, alloys can be deposited in this way, by co-deposition of individual elements from separate sources. (Typical energy of atoms 0.1 eV)

Pulsed laser deposition; a high-power infrared laser is used to strike the material target with intense pulses that ablate the material in the form of nanometer-scale clusters that travel to the growth, substrate where they deposit. In this case, the atoms don't arrive one by one, but in groups that are large enough to minimize both the kinetic energy and the released cohesion energy per arriving atom in the cluster, but small enough to still rearrange into atomically thin deposits[159]. Like sputter deposition, this technique works well both for single-element targets and for premixed targets with the required alloy composition (cooling rate for picosecond pulses: $10^{13} Ks^{-1}$) [160].

Chemical vapor deposition (CVD)

In this class of methods, the growth substrate is exposed to a precursor gas, i.e. a flux of gas molecules. These molecules chemically decompose on the surface of the substrate and leave behind the material of interest, e.g. the metal atoms of choice, while the residues from these molecules desorb from the surface in this process[161]. There are various types of CVD and the most used ones for metallic glasses are plasma-enhanced CVD (PECVD), rapid thermal CVD (RTCVD) and combustion CVD (CCVD)[162].

3.8 Properties and applications of MGs

As a result of their non-periodic atomic structure and the absence of grains and grain boundaries, metallic glasses often exhibit special properties, such as a high electrical resistivity with a low-temperature coefficient, excellent soft-magnetic properties, superior mechanical properties, e.g. a high yield strength and, a high corrosion resistance. In this section, I will briefly discuss several of these properties.

Mechanical properties

Many of the mechanical properties of crystalline materials, such as most metals, are strongly dominated by crystal defects, such as their grain boundaries and dislocations. Usually, the yield strengths measured for metallic materials are well below the ideal strengths, predicted by theoretical calculations, because of these imperfections. They also make the mechanical properties inhomogeneous, which has significant consequences for the plastic deformation behavior of metals. By contrast, metallic glasses are homogeneous and lack grains, grain boundaries, dislocations and other extended crystal defects. As a result, these materials do not exhibit the variations in mechanical strength that are typical for regular metals, which makes them promising materials with high and constant yield strength. Despite this higher strength compared to their crystalline counterparts, the metallic glasses have elastic moduli in the same range as regular metals. Figure 3.7 demonstrates this in the form of a map with the yield stress, expressed as the elastic limit, and the Young`s modulus measured for various materials, including elemental metals as well as crystalline and amorphous metal alloys. The latter ones are indicated on the map as dark ellipses. What the figure reveals directly, is that the experimental values for the yield stress of the metallic glasses are much closer to the theoretical values than those for regular metals and crystalline metal alloys with the same Young's modulus (E). For a complete overview of these systems, we refer to the literature[99,163]. The high yield stress of metallic glasses makes them interesting materials for applications with special demands towards mechanical properties, such as elastic pressure gauges, flow-meters, sporting products, and micro-springs [164–168].

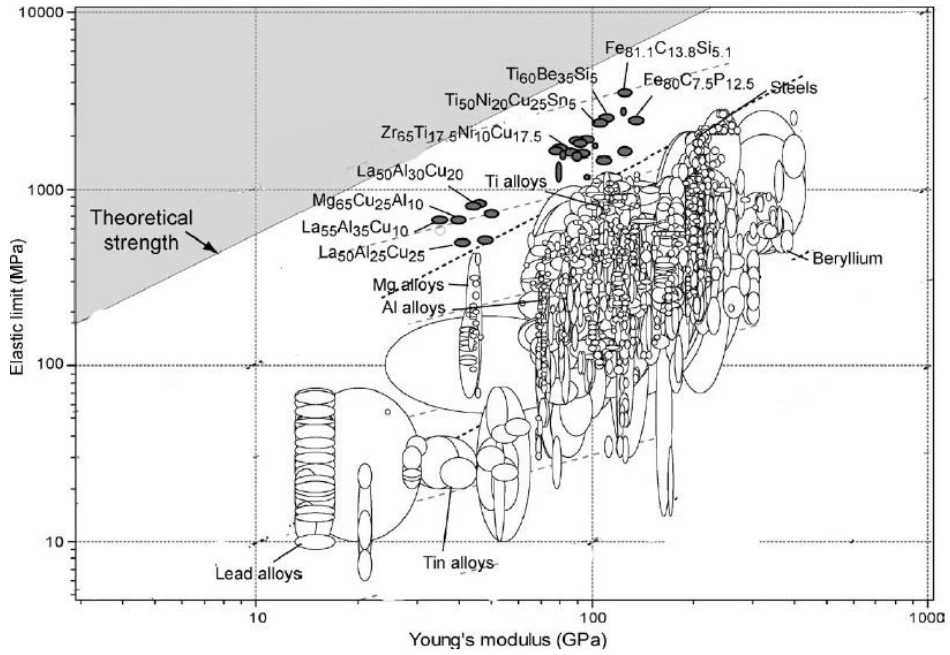

Figure 3.7 *Elastic limit (yield stress) and Young`s modulus for a wide selection of metals and metallic alloys, metallic glasses and nano-crystalline metallic glasses. Metallic glasses are indicated by dark ellipses. Figure adapted from ref.163.*

Electrical resistivity

The electrical resistivity values of metallic glasses are approximately two times higher than those for the crystalline versions of the same materials at room temperature and the difference becomes more pronounced at lower temperatures. Metallic glasses have higher resistivities, because the absence of long-range periodicity of the atomic-scale structure leads to increased scattering of conduction electrons. Another important difference is that metallic glasses exhibit extremely weak variations of their electrical resistance with temperature. Their resistance-temperature coefficient may even be zero or negative, enabling the suppression of thermal drift for electrical applications that require a stable resistance[169]. Figure 3.8 shows the relative resistivity as a function of temperature for both the crystalline and the amorphous forms of FePC. For the glass version of the material, the variation of the resistance is very modest up to 675K, which is the crystallization temperature for this material.

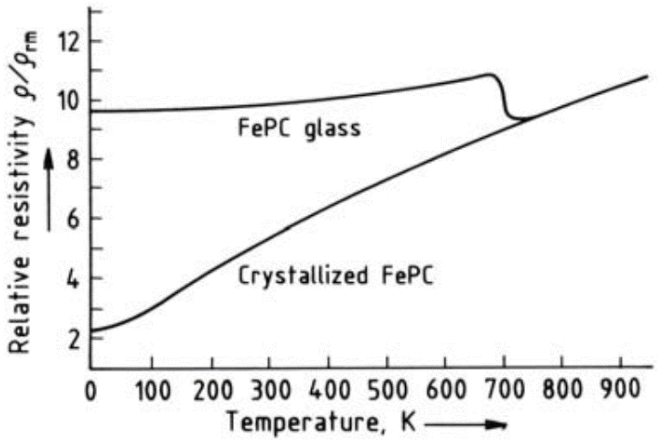

***Figure 3.8**. Relative electrical resistivity as a function of temperature for amorphous and crystalline FePC. The figure is taken from ref. 169,170.*

Magnetic properties

The random atomic arrangement of atoms and the absence of grain boundaries lead to easy magnetization and de-magnetization that provides magnetic metallic glasses with a high magnetic permeability and a high saturation induction. This is because the ferromagnetic magnetization vector is free from any structural anisotropy, which provides these materials with exceptionally soft magnetic properties. Soft magnetism corresponds to relatively short response times to changes in an external magnetic field, which means that these materials can be magnetized easily and that they have the tendency not to maintain their magnetization, once the external field is removed. By contrast, permanent magnets are made of materials having hard magnetic properties based on their internal crystal structure. Their structural anisotropy gives rise to hard de-magnetization. The soft magnetic materials also exhibit low magnetic losses (eddy current loss). These properties make MGs successful components for transformers, inductors, electromagnets and for microwave applications.

Corrosion resistance

Corrosion is one of the most common problems that almost all metals share. Polycrystalline and amorphous metals are potentially different in their chemical properties, including their corrosion behavior. Grain boundaries in a polycrystalline matrix are often the preferred channels for atoms and molecules from the surrounding phase, e.g. air or water, to enter the solid and migrate inside the material[163]. In addition, grain boundaries provide

the internal surfaces where corrosion can take place, in parallel with the corrosion on the external surface. By contrast, a glassy structure lacks grain boundaries and may therefore be expected to exhibit corrosion only at the outer surface and to protect itself in many cases from further corrosion by the presence of the first nanometers of surface oxide. In this way, we may hope that amorphous metals have a higher corrosion resistance than their polycrystalline counterparts.

Properties of thin-film metallic glasses

The structure and properties of thin films to some extent depend on the substrate temperature and the adatom mobility of the particles arriving in the film's deposition process. In addition to the properties that they share with BMGs, TFMGs may exhibit additional, unique properties. For example, due to the absence of grains or other microstructures, the surface roughness of metallic glasses is expected to be lower than that of their crystalline counterparts. Zeman et al. reported that the surface roughness of thin films of Zr-Cu metallic glass was less than 1.5 nm, which is lower than the roughness of equally thin polycrystalline films of elemental Zr and Cu[171]. Nevertheless, a surface roughness of 1.5 nm is a modest improvement and may also be achieved for polycrystalline thin films. Similar results were also reported for ZrCuAlNi metallic glass films[172] Kumar et al. demonstrated that the magnetic bulk metallic glasses would be promising candidates for high-density data storage due to the kinetics of the writing and erasing[173]. In fact, these properties reflect the surface smoothening of the disordered atomic structure triggered by annealing at supercooled liquid temperatures. The amorphous structure and the relatively low viscosity for the crystallization in the supercooled liquid region are responsible for the recovery of possible defects, such as scratches or the roughness originating from the deposition of the film. We recognize two main driving forces for this self-healing, namely surface tension and structural relaxation[174]. An AFM study of Fe-based thin-film metallic glass demonstrated that the depth of a nano indentation was reduced by 13.8% after annealing at 500˚C for 1 min[109], indicating that the glass film is not only smooth as a result of the deposition, but that the smoothness can be improved further by post-deposition annealing.

3.9 Limitations

Even though metallic glasses exhibit a high yield strength, their plastic properties present a limitation. As they do not have extended crystal defects, such as dislocations and stacking faults, MGs tend not to be very ductile. Instead, they show brittleness, caused by highly localized deformation in shear bands that accommodate the strain almost entirely, while leaving the rest of the material unstrained[175–182].

However, the poor-ductility problem of metallic glasses is strongly reduced for objects of smaller sizes, such as thin films[183]. It has been demonstrated that $Zr_{60}Cu_{24}Al_{11}Ni_5$ MG films with a thickness of 260 nm could accommodate a massive strain up to ~4000% without shear-banding or cracking[184]. Similarly, Glushko et al. reported an exceptional fracture resistance of 7-nm thick $Pd_{82}Si_{18}$, whereas this effect disappeared for thicker films[185]. The combination of a high mechanical strength due to the glassy structure with good ductility, connected to the nanometer thickness, makes thin-film metallic glasses promising candidates for applications such as microelectronics, data-storage electronics or nanoelectromechanical systems[186].

We can keep minimizing the effect of poor ductility and poor fracture resistance by keeping the sizes of metallic glass structures small, but the limited size in itself can be another limitation. Still, another solution may exist by which the limited-size restriction can be lifted, which involves the combination of nanocrystals inside an amorphous matrix. I will explain this suggestion in more detail in Section 11. First, we need to understand the crystallization of metallic glasses.

3.10 Crystallization from the glassy state

Independent of how it is produced, an amorphous configuration is thermodynamically unstable, or, more precisely, metastable. At a sufficiently high temperature, the transformation to a (poly)crystalline solid is bound to take place. Key steps in this process are the nucleation of crystallites within the glass environment and the subsequent growth of these crystalline nuclei[187,188]. In practice, crystallization of glass is observed at and above an onset crystallization temperature (T_x). Similar to T_g, which is a function of cooling rate, T_x is determined by the heating rate; it is higher for higher heating rates. The difference between T_x and T_g can be taken as a measure for the thermal stability of a glass;

$$\Delta T = T_x - T_g \quad (3.2)$$

Here, we briefly review classical nucleation theory to acquire a basic understanding of the first step in the crystallization process. We follow the well-known description for crystallization in a supercooled liquid and, for simplicity, assume the crystal nuclei to have spherical shapes, ignore possible effects of segregation and impurities at the amorphous-crystal interface and assume the crystallites to be homogenous in composition and structure[189–191].

Classical Nucleation Theory

Classical nucleation theory (CNT) provides a convenient model description of the kinetics of crystallization[192,193]. Here, we summarize the simplest form of CNT, assuming

crystallization to start with the spontaneous formation of a spherical crystalline nucleus inside a homogeneous liquid. The relevant quantity in this description is ΔG, the change in total Gibbs free energy ΔG when a crystalline nucleus with radius r is formed within the supercooled liquid. This change is composed of two contributions.

$$\Delta G(r) = \frac{4}{3}\pi r^3 \Delta g + 4\pi r^2 \sigma \quad (3.3)$$

The first term on the right relates to the volume of the spherical cluster, Δg is the difference per unit volume of the Gibbs free energy between the solid and the supercooled liquid phases, which is necessarily negative. The second term is introduced by the interface between the two phases, and is proportional to the Gibbs free energy per unit area σ of that interface, which is always positive. Since the first term scales with r^3 and the second with r^2, $\Delta G(r)$ displays a maximum at a special radius that we refer to as the critical radius.

$$\left.\frac{d\Delta G}{dr}\right|_{r=r_c} = 0 \quad (3.4)$$

Nuclei below this size tend to shrink and disappear. However, once a nucleus passes the critical radius, it is there to stay and it will grow without further hindrance. This makes the maximum of $\Delta G_c = \Delta G(r_c)$ the relevant free energy barrier for the nucleation process. We readily obtain r_c and ΔG_c from Eq. (3.4).

$$r_c = \frac{2\sigma}{|\Delta g|} \quad (3.5)$$

$$\Delta G_c = \frac{16}{3(\Delta g)^2}\pi\sigma^3 \quad (3.6)$$

This relation between the Gibbs free energy, the bulk free energy difference and the interfacial free energy is illustrated in Figure 3.9. Impurities in the liquid and the presence of surfaces may provide local nucleation sites, leading to heterogeneous nucleation, typically with a lower free energy barrier than ΔG_c.

A limited number of studies demonstrate that some metallic glasses with high thermal stability cannot be described well by CNT and seem to be described better by the phase-field theory (PFT)[194–197]. PFT uses an alternative solution to substitute the boundary conditions with a diffuse interface by an auxiliary field[198].

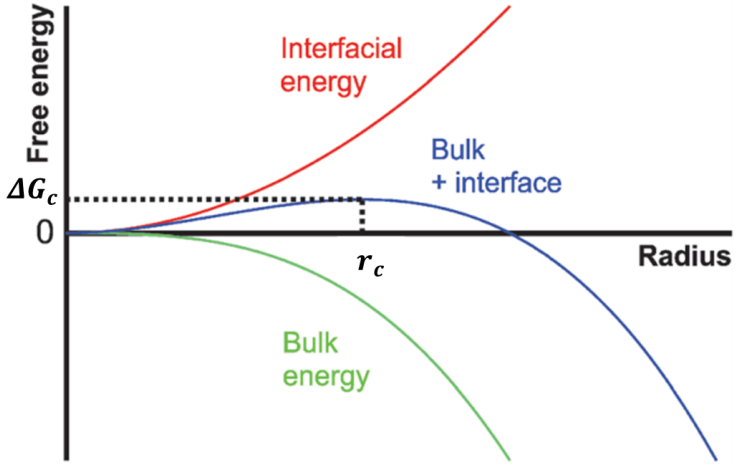

***Figure 3.9**: Schematic illustration of the free energy difference of a crystalline particle in a supercooled liquid, with respect to an equally large volume of liquid, as a function of its radius. The green curve shows the volume contribution, which is always negative, as the liquid is supercooled, and scales with the third power of the radius. The red curve illustrates the interfacial energy, which is always positive and scales with the square of the radius. The blue curve represents the total free energy (sum of volume and interface contributions), which initially increases with the radius, reaches a maximum at the so-called critical radius and reduces for larger radii. Figure reproduced from ref. 199.*

Crystallization Modes

Crystallization of bi-metallic glasses can take place in several ways, as illustrated in Figure 3.10. Each crystallization mode leads to a different structure, which provides the possibility to choose the microstructure of these materials and tune their properties[200]. Here, I mention the three main crystallization modes for bi-metallic glasses[201,202];

Polymorphous crystallization is the name that is used for transformations of the amorphous alloy that take place without changes in composition. The two panels of Figure 3.10 indicate different possibilities for such a transformation.

In the top panel, polymorphous crystallization would take place to a solid solution, in this case of A-crystallites with B-atoms dissolved in them. In the lower panel, polymorphous crystallization would take place to a well-defined, crystalline compound of A and B, which is indicated in the panel by a narrow free-energy curve.

Primary crystallization is the major way for a metallic glass to transform. It requires the segregation of the bi-metallic mixture into regions that are enriched in either of the

components, thus lowering the total free energy of the material. The double-tangent construction in the top panel of Figure 3.10 connects the Gibbs free-energy curve for A-enriched crystals with the curve for the amorphous (or liquid) mixture and demonstrates how the total free energy is lowered by the formation of A-enriched crystals. The other component, which is B-enriched and still amorphous, may undergo a subsequent crystallization transition, for example in the form of a second 'primary' crystallization transition, referred to as a secondary transformation, which would result in B-enriched crystallites.

Eutectic crystallization was already mentioned as the simultaneous, coupled crystallization into a spatially organized combination of two different structures with different compositions, ΔG was illustrated in Figure 3.6. In the lower panel of Figure 3.10, this is illustrated for the case of a solid solution of the A-rich crystalline phase in combination with a specific, crystalline A-B compound. In Figure 3.6, it was shown for the combination of two solid solutions, A-rich and B-rich.

Crystallization of an amorphous structure into metastable or stable phases goes hand in hand with changes in physical properties, such as mechanical, electrical and magnetic[203–205]. Ketkaew et al. investigated the effect of crystallization on fracture resistance. They found that a minor level of crystallization, up to 6%, does not lead to a significant difference in toughness. However, they measured a 50% decrease in the fracture resistance after an additional 1% crystallization[206].

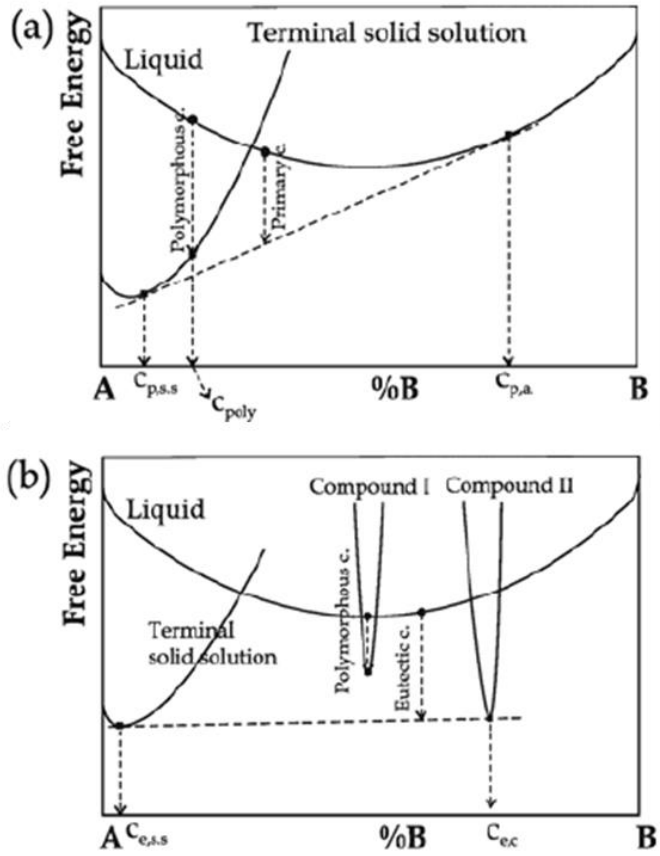

Figure 3.10 *Gibbs free energy diagrams for a binary metal alloy that illustrate the crystallization modes, discussed in the text. The free-energy curve for the liquid is taken as representative for that of the amorphous metallic mixture. Whereas polymorphic crystallization requires no changes in composition, segregation of the mixture into A-enriched and B-enriched regions is necessary for primary crystallization and eutectic crystallization. Figure reproduced from ref.182.*

3.11 Amorphous and nano-crystalline metallic glasses

Nanocrystals are aggregates of atoms in the form of single crystals with sizes smaller than 50 nm. They form fine, polycrystalline structures with a high density of grain boundaries. Nanocrystalline solids are often considered an intermediate between amorphous and conventional polycrystalline materials with coarser grains. Previously, we discussed the

unique properties of amorphous metallic glasses and their drawbacks, such as poor fracture resistance. Here, we will briefly explore the characteristics of nanocrystalline materials, after which we consider one composite that consists of an amorphous metallic matrix with embedded nanocrystals.

There are various methods to produce nanocrystalline materials. The first to consider is ball milling. In section 3.7, we mentioned that this method can be used for the production of metallic glasses[207,208], but they also showed that this method can also be used to obtain one composite consisting of both amorphous and nanocrystals by modifying the composition of the elements. A second method is the annealing-induced crystallization of amorphous alloys[209]. Following the discovery of metallic glasses, researchers often investigated their thermal stability. It was found that for some material compositions of specific alloys, such as Fe-P-C[210], Zr-Cu[211], and Pd-Si[96,212], after the annealing at a specific temperature that depends on the material and the precise composition, a combination is obtained of nanocrystals embedded in a metallic glasses. Unfortunately, it is challenging to control the amount of crystallization with this technique. In addition, the thermal treatment itself also can cause other changes that dramatically affect the properties of the metallic glass. For example, annealing at temperatures below the crystallization temperature has a strong effect on the micro-hardness of an amorphous Fe-B alloy[213]. Therefore, more controlled methods are increasingly gaining attention, such as PVD methods, e.g. thermal evaporation[214], pulsed laser deposition[215,216] and sputter deposition[217–220]. These methods enable one to directly obtain nanocrystalline thin films. Especially, sputter deposition has an overall advantage over other techniques because it provides an enhanced GFA over a wider compositional range for the alloys to be produced in amorphous or crystalline configurations by modifying the sputtering settings, [220,221] and furthermore it is an attractive technique for industrial applications. Chapter 2 of the thesis presents the experimental results of nanocrystalline elemental metal thin films by sputter deposition. The most important property, of determining whether the deposition results in nanostructured metallic glass, is the composition of the sputtered elements.

In addition to these, other methods have been developed to obtain nanocrystalline structures on a surface, such as crystallization by ultrasonic shot peening[222] and surface mechanical attrition treatment[223]. For these methods, the amorphous matrix is the parent phase for crystallites that are formed in a later stage. Li et al. wrote a useful review article on the fabrication, properties and applications of amorphous-nanocrystalline alloys[224]. They highlighted the advantages of these alloys compared to regular crystalline counterparts including high strength and hardness. However, some limitations are also demonstrated such as modest stability at elevated temperatures[225,226] and poor ductility[227–229], similar to the limitations of metallic glasses, discussed previously.

Smart engineering may enable the combination of the advantages of nanocrystalline materials and amorphous metallic glasses. In order to improve fracture resistance, one can introduce crystallites into an amorphous matrix. Embedding micrometer-size crystallites in metallic glass can improve ductility but this also introduces a remarkable drop in the overall strength of the material[230]. The behavior is entirely different when the crystallites have sizes in the nanometer regime. Kim et al. demonstrated that including nanometer-size Al crystals in an Al-Y-Ni-Fe metallic glass not only increases the fracture resistance but also slightly increases the strength[231]. Early research aiming to increase the mechanical strength of metallic glasses was mostly conducted at Tohoku University. It was found that most of the metallic glasses exhibit an improved hardness and an increased elastic modulus when the volume fraction of nano-crystallites is increased from 10% to 40% [224,232–240]. The role of nanocrystals inside the amorphous matrix enhances not only the mechanical properties but also the chemical properties of the material such as resistance to oxidation[241]. Therefore partially crystallized metallic glasses can find a place in various applications. Even though it is clear that the detailed atomic configurations are at play here, in combination with thermodynamic driving forces, the precise mechanisms by which these properties are improved are not fully understood. The methods, discussed here, to obtain both crystallites and an amorphous matrix, mostly rely on the formation of the crystallites in a pre-existing amorphous medium, by subsequent thermal or mechanic processes. However, these final-stage treatments may significantly affect the properties of the two components of the composite material. It would be interesting to produce such a hybrid material of a binary alloy, combining crystallites and an amorphous matrix, without the need for special thermal or mechanical treatments. Preliminary observations in the context of Chapter 4, suggest that we may have a recipe to directly obtain configurations of nano-crystallites in an amorphous matrix via the deposition of thin binary alloy films.

3.12 Ru-Mo alloy

In this thesis, the focus is on alloys of Ru and Mo. Obviously, these alloys do not satisfy the first empirical rule that was introduced in Sect. 3.4 for achieving a high GFA, namely that the alloy should contain at least three elements. Also, the second rule, that the atomic sizes should differ by at least 12%, does not apply, as the Van der Waals radii of Mo and Ru, of 209 pm and 205 pm respectively, differ by less than 2 %. For this reason, RuMo alloys have received little attention as potential metallic glasses. However, since both materials exhibit favorable properties for applications that involve EUV light, it is useful to explore the possibilities for amorphous structures of these alloys and their potential benefits for these applications.

The binary RuMo phase diagram was investigated at temperatures below 1600˚C by Raub[242]. It was found that only small quantities of Ru can dissolve into Mo, whereas Mo can dissolve up to 35% into Ru at 800˚C. In addition to this, a special crystal structure was identified by Bloom[243] for the composition Ru_3Mo_5, referred to as the sigma phase (σ-phase). The sigma phase is a member of a family of topologically close-packed (TCP) phases, also known as Frank-Kasper (FK) phases. It consists of intermetallic compounds of transition metals with a non-stoichiometric structure. The sigma phase has a complex tetragonal structure with 30 atoms in a unit cell. This is a special case for the transition metal alloys, having the ratio of valence electrons to atoms in the range of 6.2 to 7.4[244], and the formation of this phase has a strong influence on mechanical properties, such as hardness and brittleness. Anderson and Hume-Rothery studied the Mo-Ru system at temperatures above 1600˚C and they claimed that the maximum solubility of Mo is 51% in Ru, where Ru dissolves up to 30.5% of Mo at the same temperature[245]. Kleykamp reinvestigated the phase diagram of RuMo with a broader temperature range between 900 and 2000˚C and obtained consistent results with the previous studies[246]. Furthermore, Kleykamp demonstrated that the σ-phase of Ru_3Mo_5 ceases to exist at temperatures below 1143˚C, see Figure 3.12. This implies that the formation enthalpy is unfavorable for the sigma phase, but the structure is stabilized by configurational entropy for temperatures above 1143˚C.

In 1977, Collver and Hammond investigated the stability of amorphous transition-metal alloy films, including MoRu alloys, grown by electron-beam evaporation onto a liquid-helium cooled substrate[247]. Their research identified an abrupt decrease in electrical resistivity during annealing, which was correlated to crystallization. The results suggested that Ru-rich alloys, down to 75% of Ru, are crystalline immediately when deposited. For 75% of Ru, 25 K was found as the transformation temperature, indicating the alloy to be amorphous below that temperature. For alloys containing 50% and 68% of Ru, no sharp drop was found in the resistivity up to 800 K, suggesting that these compositions were amorphous. However, Collver and Hammond did not provide any direct proof of the microstructure in their paper.

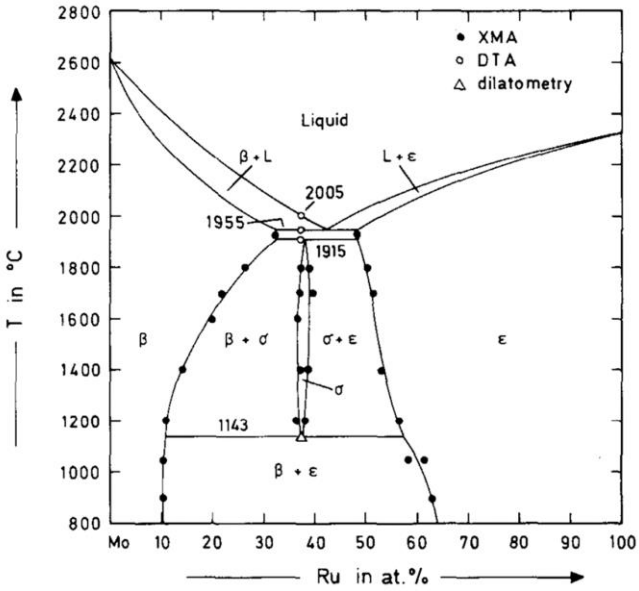

Figure 3.12 *Binary Phase diagram of Mo and Ru for temperatures above 800˚C. The diagram combines results from X-ray microanalysis (XMA), differential thermal analysis (DTA) and dilatometry. In the immiscibility gap, at temperatures above 1143˚C, the so-called σ-phase is found. The other phases that are relevant in the immiscibility gap are the Mo-rich β-phase and the Ru-rich ε-phase*. Figure reproduced from Ref. [246].

In Chapter 4, I report results for alloys of Ru and Mo, obtained by sputter co-deposition. There are multiple reasons that make an amorphous Ru and Mo alloy very attractive and promising. First of all, both Ru and Mo show a high IR-emissivity[248]. In addition, Ru exhibits superior resistance to oxidation[249], while Mo has a very high EUV transmissivity[250]. That is why both metals are well-researched and in use in the semiconductor equipment industry. Furthermore, Collver and Hammond reported some amorphous transition metals, including Ru and Mo alloy, that exhibit superior superconductivity, compared to their crystalline counterparts[247]. Ru and Mo are also essential and very high-yield elements in irradiated oxide nuclear fuels[251].

Chapter 4

AMORPHOUS ALLOY FILMS OF RUTHENIUM AND MOLYBDENUM

Microscopy and diffraction measurements are presented of ultrathin binary alloy films of ruthenium and molybdenum that are obtained by standard sputter deposition. For compositions close to $Ru_{50}Mo_{50}$, we find the films to be amorphous. The amorphicity of the films is accompanied by a significant reduction of the roughness with respect to the roughness of equally thick films of either ruthenium or molybdenum. We ascribe this to the absence of the grain structure that is characteristic of the polycrystalline films of the separate elements.

4.1 Introduction

Thin metal films find broad application in advanced as well as every-day technology as a relatively cost-effective way to customize and improve materials properties, for example to protect against corrosion [219], to lower friction and enhance wear resistance[9,252–254], as electrically conductive layers[6,8], or, simply, to make a material look metallic. The combination of a cheap inside with a thin film of a more sophisticated or expensive material often forms a cost-effective way to add the superior surface properties or looks of the coating to the bulk properties of the inner material. On a microscopic scale, metal films are usually polycrystalline. The strong tendency for metals to crystallize, usually makes these films organize themselves as a conglomerate of small crystallites, all with different orientations. Even though most of the atoms in the film can be inside such small crystalline grains, many macroscopic film properties are actually dominated by the grain boundaries between them, where the perfect crystalline stacking is obviously compromised, and by other defects in the crystal structure. For example, the yield strengths measured for polycrystalline films differ strongly from the ideal strengths, predicted by theoretical calculations for perfect single crystals[163], because of the strong effects of dislocations and other crystal defects on the mechanical properties[255]. Chemically, the protective quality of a polycrystalline film can be significantly below that of a single-crystalline one, if atoms or molecules can migrate through the polycrystalline ensemble via the grain boundaries[163]. Even the chemical integrity of the film itself can be at stake, when e.g. oxidation can take place not only at the surface of the film, but also deeply inside, at or via the grain boundaries. In many modern applications, such as low-friction films and optical coatings, extreme, i.e. atomic-scale flatness of thin films would be of advantage[256,257], but the grainy structure of a polycrystalline film also comes with roughness, simply because of the tendency for each grain at the surface of the film to adopt its own equilibrium shape[22]. Rather than connecting into a densely packed, atomically smooth layer, these randomly oriented crystallites typically make the surface look like a cobblestone pavement.

Conceptually, one may recognize two obvious, but extreme solutions to the problems introduced by the polycrystallinity of most metal films: either perfect order, i.e. single crystallinity, or total disorder, i.e. amorphicity. In principle, one should be able to avoid grain boundaries altogether by producing thin, metal films in the form of perfect, single crystals. Unfortunately, even though it is possible to reach lateral grain sizes that can be significantly larger than the thickness of a metal film, it is practically impossible to make the average grain size arbitrarily large and thus completely remove the grain boundaries from thin, crystalline metal films. Moreover, larger grain diameters are accompanied by larger thickness variations of the film – the cobblestone effect. For cases where the lateral grain size would be much larger than the film thickness, this would eventually even lead to

places where the film thickness is reduced to zero, at which point the film would be free to break up and expose the underlying material, depending on the surface and interface free energies of the materials involved. The counterintuitive, extreme alternative would be to avoid grain boundaries by going completely in the opposite direction and avoiding crystallinity altogether. For this purpose, the metal would need to be deposited and maintained in a glassy arrangement. This is practically impossible to achieve and maintain for single-element metals.

Interestingly, several metallic alloys are known that can be cast or deposited in an amorphous form. First reports on amorphous metal alloys date back to the early nineteen-sixties[101,148]. The rationale behind this approach is that crystallization often requires a significant rearrangement of the internal configuration of the alloy. This can, for example, take the form of segregation of the compound into two different compositions, one enriched in one of the two metals, the other enriched in the other, with at least one of them forming crystallites. This would require the migration of atoms over substantially larger distances than the atomic-scale rearrangements required to turn a single-element material into a crystal. Additional kinetic hindrance is introduced when the two constituents have significantly different atomic sizes [121,258]. While a single-element metallic liquid typically would have to be cooled at a rate in the order of 10^{14} K/s[91] to reach the glass transition temperature without spontaneous nucleation of crystallites, typical cooling rates required for glass formation of selected binary metal alloys can be lower by more than 11 orders of magnitude[259]. This still calls for dedicated production methods. Since the early work on metallic glasses, a growing variety of new, ever more complex, metallic materials was identified that can be obtained in the form of a glass. One class of examples is formed by high-entropy alloys[260], for which the combination of five or more elements makes that the high configurational entropy of the liquid strongly reduces the melting point and thus reduces the remaining temperature difference that needs to be overcome rapidly to reach the glass transition.

In this chapter, we concentrate on the classic case of a binary mixture, by investigating alloys of ruthenium and molybdenum. These materials were selected because of their application in reflective optics for lithography with extreme ultraviolet light with a wavelength of 13.5 nm, used in the latest generation of lithography tools in the semiconductor industry[261]. We first demonstrate that sputter deposition of mixtures of these metals with a composition close to $Ru_{50}Mo_{50}$ leads to amorphous thin films with a surprising level of metastability with respect to crystallization. We employ grazing-incidence x-ray diffraction and high-resolution transmission electron microscopy to inspect the amorphicity of these films down to the atomic scale. We further show that these films exhibit an extremely smooth surface when compared to the conventional, polycrystalline surfaces that we

obtained by the same sputter deposition procedure for similarly thick layers of the elemental constituents, i.e. Ru or Mo, under the same conditions and on the same substrates.

Thin amorphous films have been demonstrated before for selected binary metal alloys[109], for example in the case of the Cu-Zr system[171]. For the Ru-Mo alloy that is featured in the present chapter, to our knowledge, no direct observations are available for the amorphicity of thin films, albeit measurements in[59] on the electrical resistivity of electron-beam deposited RuMo films were interpreted already in 1978 as an indication for their amorphous structure in a certain range of compositions.

That the surface roughness of thin amorphous metal alloy films can be very low[109,262] and that it increases upon the change from amorphous to polycrystalline, has been found before, for example in annealing experiments[263] on ZrAlMoCu metallic glass films and in the comparison of polycrystalline Zr and Cu films and amorphous CuZr alloy films[171]. Similar indications were reported for ZrCuAlNi metallic glass films[172]. For the CuZr-case, the larger roughness of the polycrystalline films was ascribed to their columnar structure[171].

We investigated mixtures of ruthenium and molybdenum. A special feature of the binary phase diagram of RuMo mixtures is the existence of an entropy-stabilized configuration for a narrow range of compositions around Ru_3Mo_5, the so-called σ-phase[243–246], a tetragonal lattice (space group $P4_2/mnm$) with five inequivalent sublattices of atomic sites. This phase occurs at temperatures below the eutectic point, i.e. the lowest melting point for any of the mixtures. Rather than to cool the mixture from the melt, we concentrated on ultrathin films that we routinely deposit on Si(100) wafers, terminated by a native oxide layer, by simultaneous sputter deposition of Ru and Mo from separate sources. In contrast to Ru-Mo growth studies reported in the literature[59,60], the substrate was kept at room temperature. For practical reasons, we used DC-sputtering for Ru and RF-sputtering for Mo, but we do not expect that this difference plays a decisive role in our findings. In this way, films were obtained with thicknesses ranging from 4 to 30 nm and compositions ranging from $Ru_{83}Mo_{17}$ to $Ru_{35}Mo_{65}$. Details about the deposition procedure and all other experimental methods can be found in Chapter 1. The thicknesses and precise average compositions of the films were determined after deposition with a combination of techniques, including profilometry, atomic force microscopy, electron microscopy, energy-dispersive x-ray spectroscopy and x-ray photoelectron spectroscopy. For reference, we also deposited pure Ru films and pure Mo films. In order to bring out their atomic-scale structure, local composition and surface smoothness, we inspected the collection of deposited thin films with further techniques, including grazing-incidence x-ray diffraction (GIXRD), scanning electron microscopy (SEM), high-resolution cross-sectional transmission electron microscopy (TEM) and atomic force microscopy (AFM).

4.2 Results

Figure 4.1 concentrates on the structural characteristics of approximately 21 nm thick RuMo alloy films with two different compositions. The $Ru_{43}Mo_{57}$ film is closest to the eutectic composition of $Ru_{42}Mo_{58}$[245,246,264]. A strong fingerprint of the amorphous nature of this film is provided by the upper GIXRD pattern in Figure. 4.1a. It contains two very broad peaks, similar to the diffraction pattern from a liquid[265,266]. The complete absence of sharp peaks indicates that if some of the Ru and/or Mo atoms would still have formed crystals, their fraction of the total cannot establish more than approximately 1% of the total number of atoms, based on the sensitivity and the noise level in the data. Note that the sharp peaks, labeled by an asterisk, stem from the Si(100) substrate and have low intensities due to the grazing-incidence geometry of the experiment that was chosen to maximize the signal from the film. The sharpness of these Si peaks testifies to the angular resolution of the diffraction measurement. In order to be certain that the broad GIXRD peaks of the alloy correspond to an amorphous configuration, rather than a nano-crystalline arrangement, for which the small crystallite size might perhaps lead to similarly broad peaks, we inspected the $Ru_{43}Mo_{57}$ film also with high-resolution cross-sectional TEM. The result is shown in Figure. 4.1b. While the Si(100) substrate exhibits its familiar, well-ordered lattice structure, the alloy film is completely disordered on all length scales, down to atomic dimensions, as can be verified directly in the enlarged section in Figure. 4.1c. The spatial information in the TEM image is consistent with the GIXRD spectrum, as can be recognized from the two-dimensional fast Fourier transform (2D FFT) in Figure 4.1d that was taken from the TEM region in Figure. 4.1c, completely within the alloy film. As expected from the qualitative impression of the TEM image itself, the 2D FFT contains no orientational preferences. The broad ring reflects the short-range correlation between the atoms in the amorphous film and their direct neighbors, and its radius coincides with the position of the main peak in the GIXRD pattern. Interestingly, the surface of the film makes a smoother impression in the TEM image than the surface of the thin native oxide layer on which the film was deposited. We will return to this point later.

The lower curve in Figure 4.1a shows the GIXRD spectrum measured for an equally thin film of the more ruthenium-rich alloy, $Ru_{77}Mo_{23}$. It is dramatically different from the diffraction pattern from the amorphous alloy, $Ru_{43}Mo_{57}$, and shows a rich collection of sharp peaks that can all be associated with a polycrystalline layer with the hexagonal close-packed structure of ruthenium. Interestingly, the peak positions correspond to lattice constants of a = 0.272 nm and c = 0.432 nm, which indicates an expansion of the volume of the lattice unit cell by 2.0 % ± 0.35 % with respect to the regular lattice of ruthenium. This indicates that these diffraction peaks do not come from pure ruthenium, but from a solid solution of the somewhat larger molybdenum atoms in ruthenium[246]. The lattice

expansion can be associated with a composition of $Ru_{84}Mo_{16}$, with an error margin of no more than ± 3 % on the two atomic concentrations. The widths of the diffraction peaks exceed the resolution and can be used to estimate an average grain size of approximately 10 nm, a significant fraction of the film thickness. We speculate that the ruthenium-rich crystals that the GIXRD spectrum is indicative of are formed out of the deposited, 77:23-mixture by segregation. The remaining material in the film must then be enriched in molybdenum. One might expect this remaining component to form body-centered cubic crystallites, i.e. with the lattice structure of molybdenum (and with a slightly reduced lattice constant due to the dissolved ruthenium). However, the GIXRD pattern does not contain any additional peaks. This means that the molybdenum-enriched component must be present in a different form, which does not generate distinct, i.e. sharp features in the GIXRD. In order to further elucidate the segregated structure for this composition, additional experiments will be required.

The diffraction pattern and TEM observations of the amorphous nature of the $Ru_{43}Mo_{57}$ film were characteristic for the entire film, rather than specially selected 'best cases'. Figure 4.2a shows the same combination of a selected region from a cross-sectional high-resolution TEM micrograph of the $Ru_{43}Mo_{57}$ alloy film and its two-dimensional fast Fourier transform that was shown already in Figs. 4.1c,d. For completeness, we also show Figs. 4.2b and c of two other, equally large regions from the same film and the corresponding 2D-FFT patterns. The arrows point to what one might interpret as weak indications of local order, but that does not stand out as ordered domains in the corresponding real-space images. Apart from such occasional local intensities, all two-dimensional Fourier transforms were fully consistent with the smooth pattern for Figure 4.2a.

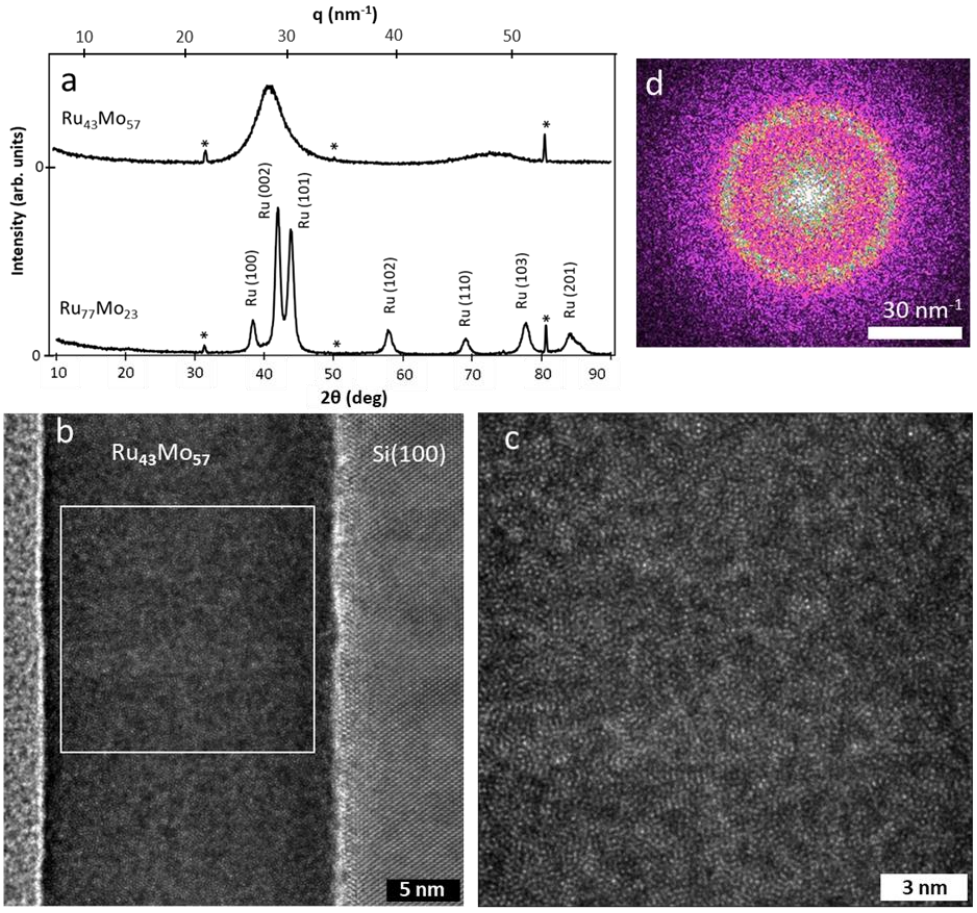

Figure 4.1. *(a) GI-XRD measurements from 21 nm thick $Ru_{43}Mo_{57}$ (top) and $Ru_{77}Mo_{23}$ (bottom) alloy films. Along the upper horizontal axis of the panel, the scattering angles are converted into the corresponding reciprocal-space scale. The sharp peaks indicated by asterisks are artifacts originating from the Si(100) substrate. (b) Cross-sectional high-resolution TEM micrograph of the $Ru_{43}Mo_{57}$ alloy film and the Si(100) substrate. Note the crystalline structure of the Si substrate, the structural disorder of the thin native oxide layer by which the substrate is terminated and the complete absence of crystalline order in the metal alloy film on top of that. The white rectangle indicates the region that is displayed on a magnified scale in panel (c) to emphasize the disordered arrangement in the alloy. Panel (d) represents the two-dimensional fast Fourier transform of this region, which matches the features in the upper GIXRD curve of panel (a), measured from the same composition*

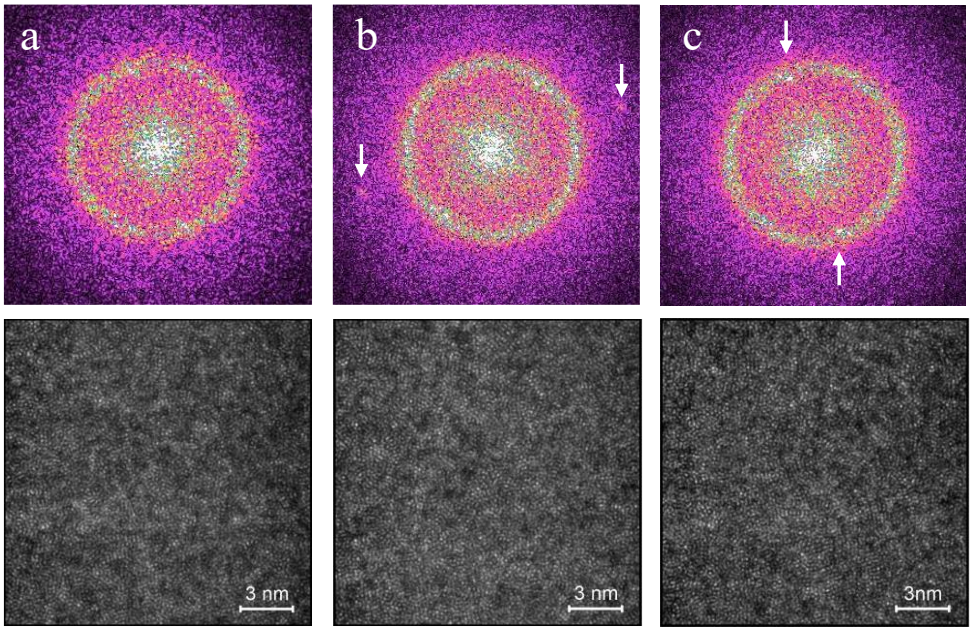

Figure. 4.2. *Three selected regions from cross-sectional high-resolution TEM micrographs of the $Ru_{43}Mo_{57}$ alloy film, each taken completely within the alloy film. The corresponding two-dimensional fast Fourier transforms all display the same broad ring, typical for an amorphous arrangement. The arrows in panels (b) and (c) indicate weak, additional signatures of local order that we have observed in some of these local 2D FFTs, but that we cannot recognize readily in the corresponding TEM images*

Figure 4.3 shows the XPS spectra of a polycrystalline $Ru_{77}Mo_{23}$ thin film (top) and an amorphous $Ru_{43}Mo_{57}$ thin film (bottom). The survey spectra (left) have been acquired at 500 eV pass energy, while the detailed Ru 3d and Mo 3d regions (right) have been acquired at 300 eV pass energy. The survey spectra only contain peaks associated with ruthenium, molybdenum and oxygen.

The detailed Ru 3d and Mo 3d regions have been fitted using Voigt functions, taking into account the presence of metal oxides and the broadening due to the Coster-Kronig effect. A Shirley function has been used for background correction.

The surface fractions of ruthenium and molybdenum were inferred from the total areas of the Ru 3d and Mo 3d peaks, obtained from the fits and the corresponding photoionization cross sections, according to the general equation:

$$x_i = \frac{\frac{A_i}{\sigma_i}}{\sum_{j=1}^{N}\left(\frac{A_j}{\sigma_j}\right)} \quad (4.1)$$

where *A* is the area of a peak, *σ* is the corresponding photoionization cross-section, *i* and *j* refer to the elements ruthenium and molybdenum, and *N* stands for the total number of elements, in this case 2. The surface compositions that we obtained in this way for the two alloys in Figure 4.3, are given in the two panels on the left, with the overview spectra. Within the error margins, the measured surface compositions of $Ru_{79}Mo_{21}$ and $Ru_{43}Mo_{57}$, are equal to the (average) bulk compositions of $Ru_{77}Mo_{23}$ and $Ru_{43}Mo_{57}$ that we obtained from SEM-EDX measurements on the same samples (see Table 1.3).

The oxygen peaks are expected due to the exposure of the surface to air after the deposition, leading to surface oxidation and water adsorption. The XPS spectra contain a minor molybdenum peak at 235 eV, stemming from molybdenum oxide. Note that the surface of the $Ru_{43}Mo_{57}$ alloy contains more oxygen than that of the $Ru_{77}Mo_{23}$ alloy, which may be attributed to the stronger oxidation resistance of ruthenium capping layers[267,268].

A possible C 1s peak, due to carbon contamination during deposition, would be located around 284.5 eV and would thus overlap with the Ru 3d peak structure. When fitting the Ru 3d peak, we arrive at the correct 3:2 peak ratio, from which we conclude that carbon contamination can be neglected.

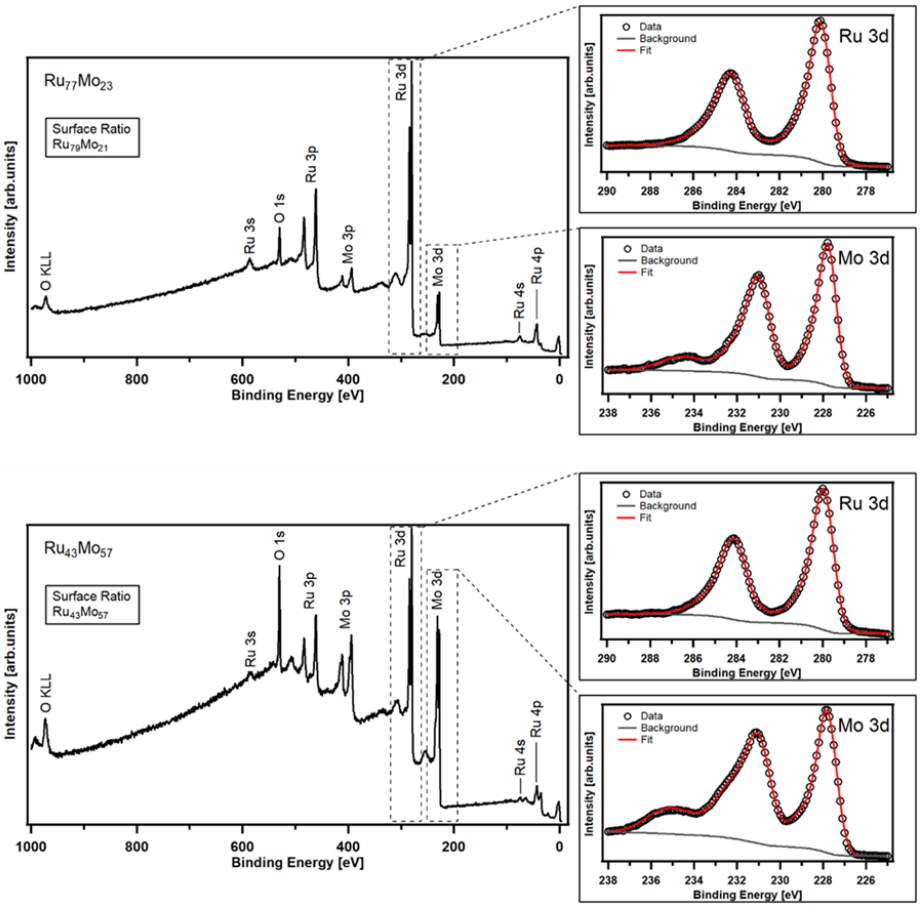

Figure. 4.3. *XPS spectra for a 20 nm thick, polycrystalline film with a composition of $Ru_{77}Mo_{23}$ (top) and for a 21 nm thick, amorphous film with a composition of $Ru_{43}Mo_{57}$ (bottom). The panels on the right show the detailed spectra for the two thin films around the Ru 3d and the Mo 3d regions, and the corresponding fits (red curves).*

The bottom right panel of Figure 4.4 repeats the TEM image of Figure 4.1b. The other panels show the simultaneously acquired EDX maps for four elements, ruthenium, molybdenum, silicon and oxygen. As the ruthenium and molybdenum maps clearly show and as is quantified in the concentration curves for the two metallic elements in the bottom left panel, the concentrations of the two metals go through a total of close to five full cycles of approximately 15% variation, with the two metals varying in antiphase with each other. This variation is a direct consequence of the source geometry of our sputter deposition chamber in combination with the continuous sample rotation during deposition. As explained in Chapter 1, we produce our alloy films by co-deposition from separate, pure

molybdenum and pure ruthenium targets. These sputter targets are arranged off-axis with respect to the rotation axis of the sample platform, each directed toward the center of the platform. This platform carries multiple samples, with each sample placed at a certain distance from the rotation axis. During the deposition, the sample platform rotated at a speed of 4 revolutions per minute (RPM), periodically bringing each sample closer to the molybdenum target and further away from the ruthenium target and vice versa. The period of the observed concentration variations matches this rotation. Interestingly, this variation implies that the results in Figure 4.4 and the rest of this chapter are all for alloy films that internally contain a range of compositions. The entire, 21 nm thick film of Figure 4.4 can be seen to be amorphous, as is also confirmed by the GIXRD measurements, even though the composition within the film varies between $Ru_{35}Mo_{65}$ and $Ru_{50}Mo_{50}$. This shows that the alloy is amorphous over at least this range of compositions.

SEM images show a fully structureless surface on the $Ru_{43}Mo_{57}$ films, in full contrast with the familiar network of grains and grain boundaries that we observe in SEM images on thin films of pure ruthenium or pure molybdenum. In fact, focusing the electron microscope on these alloy films was only possible by virtue of special features, such as the edges of the films, as the surfaces of the films did not offer any discernable contrast. In order to obtain more quantitative information on the height variations, we inspected the surfaces of the films with AFM. The upper left panel of Figure 4.5 shows a large-area scan of a 30 nm thick $Ru_{43}Mo_{57}$ film. In spite of the large scan range, all height variations are fully captured by the tight $\pm$ 0.7 nm height range of the color bar. The enlarged region shown in the upper right panel of Figure 4.5 indicates that there are mild undulations in the height, with a typical lateral length scale in the order of 10 nm. The surface roughness of the alloy, that can be derived from these images as the root-mean-square (RMS) height variation around the average surface plane, is spectacularly low, 0.26 nm. Within the error margins, the alloy film seems not to introduce any additional roughness with respect to the roughness of the native oxide on the Si(100) substrate, on which the metal films were deposited.

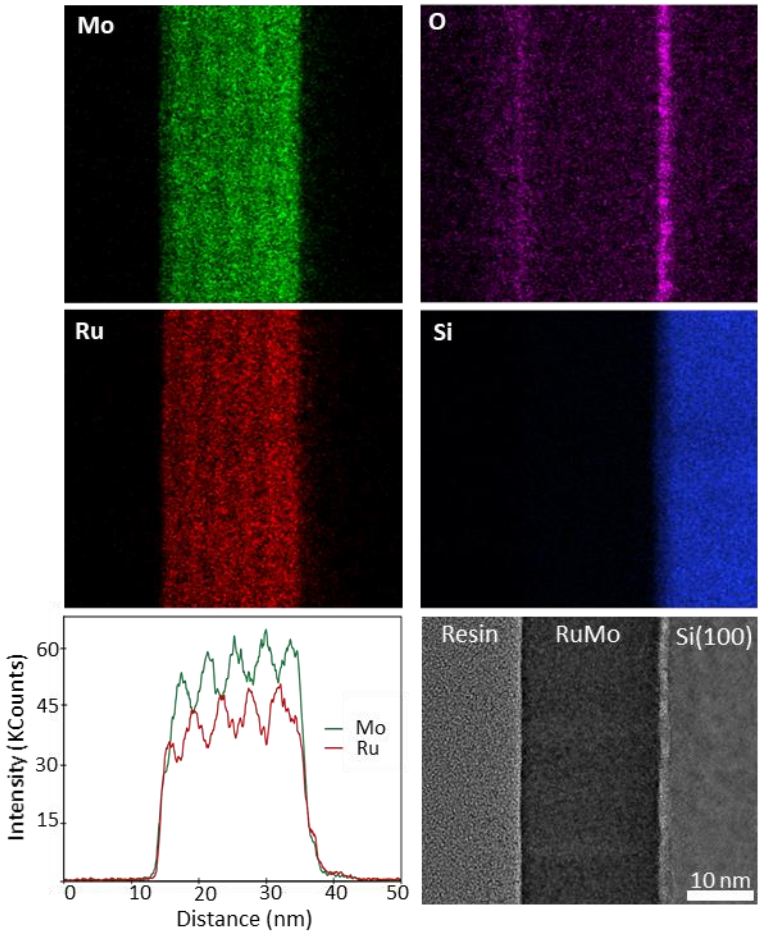

Figure. 4.4 *HAADF-STEM image (bottom right panel) and simultaneously measured EDX maps on a 21 nm thick film of the $Ru_{43}Mo_{57}$ alloy (top four panels) for four elements: Ru (red), Mo (green), Si (blue) and O (purple). The corresponding concentration curves for Ru and Mo (bottom left panel) demonstrate a periodic 15% variation in the composition, with the Mo and Ru concentrations changing in antiphase with one another. This variation can also be recognized directly as the striations in the EDX panels of Mo and Ru.*

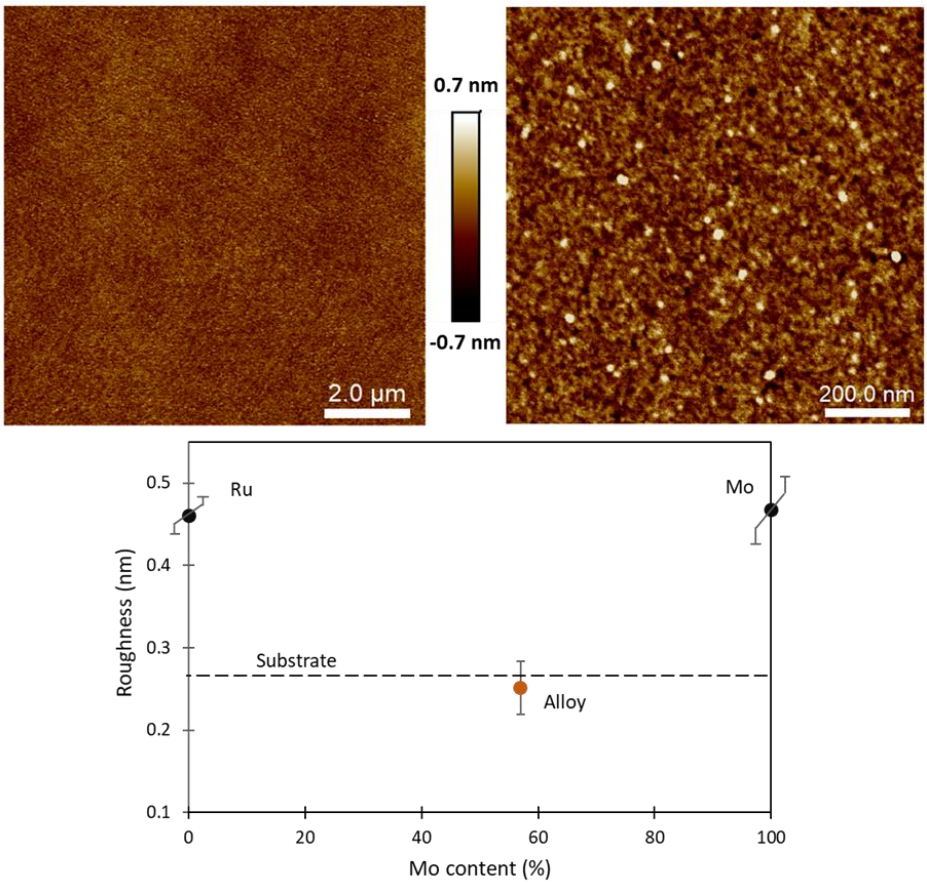

Figure 4.5 *The two upper panels are AFM height micrographs obtained on a 30 nm thick film of the $Ru_{43}Mo_{57}$ alloy, with image sizes of 10 µm × 10 µm (left) and 1 µm × 1 µm (right). Both images are displayed with the same conversion of height variations into colors, as indicated by the color bar. The pattern of parallel lines, vaguely visible in the larger-scale image, are an artifact resulting from a minor mechanical vibration. The bottom panel compares the values of the surface roughness (RMS height variation) for 20 nm thick films of pure Ru, pure Mo and the $Ru_{43}Mo_{57}$ alloy, measured from AFM images with sizes of 1 µm x 1 µm. The lower dashed line indicates the surface roughness encountered on the substrate, prior to deposition.*

The roughness of the metal films, including the RuMo alloy, is plotted in the bottom panel of Figure 4.5. Each point in the graph is the result of several AFM measurements on a different film. Whereas one might have anticipated the $Ru_{43}Mo_{57}$ mixture to adopt at best some sort of average of the roughness values of pure ruthenium and pure molybdenum films, and that any tendency to segregate would introduce extra roughness, the data clearly shows that the mixed film is significantly smoother than pure ruthenium and pure molybdenum. In fact, the alloy does not add any roughness on top of that of the underlying

substrate; within the error margin it seems to be even slightly smoother than the substrate. Note, that the alloy film in Figure 4.5 is actually thicker than the films of the two pure metals. We investigated a small number of films with a larger thickness, for which we find the same trend. For example, a 100 nm film of $Ru_{43}Mo_{57}$ exhibited a roughness of 0.43 nm, whereas the roughness of an equally thick, pure Ru film was 0.75 nm.

4.3 Discussion and conclusion

There is a simple scenario, sketched in Figure 4.6, that illustrates how the microstructure of a film, in particular the film's polycrystallinity or amorphicity, plays a dominant role in the roughness of the film. We start by emphasizing that our observations for pure ruthenium and pure molybdenum films are quite typical. The SEM micrographs and the AFM images for the pure metals show, in both cases, a polycrystalline arrangement with a significant roughness that is introduced by the grainy morphology of these films, with its typical network of grain boundary grooves (left panel of Figure 4.6). The increase of the roughness with increasing film thickness for the pure films is a direct consequence of the increasing lateral size of the grains, which is accompanied by increasing height variations[22]. We have also performed a few additional measurements for thicker films, up to film thicknesses of 100 nm. The results from those are consistent with what we report in this thesis for the thinner films.

These grain-related aspects are all absent for films with the $Ru_{43}Mo_{57}$ composition (right panel of Figure 4.6), for which both the GIXRD and the TEM data provide atomic-scale evidence that they are amorphous. The atomic arrangement of such an amorphous film does not suffer from crystal defects such as the familiar grain boundaries, where otherwise the structure would be compromised and grooves would develop at the film surface, in order to minimize grain boundary energy costs. In fact, for an amorphous film, the opposite might take place. The minimization of the surface free energy by virtue of the transient atomic mobility during the (sputter) deposition process may rather lead to surface *smoothening* instead of roughening[262]. That such smoothening is indeed at play, seems to be suggested by the reduction in apparent roughness that the surface of the $Ru_{43}Mo_{57}$ alloy film in the TEM micrograph in Figure 4.1 exhibits with respect to its interface with the underlying substrate. This also seems to be confirmed by the slightly lower AFM-value of the surface roughness of films with that composition with respect to that of the substrate (Figure 4.5), albeit that this modest difference remains within the statistical error margin. The observed roughness lies in the range of the height variations that one otherwise only finds in the case of (near)-ideal layer-by-layer growth or in the case of (near)-ideal step-flow growth of single crystals. In the layer-by-layer case, usually, the roughness progressively increases, which typically washes out the layer-by-layer character within the

first ten atomic layers, i.e. the first few nanometers. Also, in step-flow growth, statistical variations in the deposition gradually roughen up the surface. The smoothness of the $Ru_{43}Mo_{57}$ alloy film is superior to that of its crystalline counterparts and greatly exceeds our expectations.

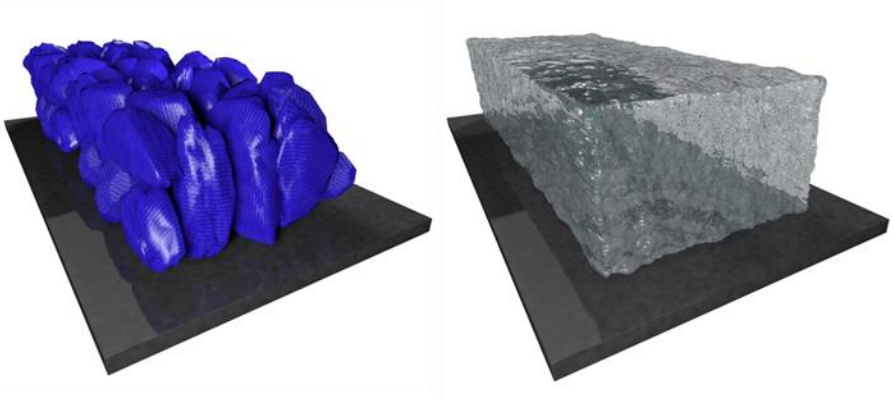

Figure 4.6 *Schematic of the two configurations encountered in this study. (Left) The typical structure of a metal film is polycrystalline, characterized by a collection of crystalline grains that, together, lead to a rough surface. (Right) The complete absence of grains makes an amorphous alloy film extremely smooth*[269]*.*

As discussed, in the context of the compositional variations, observed in Figure 4.5, our measurements indicate that amorphous RuMo layers can be deposited over a relatively wide range of compositions, similar to what was found earlier for the Cu-Zr system[171].

These results have implications that can be of relevance for potential applications of Ru and Mo coatings, for example in the context of EUV lithography technology. As we mentioned already, many problematic properties of thin metal films that limit their performance in practice, stem from their grainy nature. These disadvantages are all reduced or removed when the film can be made amorphous, providing improvements in terms of smoothness, mechanical strength, impermeability, friction and wear, corrosion resistance, and other properties. What our results for alloys of ruthenium and molybdenum show, is that with the industrially familiar technique of sputter deposition, it is relatively straightforward to deposit amorphous alloy films of molybdenum and ruthenium. The amorphicity seems to be rather robust with respect to variations in the precise alloy composition, at least for this particular combination of metals. From the perspective of applications, this even provides some flexibility to optimize the film composition for specific, chemical,

optical, or mechanical behavior, while maintaining the amorphous structure and the accompanying advantages.

Chapter 5

THERMAL STABILITY OF AMORPHOUS RUTHENIUM AND MOLYBDENUM ALLOYS

As explained in the previous two chapters, an amorphous, atomic configuration establishes an unstable arrangement. In time, such a structure tends to evolve towards ordered, i.e. crystalline configurations, which can be accelerated greatly by raising the temperature. However, when the temperature is kept low enough, the timescale for this restructuring can be long enough to make the amorphous configuration behave as if it were a thermodynamically stable phase. For practical applications of amorphous materials, it is of crucial importance to explore the range of temperatures over which the amorphicity remains robust with respect to crystallization over extended timescales.

In this chapter, I investigate the effect of heating on the atomic structure, chemical composition and compound formation of thin films of two RuMo alloys, deposited on Si(100) with a native oxide. For this purpose, I employed scanning electron microscopy, atomic force microscopy, transmission electron microscopy and x-ray photoelectron spectroscopy. I provide evidence that the thin alloy films are stable up to surprisingly high temperatures.

5.1 Introduction

Based on the TEM and GI-XRD results in Chapter 4, we concluded that RuMo alloy films, produced by sputter co-deposition of Ru and Mo from separate sources, are amorphous over a wide range of compositions, at least spanning the range from $Ru_{50}Mo_{50}$, which is close to the eutectic composition[246], to $Ru_{35}Mo_{65}$, which is close to the sigma phase[243]. As usual, this glass 'state', especially for metals, is unstable with respect to crystallization, due to the strong thermodynamic preference of metals to order. Heating or even just aging of metallic glasses, eventually, necessarily results in crystallization. This transformation proceeds in two steps. First, the nucleation of crystallites takes place, as described by classical nucleation theory (Chapter 3). This stage is followed by the subsequent growth of these crystallites. Crystallization of an amorphous film does not only alter the internal structure but also many physical properties of the system.

In the context of the investigation of layers of Ru, Mo and alloys of these two metals, including amorphous alloys, we are interested in the thermal stability of these films, in particular in the temperature regime in which the transformation of amorphous films starts towards partially or fully crystalline configurations. Additionally, we will keep an eye out for possible compound formation at high temperatures, such as we observed in Chapter 2 for systems containing Mo, Ru and Si. In Chapter 2, we concentrated on the high-temperature rearrangements and dewetting of pure Ru films, pure Mo films, and combinations of Ru and Mo films, all on the same substrate, Si(100) with a native oxide. In this chapter, we will focus on thin RuMo alloy films. We have selected two different alloy compositions. One is $Ru_{43}Mo_{57}$, which we found in Chapter 4 to be amorphous. The other is $Ru_{77}Mo_{23}$, which is crystalline and serves to compare amorphous versus crystalline behavior. We inspected the metal alloy films with SEM and TEM for imaging, EDX and XPS for elemental and chemical characterization and TEM for characterization of the crystallinity.

We will see that even after annealing at 500°C, the amorphous $Ru_{43}Mo_{57}$ film mostly preserves its glassy structure. In addition to this, a large amount of Si is found to diffuse through the metallic films from the substrate for both alloy compositions. Interestingly, the Si diffusion through the amorphous film is observed to stop before the Si reaches the surface, independently of the annealing temperature and duration. We also find that, at high temperatures, both the amorphous and the crystalline alloy film lose contact with the substrate and thus, spontaneously, form a free-standing film.

5.2 Results and discussion

We start by concentrating on the structural characteristics of a sputter-deposited $Ru_{43}Mo_{57}$ alloy film, after annealing for one hour at 500˚C. Figure 5.1 shows a cross-sectional TEM image. The image shows that the thickness of the annealed film is approximately 33 nm, which is significantly thicker than the deposited thickness of 20 nm that the film had prior to the annealing. The near-surface part of the film contains two layers with different brightness levels from the rest of the film. The outermost ~ 3 nm is clearly brighter, while the ~ 5 nm below that is somewhat darker than the interior of the film. Below, we will see that these variations correlate with compositional differences. The lower panels of Figure 5.1 are enlargements of the two marked regions, one situated largely in the darker, near-surface band and the other well within the film. Both regions exhibit complete disorder on all length scales, down to atomic dimensions. This visual impression is confirmed by the two-dimensional fast Fourier transforms (2D FFT). Similar to our results in Chapter 4 for the freshly deposited film, the broad rings in both FFTs are indicative of an amorphous atomic arrangement in both regions and the absence of orientational preferences. Note that the radius of the ring for the near-surface region is slightly larger than that for the interior of the film, corresponding to a smaller interatomic distance in the near-surface region (0.168 nm) compared to the interior of the film (0.171 nm). On the other hand, the interatomic distance was found 0.212 nm for the amorphous film prior to annealing in Chapter 4. Closer-packed amorphous arrangements can be attributed to the structural adaptation towards a more stable arrangment[270] which brings it closer to the hypothetical ideal glass [271] A densification of the amorphous network of less than 1% as a result of heat treatment was also observed in other studies[272,273] but in our case, the increase in the density is significantly higher.

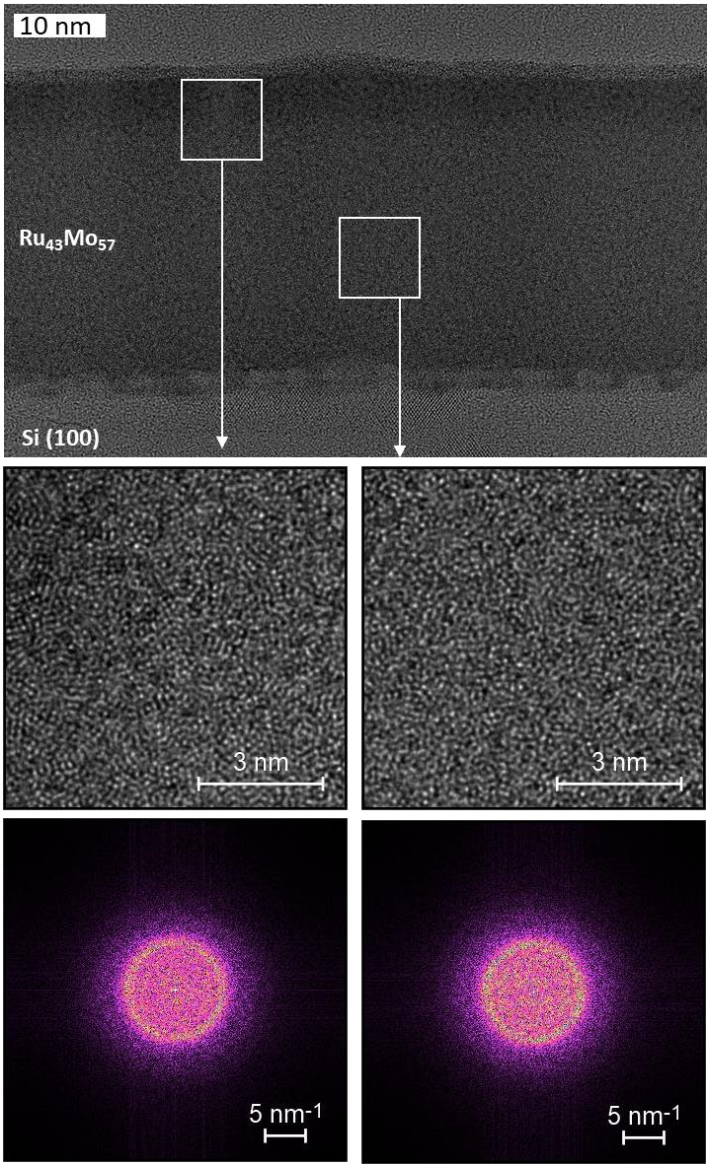

Figure 5.1 *Cross-sectional high-resolution TEM micrograph of the $Ru_{43}Mo_{57}$ alloy film on the Si(100) substrate after annealing for one hour at 500˚C. The white rectangles indicate the regions that are displayed on a magnified scale in the middle panels to emphasize the disordered arrangement in the alloy; the bottom panels are the corresponding two-dimensional fast Fourier transforms of these regions.*

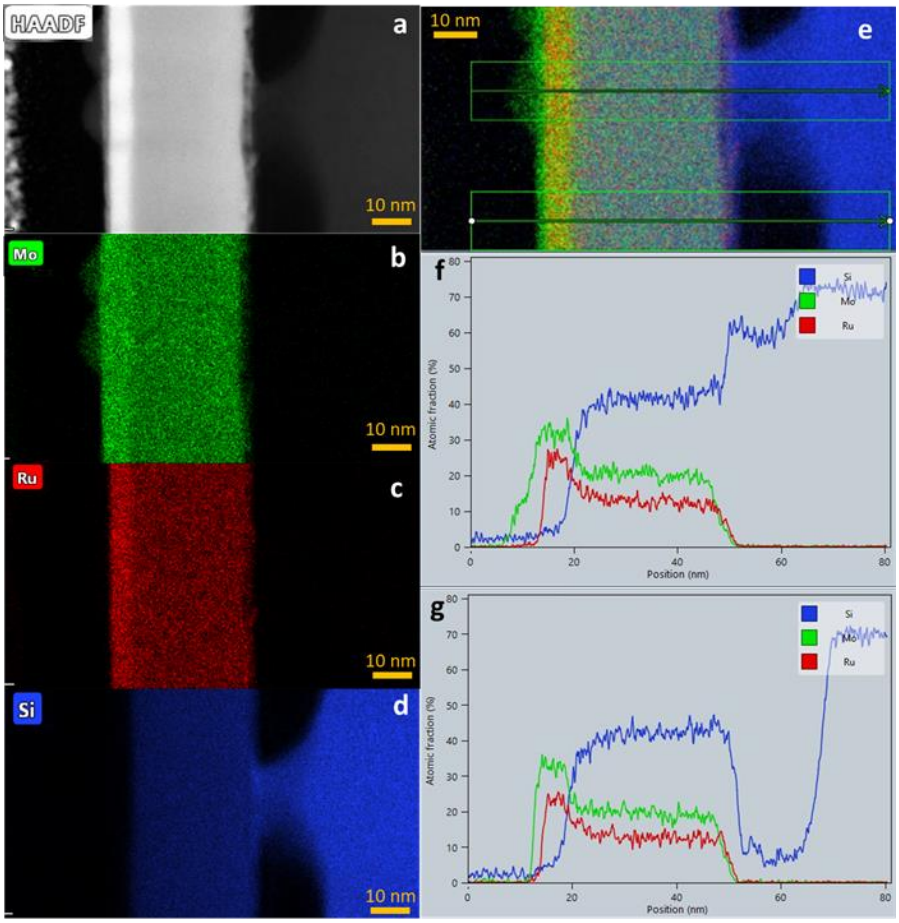

Figure 5.2 *HAADF-STEM micrograph (a) and simultaneously acquired elemental EDX maps of a* $Ru_{43}Mo_{57}$ *alloy thin film on Si(100) with a native oxide after annealing for one hour at 500˚C. Green (b), red (c) and blue (d) represent Mo, Ru and Si, respectively. Panels (g) and (f) show compositional curves for Mo, Ru and Si along the two lines (areas) in panel (e), which is a composite map, combining the three elements, each indicated by its own color.*

Figure 5.2 presents HAADF-STEM-EDX measurements on a different part of the same, annealed alloy film. Panel (a) shows the HAADF image of the $Ru_{43}Mo_{57}$ film, while panels (b), (c), (d) display the simultaneously acquired EDX maps for three elements, Mo, Ru, and Si, respectively. Panels (f) and (g) show quantitative elemental concentration curves for these three elements along the lines, indicated in panel (e).

Also, the HAADF image in panel (a) shows that the thickness of the annealed film has swollen to approximately 33 nm. The reason for the 65% expansion in film thickness with respect to the freshly deposited film can be found in the EDX map in panel (d) for Si, which is indicative of significant Si diffusion from the substrate into the film. The film can no longer be regarded as a binary alloy of Mo and Ru. The compositional curves in Figure 5.2 reveal that the film even contains more silicon than Mo and Ru, the composition being 57% Si, 25% Mo and 18% Ru, with minor compositional fluctuations. The EDX maps in panels (b) and (c) show no traces of Mo and Ru inside the Si substrate. These observations, of Si entering the metal film from the substrate, are reminiscent of our observations in Chapter 2 for the thin-film bilayer of Mo and Ru on Si(100) with a native oxide. In that case, we found that the Si atoms migrated from the single-crystalline substrate, leaving behind inverted pyramidal pits, with no evidence of Mo or Ru atoms migrating into the substrate. Also in other studies, Si atoms were identified as the dominant diffusing species in the case of molybdenum silicide formation[74,75]. With reference to the empirical rules in Chapter 3 for achieving a high GFA[114,121], we should expect that, since the introduction of Si from the substrate into the RuMo film adds a third element to the binary metal alloy, it should enhance the GFA. Additionally, the difference in atomic size between Si and the two metals should further add to the GFA. Together, these effects should provide a stabilizing effect on the amorphicity of the three-element film with respect to that of the original RuMo alloy.

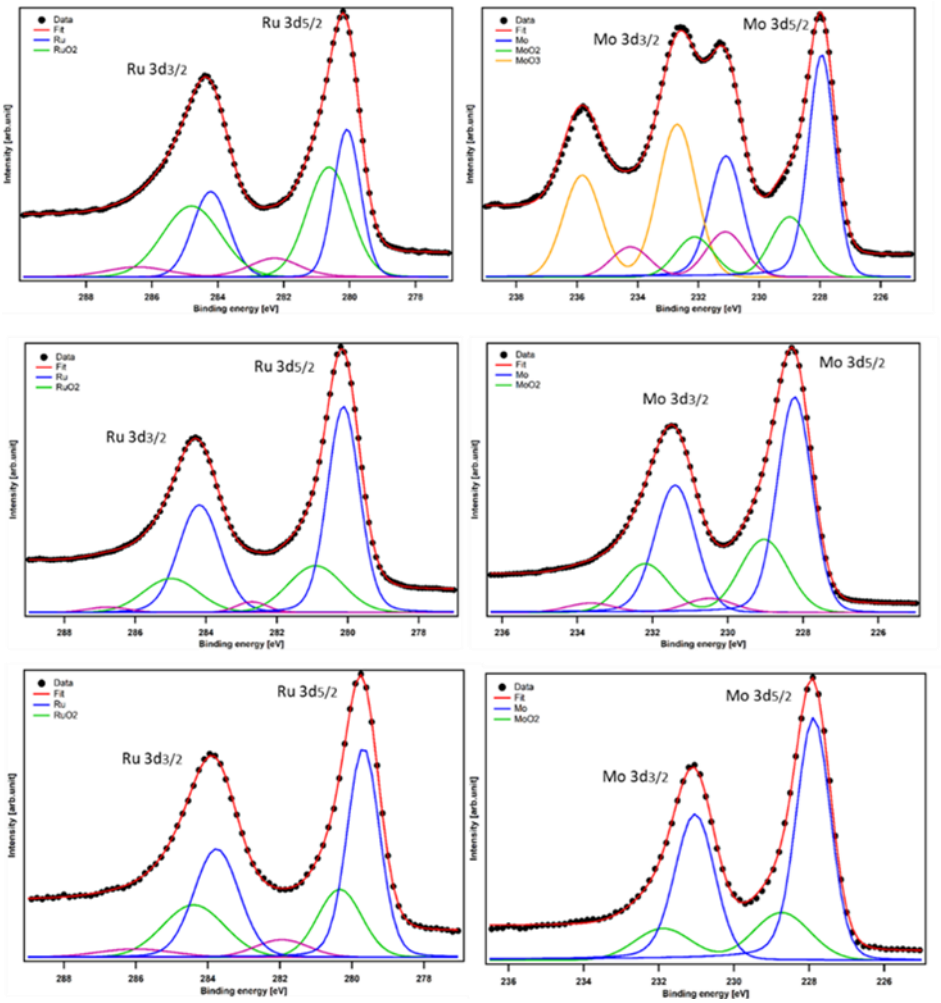

Figure 5.3 *Detailed XPS peaks of Ru (left) and Mo (right) for a $Ru_{43}Mo_{57}$ film on Si(100) with a native oxide. Top: freshly deposited; center: sputter-cleaned; bottom: at 650°C.*

film composition / treatment	$Ru_{43}Mo_{57}$	$Ru_{77}Mo_{23}$
Surface after deposition at room temp.	Ru 43% Mo 57% Si 0%	Ru 78% Mo 22% Si 0%
Sputter-cleaned surface	Ru 43% Mo 57% Si 0%	Ru 78% Mo 22% Si 0%
Surface at 650 °C	Ru 47% Mo 53% Si 0%	Ru 41.2% Mo 8.6% Si 50%
Interface at 650 °C	Ru 22% Mo 26% Si 51%	Ru 25% Mo 13% Si 62%
Substrate at 650 °C	Ru 0% Mo 0% Si 100%	Ru 0% Mo 0% Si 100%

Table 5.1 *Surface and interface concentrations of Ru, Mo and Si for the two RuMo films and their substrate, obtained from XPS measurements such as those in Figure 5.3, at various stages in the evolution of these films.*

The elemental map of Si in Figure 5.2 (e.g. panel (d) and the Si-curves in panels (f) and (g)), demonstrates that the Si diffusion through the thin $Ru_{43}Mo_{57}$ film stopped abruptly, well before the Si reached the surface of the film. In the outermost 8 nm of the film, we detected no silicon at all. The absence of silicon in the outermost region also leads to differences in contrast in the HAADF-STEM micrograph of panel (a), where it shows up brighter, and in the high-resolution TEM image in Figure 5.1 where it has a darker appearance. Further information comes from high-temperature XPS measurements, such as those shown in Figure 5.3. The surface concentrations of Ru, Mo and Si in Table 5.1, obtained from fits to the high-temperature XP spectra, show that even at 650˚C, there is still no trace of Si on the surface of the amorphous $Ru_{43}Mo_{57}$ thin film. This complete absence of Si at the surface and the abruptness of the drop in Si content inside the film make it difficult to explain the Si concentration profile merely by incomplete diffusion, for example as the result of a limited annealing temperature or duration. Instead, we interpret the profile as an indication that the outermost 8 nm of the film has adopted a special, energetically

favorable RuMo composition with a low solubility for Si and an energetic penalty against silicide formation.

Comparing Panels (b) and (c) in Figure 5.1, we see that at the surface of the film, the elemental Mo map extends 2 to 3 nm further than the Ru map and that the very surface does not contain Ru. Again, this is reflected in contrast changes in both the high-resolution TEM image of Figure 5.1 and the HAADF-STEM image of Figure 5.2. The surface enrichment with Mo suggests a further level of phase separation and it may well be that this demixing of the alloy plays a role in the later surface-induced nucleation of the crystallization of the amorphous alloy film[275] (c.f. Chapter 3).

In Figures 5.1 and 5.2, we further observe that, after annealing, the surface contains protrusions on top of the film. These introduce roughness with respect to the extreme smoothness of the as-deposited film. We have observed only a few of these protrusions over multiple cross-sectional TEM micrographs along several hundred nm. Elemental mapping in Panels (b)-(e) and the selective-area compositional curve in Panel (f) of Figure 5.2, which was chosen to run across one of the protrusions, indicate that the protrusions consist of pure Mo without significant contributions of Si or Ru. These Mo clusters may embody the next stage in the heterogeneous nucleation of phase separation and crystallization of the amorphous alloy phase. In addition to the direct energetic benefits of the segregation and clustering, the structural and compositional changes should be expected to also assist in relieving mechanical stress at the surface[276], which may add to the driving force for surface crystallization.

An interesting observation in Figure 5.2, is that the image and all EDX maps indicate that the film partially detached from the substrate. Also macroscopically, we observed the detachment of alloy films of Mo and Ru with various compositions after annealing at least at 400°C. In a separate publication, we presented an in-depth analysis of this type of delamination for various thin films, including elemental Mo, Ru, a RuMo alloy and a high-entropy alloy of HfMoNbTiZr on Si(100) substrates with a native oxide, and concluded that Ru is an essential element at the interface for the thin films to detach from the substrate, the underlying mechanism being based on the formation of Ru silicide[274]. In chapter 2, I showed that the Mo thin films on Si(100) substrate provide better thermal stability compared to Ru thin films on the same substrate. We claimed that the interfacial silicide formation leads to better adhesion of Mo to Si, which increases the thermal stability for Mo films on Si against dewetting. It remains to be investigated, why interfacial silicide formation seems not to generate a similarly strong adhesion of Ru thin films to Si substrates. We assume that this is connected with the tendency for Ru-containing films to delaminate from Si and speculate that the common origin for both phenomena lies in the generation of high compressive stress during Ru silicide formation.

As a result of this annealing-induced detachment, we found that it was possible to readily exfoliate annealed alloy films over macroscopic distances, simply by use of tweezers. This resulted in freestanding flakes with lateral dimensions in the centimeter regime, as can be seen in Figure 5.4. Here, we will not discuss possibilities for practical applications of this method to generate macroscopic, ultrathin metal foils, but rather use the easy delamination as a convenient way to inspect not only the outer surface of the film but also its interface to the substrate, as well as the underlying substrate itself.

Figure 5.4 *Photograph, showing a pair of tweezers (dark object coming in from the top) that holds a freestanding, metallic thin film of* $Ru_{77}Mo_{23}$ *with a thickness of 200 nm, after annealing-induced delamination at 700˚C from the oxidized Si(100) substrate.*

Figure 5.5 presents SEM images of the free-standing thin $Ru_{77}Mo_{23}$ film that was obtained by annealing the system for one hour to 700˚C. The images were taken on the surface of the delaminated alloy film (upper panels), on the thin-film side of the film-substrate interface (middle panels), and on the substrate side of that interface (bottom panels), each time with a larger-scale image on the left and a higher magnification on the right. The upper SEM images, in particular the one in the upper right panel, show granular structures, which should be regarded as the typical signature of the nanoscale polycrystallinity of the annealed metal film. The average grain size is approximately 17 nm. At the interface (middle panels), the film exhibits a characteristic pattern of smaller and larger features, the larger ones appearing as craters, with a lateral length scale of several μm, significantly exceeding the 200 nm thickness of the film. Note, that these features do not show up in any way at the surface of the film (upper panels). As the bottom panels show, the 'craters' are also not reflected on the side of the substrate that became exposed after the delamination. Instead, on that side, we observe pyramidal craters in the substrate, similar to the ones we observed in Chapter 2 for the bilayer thin films of Mo and Ru on oxide-covered Si(100), after annealing at and above 700°C. The pyramidal pits in Chapter 2 were

identified as etch pits in the (100) surface, each one formed by four {111} surfaces, the low-energy surfaces of Si. The Si missing from the pits was found to be incorporated in silicide 'nano-flowers' that covered the pits and the central part of each flower was found to be freely suspended over its own pit. The mechanism that we proposed in Chapter 2 for the formation of these structures was that, at elevated temperatures, Si atoms would be able to diffuse through specific defects in the native oxide that covered the Si substrate. This would bring them in touch with the Mo layer and enable them to form a silicide, a process that would radially convert the metal film, with the defect in the oxide layer marking the central location, i.e. the center of both the nano-flower and the pyramid. The rugged shape of the 'base' of the pyramidal pit in the bottom right panel of Figure 5.5 seems to indicate that the delamination process has still left behind a thin overlayer on the Si substrate that seems to establish a minor overhang over the edges of the pyramidal pit and thus to hide these edges from view. The bright decoration of the rugged edge may indicate a reduced electrical conductivity of the film with respect to the Si substrate, making the overhanging parts of the film charge up and enhancing their secondary electron emission in comparison with the regions where the film is in contact with the substrate. The XPS results that we discuss below, indicate that this film cannot be the native oxide that originally covered the Si substrate.

The surface and interface compositions in Table 5.1 were derived from in-situ XPS measurements, partly taken at an elevated temperature of 650°C. These measurements were conducted both on a fully amorphous $Ru_{43}Mo_{57}$ film and on a nano-crystalline $Ru_{77}Mo_{23}$ film. After the annealing, both films were lifted off from the substrate, while we kept the system in an ultrahigh vacuum, thus allowing us to investigate the interface, surface, and substrate compositions without exposure to ambient conditions during or after the annealing and delamination. Whereas the overall evolution of the amorphous alloy is similar to that of the nano-crystalline, Ru-rich alloy, there is a significant difference between the two at 650°C, where the surface of the amorphous film contains no Si, while Si has already reached a concentration of 50% at the surface of the nano-crystalline film. Another observation of interest is that the XPS spectra after exfoliation show SiO_2 signals at the interface only on the thin-film side but not on the substrate side (not shown in Table 5.1). This indicates that the films delaminate from the Si substrate together with its native oxide. However, as the bottom SEM images in Figure 5.5 show, the substrate that is exposed after annealing-induced delamination seems still to be covered by a thin overlayer. The XPS spectra on the exposed substrate (Table 5.1) also do not contain signals from Ru or Mo, which also excludes the possibility that the overlayer would be a thin metal or metal silicide film.

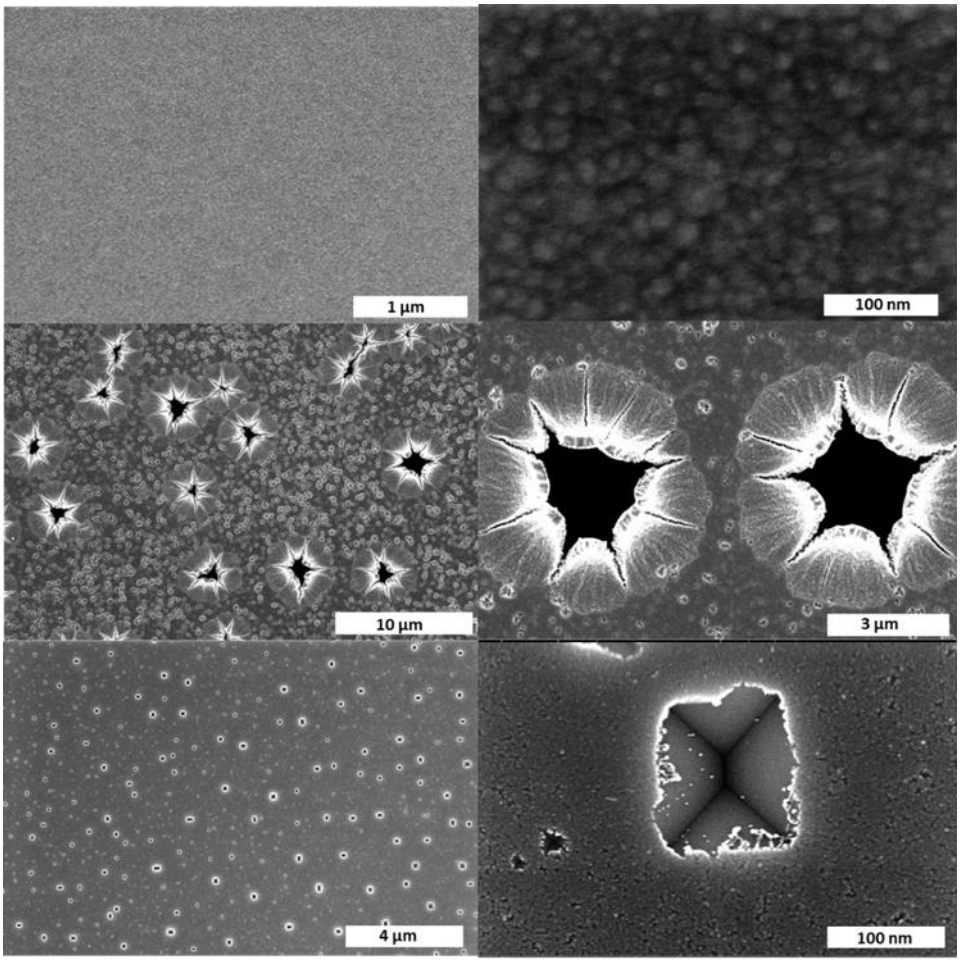

Figure 5.5 *SEM micrographs, taken after the delamination of a 200 nm thick free-standing $Ru_{77}Mo_{23}$ alloy film annealed at 700°C. The upper two images show the outer surface of the delaminated film. The middle two images were taken on the interface between the film and the substrate. The bottom two images present the Si(100) substrate after the delamination of the thin film.*

5.3 Conclusions

In summary, we used multiple techniques to investigate the thermal evolution of thin alloy films of Ru and Mo, obtained by sputter co-deposition on Si(100) substrates with a native oxide. High-resolution TEM images and the corresponding 2D-FFTs showed that the amorphous alloy film, $Ru_{43}Mo_{57}$, preserves amorphicity after annealing at 500°C. STEM-EDX mapping reveals that, during the annealing, a high concentration of Si is incorporated in the alloy films, which originates from the underlying substrate. The introduction of Si in the amorphous MoRu alloy is thought to increase the GFA of the alloy by introducing an extra element with a much smaller atomic size.

Based on the EDX mapping and the XPS spectra of the annealed films, we also concluded that the migration of the Si stops before it reaches the surface of the amorphous film, while the more Ru-rich alloy, $Ru_{77}Mo_{23}$, was found to contain a dominant amount of silicon on the surface. This rejection of Si at the surface of the amorphous film could be interesting as a practical means to keep surfaces of Si-containing materials clean of Si, thus potentially avoiding some of the undesired phenomena that are typical for Si-containing structures in EUV lithography applications.

Finally, at high temperatures, both the nano-crystalline and the amorphous alloy film lose contact with the substrate, which we ascribe to the formation of Ru silicide. This delamination behavior may serve as a practical approach towards the production of free-standing, ultrathin metallic films.

REFERENCES

1. Hall, P. *Indonesia, Malaysia & Singapore Handbook*. (Trade & Trade & Travel Publications ; New York, NY, 1993).

2. Aubert, M., Brumm, A., Ramli, M., Sutikna, T., Saptomo, E. W., Hakim, B., Morwood, M. J., van den Bergh, G. D., Kinsley, L. & Dosseto, A. Pleistocene cave art from Sulawesi, Indonesia. *Nature* **514,** 223–227 (2014).

3. Hoffmann, D. L., Standish, C. D., García-Diez, M., Pettitt, P. B., Milton, J. A., Zilhão, J., Alcolea-González, J. J., Cantalejo-Duarte, P., Collado, H., de Balbín, R., Lorblanchet, M., Ramos-Muñoz, J., Weniger, G.-Ch. & Pike, A. W. G. U-Th dating of carbonate crusts reveals Neandertal origin of Iberian cave art. *Science* **359,** 912–915 (2018).

4. Greene, J. E. Tracing the 5000-year recorded history of inorganic thin films from ∼3000 BC to the early 1900s AD. *Applied Physics Reviews* **1,** 041302 (2014).

5. Ketov, S. V., Shi, X., Xie, G., Kumashiro, R., Churyumov, A. Yu., Bazlov, A. I., Chen, N., Ishikawa, Y., Asao, N., Wu, H. & Louzguine-Luzgin, D. V. Nanostructured Zr-Pd Metallic Glass Thin Film for Biochemical Applications. *Sci Rep* **5,** 7799 (2015).

6. Sahu, D. R., Lin, S.-Y. & Huang, J.-L. ZnO/Ag/ZnO multilayer films for the application of a very low resistance transparent electrode. *Applied Surface Science* **252,** 7509–7514 (2006).

7. Kim, M.-G., Kanatzidis, M. G., Facchetti, A. & Marks, T. J. Low-temperature fabrication of high-performance metal oxide thin-film electronics via combustion processing. *Nature Mater* **10,** 382–388 (2011).

8. Zhang, Y.-W., Wu, B.-Y., Chen, K.-C., Wu, C.-H. & Lin, S.-Y. Highly conductive nanometer-thick gold films grown on molybdenum disulfide surfaces for interconnect applications. *Sci Rep* **10,** 14463 (2020).

9. Leyland, A. & Matthews, A. Design criteria for wear-resistant nanostructured and glassy-metal coatings. *Surface and Coatings Technology* **177–178,** 317–324 (2004).

10. Kondratiuk, J. & Kuhn, P. Tribological investigation on friction and wear behaviour of coatings for hot sheet metal forming. *Wear* **270,** 839–849 (2011).

11. Cihan, E., Störmer, H., Leiste, H., Stüber, M. & Dienwiebel, M. Low friction of metallic multilayers by formation of a shear-induced alloy. *Sci Rep* **9,** 9480 (2019).

12. Jahanmir, S., Abrahamson, E. P. & Suh, N. P. Sliding wear resistance of metallic coated surfaces. *Wear* **40,** 75–84 (1976).

13. van Zwol, P. J., Vles, D. F., Voorthuijzen, W. P., Péter, M., Vermeulen, H., van de Kruijs, E. & Bijkerk, F. Emissivity of freestanding membranes with thin metal coatings. *J. Appl. Phys.* 6 (2015).

14. Peng, L., Liu, D. & Cheng, H. Design and fabrication of the ultrathin metallic film based infrared selective radiator. *Solar Energy Materials and Solar Cells* **193,** 7–12 (2019).

15. Rouard, P. & Meessen, A. in *Progress in Optics* (ed. Wolf, E.) **15,** 77–137 (Elsevier, 1977).

16. Axelevitch, A., Gorenstein, B. & Golan, G. Investigation of Optical Transmission in Thin Metal Films. *Physics Procedia* **32,** 1–13 (2012).

17. Thomson, T. in *Metallic Films for Electronic, Optical and Magnetic Applications* 454–546 (Elsevier, 2014

18. Scheunert, G., Heinonen, O., Hardeman, R., Lapicki, A., Gubbins, M. & Bowman, R. M. A review of high magnetic moment thin films for microscale and nanotechnology applications. *Appl. Phys. Rev.* **3,** 011301 (2016).

19. Litteken, C. S., Strohband, S. & Dauskardt, R. H. Residual stress effects on plastic deformation and interfacial fracture in thin-film structures. *Acta Materialia* **53,** 1955–1961 (2005).

20. Shekhah, O., Liu, J., Fischer, R. A. & Wöll, C. MOF thin films: existing and future applications. *Chem. Soc. Rev.* **40,** 1081–1106 (2011).

21. Zhao, J., Deng, Q., Bachmatiuk, A., Sandeep, G., Popov, A., Eckert, J. & Rümmeli, M. H. Free-Standing Single-Atom-Thick Iron Membranes Suspended in Graphene Pores. *Science* **343,** 1228–1232 (2014).

22. Rost, M. J., Quist, D. A. & Frenken, J. W. M. Grains, Growth, and Grooving. *Phys. Rev. Lett.* **91,** 026101 (2003).

23. Kaplan, W. D., Chatain, D., Wynblatt, P. & Carter, W. C. A review of wetting versus adsorption, complexions, and related phenomena: the rosetta stone of wetting. *J Mater Sci* **48,** 5681–5717 (2013).

24. Thompson, C. V. Solid-State Dewetting of Thin Films. *Annu. Rev. Mater. Res.* **42,** 399–434 (2012).

25. Che, J. G., Chan, C. T., Jian, W.-E. & Leung, T. C. Surface atomic structures, surface energies, and equilibrium crystal shape of molybdenum. *Phys. Rev. B* **57,** 1875–1880 (1998).

26. Skriver, H. L. & Rosengaard, N. M. Surface energy and work function of elemental metals. *Phys. Rev. B* **46,** 7157–7168 (1992).

27. Gilman, J. J. Direct Measurements of the Surface Energies of Crystals. *Journal of Applied Physics* **31,** 2208–2218 (1960).

28. Bisaro, R., Magariño, J., Proust, N. & Zellama, K. Structure and crystal growth of atmospheric and low-pressure chemical-vapor-deposited silicon films. *Journal of Applied Physics* **59,** 1167–1178 (1986).

29. Narayan, S. R., Day, J. M., Thinakaran, H. L., Herbots, N., Bertram, M. E., Cornejo, C. E., Diaz, T. C., Kavanagh, K. L., Culbertson, R. J., Ark, F. J., Ram, S., Mangus, M. W. & Islam, R. Comparative Study of Surface Energies of Native Oxides of Si(100) and Si(111) via Three Liquid Contact Angle Analysis. *MRS Adv.* **3,** 3379–3390 (2018).

30. Gadkari, P. R., Warren, A. P., Todi, R. M., Petrova, R. V. & Coffey, K. R. Comparison of the agglomeration behavior of thin metallic films on SiO2. *Journal of Vacuum Science & Technology A: Vacuum, Surfaces, and Films* **23,** 1152–1161 (2005).

31. Touloukian, Y. S. *Thermophysical properties of matter. metallic elements and alloys Vol. 12, Vol. 12,*. (IFI/Plenum, 1975).

32. El-Kareh, B. & Hutter, L. N. *Fundamentals of Semiconductor Processing Technology*. (Springer US, 1995).

33. Vrij, A. Possible mechanism for the spontaneous rupture of thin, free liquid films. *Discuss. Faraday Soc.* **42,** 23 (1966).

34. Wyart, F. B. & Daillant, J. Drying of solids wetted by thin liquid films. *Can. J. Phys.* **68,** 1084–1088 (1990).

35. Herminghaus, S., Jacobs, K., Mecke, K., Bischof, J., Fery, A., Ibn-Elhaj, M. & Schlagowski, S. Spinodal Dewetting in Liquid Crystal and Liquid Metal Films. *Science* **282,** 916–919 (1998).

36. Sundar, A., Decker, C. J., Hughes, R. A. & Neretina, S. The templated assembly of highly faceted three-dimensional gold microstructures into periodic arrays. *Materials Letters* **76,** 155–158 (2012).

37. Petersen, J. & Mayr, S. G. Dewetting of Ni and NiAg solid thin films and formation of nanowires on ripple patterned substrates. *Journal of Applied Physics* **103,** 023520 (2008).

38. Ling, W. L., Giessel, T., Thürmer, K., Hwang, R. Q., Bartelt, N. C. & McCarty, K. F. Crucial role of substrate steps in de-wetting of crystalline thin films. *Surface Science* **570,** L297–L303 (2004).

39. Ishikawa, Y., Kumezawa, M., Nuryadi, R. & Tabe, M. Effect of patterning on thermal agglomeration of ultrathin silicon-on-insulator layer. *Applied Surface Science* **190,** 11–15 (2002).

40. Génin, F. Y., Mullins, W. W. & Wynblatt, P. Capillary instabilities in thin films: A model of thermal pitting at grain boundary vertices. *Acta Metallurgica et Materialia* **40,** 3239–3248 (1992).

41. Génin, F. Y., Mullins, W. W. & Wynblatt, P. Capillary instabilities in polycrystalline metallic foils: Experimental observations of thermal pitting in nickel. *Acta Metallurgica et Materialia* **42,** 1489–1492 (1994).

42. Srolovitz, D. J. & Safran, S. A. Capillary instabilities in thin films. I. Energetics. *Journal of Applied Physics* **60,** 247–254 (1986).

43. Shaffir, E., Riess, I. & Kaplan, W. D. The mechanism of initial de-wetting and detachment of thin Au films on YSZ. *Acta Materialia* **57,** 248–256 (2009).

44. Hanief, N., Topić, M. & Pineda-Vargas, C. Solid-state dewetting of continuous thin platinum coatings. *Nuclear Instruments and Methods in Physics Research Section B: Beam Interactions with Materials and Atoms* **363,** 173–176 (2015).

45. Oh, H., Lee, J., Seo, M., Baek, I. U., Byun, J. Y. & Lee, M. Laser-Induced Dewetting of Metal Thin Films for Template-Free Plasmonic Color Printing. *ACS Appl. Mater. Interfaces* **10,** 38368–38375 (2018).

46. Sonawane, D., Choudhury, A. & Kumar, P. New Insights into Dewetting of Cu Thin Films Deposited on Si. *Langmuir* (2020). doi:10.1021/acs.langmuir.0c00575

47. Zhang, S.-L. & Östling, M. Metal Silicides in CMOS Technology: Past, Present, and Future Trends. 130

48. Datta, D. P., Siva, V., Varma, S., Kanjilal, D. & Sahoo, P. K. Ion induced dewetting of Au–Si on a SiO2 surface: composite nanodot evolution and wettability transition. *Phys. Chem. Chem. Phys.* **18,** 29955–29960 (2016).

49. Jahan, C., Faynot, O., Tosti, L. & Hartmann, J. M. Agglomeration control during the selective epitaxial growth of Si raised sources and drains on ultra-thin silicon-on-insulator substrates. *Journal of Crystal Growth* **280,** 530–538 (2005).

50. Danielson, D. T., Sparacin, D. K., Michel, J. & Kimerling, L. C. Surface-energy-driven dewetting theory of silicon-on-insulator agglomeration. *Journal of Applied Physics* **100,** 083507 (2006).

51. Cao, P., Bai, P., Omrani, A. A., Xiao, Y., Meaker, K. L., Tsai, H.-Z., Yan, A., Jung, H. S., Khajeh, R., Rodgers, G. F., Kim, Y., Aikawa, A. S., Kolaczkowski, M. A., Liu, Y., Zettl, A., Xu, K., Crommie, M. F. & Xu, T. Preventing Thin Film Dewetting via Graphene Capping. *Adv. Mater.* **29,** 1701536 (2017).

52. White, B. C., Behbahanian, A., Stoker, T. M., Fowlkes, J. D., Hartnett, C., Rack, P. D. & Roberts, N. A. The effect of different thickness alumina capping layers on the final morphology of dewet thin Ni films. *Appl. Phys. A* **124,** 233 (2018).

53. Choi, S.-H. & Zhang Newby, B. Suppress polystyrene thin film dewetting by modifying substrate surface with aminopropyltriethoxysilane. *Surface Science* **600,** 1391–1404 (2006).

54. Holmes, M. A., Mackay, M. E. & Giunta, R. K. Nanoparticles for dewetting suppression of thin polymer films used in chemical sensors. *J Nanopart Res* **9,** 753–763 (2007).

55. Louis, E., Yakshin, A. E., Tsarfati, T. & Bijkerk, F. Nanometer interface and materials control for multilayer EUV-optical applications. *Progress in Surface Science* **86,** 255–294 (2011).

56. Louis, E., Yakshin, A. E., Goerts, P. C., Oestreich, S., Stuik, R., Maas, E. L. G., Kessels, M. J. H., Bijkerk, F., Haidl, M., Muellender, S., Mertin, M., Schmitz, D., Scholze, F. & Ulm, G. Progress in Mo/Si multilayer coating technology for EUVL optics. in *Emerging Lithographic Technologies IV* **3997,** 406–411 (International Society for Optics and Photonics, 2000).

57. Flextura Sputter. *Polyteknik* at <http://www.polyteknik.com/products/industrial-pvd-systems/flextura-sputter/>

58. Wasa, K. & Hayakawa, S. Handbook of sputter deposition technology. (William Andrew, 1992).

59. Collver, M. M. & Hammond, R. H. Stability of amorphous transition-metal films. *J. Appl. Phys.* **49,** 2420 (1978).

60. Chen, Y.-I., Liu, K.-T., Wu, F.-B. & Duh, J.-G. Mo–Ru coatings on tungsten carbide by direct current magnetron sputtering. *Thin Solid Films* **515,** 2207–2212 (2006).

61. Scanning Electron Microscopes at <//www.thermofisher.com/uk/en/home/electron-microscopy/products/scanning-electron-microscopes.html>

62. Reimer, L. Scanning Electron Microscopy: Physics of Image Formation and Microanalysis, Second Edition. *Meas. Sci. Technol.* **11,** 1826–1826 (2000).

63. Franz J. Giessibl, Advances in atomic force microscopy. Rev. Mod. Phys. **75**, 949 (2003).

64. Dimension Icon Overview - Performance AFMs. *Bruker.com* at <https://www.bruker.com/products/surface-and-dimensional-analysis/atomic-force-microscopes/dimension-icon/overview.html>

65. Shindo, D. & Oikawa, T. in *Analytical Electron Microscopy for Materials Science* (eds. Shindo, D. & Oikawa, T.) 81–102 (Springer Japan, 2002).

66. Heide, P. van der. *X-ray Photoelectron Spectroscopy: An introduction to Principles and Practices*. (John Wiley & Sons, 2011).

67. Feature´s highlights | kolibrik.net. at <https://www.kolibrik.net/en/kolxpd/features-highlights>

68. Reimer, L. *Transmission Electron Microscopy: Physics of Image Formation and Microanalysis*. (Springer, 2013).

69. Sfiligoj, C. *Towards stable nanolayers for EUV optics*. (PhD thesis, University of Amsterdam, 2021). at <https://pure.uva.nl/ws/files/61819858/Thesis.pdf>

70. Reinink, J., Zameshin, A., van de Kruijs, R. W. E. & Bijkerk, F. In-situ studies of silicide formation during growth of molybdenum-silicon interfaces. *Journal of Applied Physics* **126,** 135304 (2019).

71. Windt, D. L., Hull, R. & Waskiewicz, W. K. Interface imperfections in metal/Si multilayers. *Journal of Applied Physics* **71,** 2675–2678 (1992).

72. Petford-Long, A. K., Stearns, M. B., Chang, C. -H., Nutt, S. R., Stearns, D. G., Ceglio, N. M. & Hawryluk, A. M. High-resolution electron microscopy study of x-ray multilayer structures. *Journal of Applied Physics* **61,** 1422–1428 (1987).

73. Holloway, K., Do, K. B. & Sinclair, R. Interfacial reactions on annealing molybdenum-silicon multilayers. *Journal of Applied Physics* **65,** 474–480 (1989).

74. Reinink, J., Zameshin, A., van de Kruijs, R. W. E. & Bijkerk, F. In-situ studies of silicide formation during growth of molybdenum-silicon interfaces. *Journal of Applied Physics* **126,** 135304 (2019).

75. Fokkema, V. Real-time scanning tunneling microscopy studies of thin film deposition and ion erosion. (PhD thesis, Leiden University, 2011).

76. Yanagisawa, S. Reaction of Mo Thin Films on Si (100) Surfaces. *J. Electrochem. Soc.* **127,** 1150 (1980).

77. Guivarc'h, A., Auvray, P., Berthou, L., Le Cun, M., Boulet, J. P., Henoc, P., Pelous, G. & Martinez, A. Reaction kinetics of molybdenum thin films on silicon (111) surface. *Journal of Applied Physics* **49,** 233–237 (1978).

78. Nik, S., Krantz, P., Zeng, L., Greibe, T., Pettersson, H., Gustafsson, S., Delsing, P. & Olsson, E. Correlation between Al grain size, grain boundary grooves and local variations in oxide barrier thickness of Al/AlOx/Al tunnel junctions by transmission electron microscopy. *Springerplus* **5,** 1067 (2016).

79. Dang, W. L., Fu, Y. Q., Luo, J. K., Flewitt, A. J. & Milne, W. I. Deposition and characterization of sputtered ZnO films. *Superlattices and Microstructures* **42,** 89–93 (2007).

80. Lee, H.-J., Zhang, P. & Bravman, J. C. Tensile failure by grain thinning in micromachined aluminum thin films. *Journal of Applied Physics* **93,** 1443–1451 (2003).

81. Krause, B., Abadias, G., Michel, A., Wochner, P., Ibrahimkutty, S. & Baumbach, T. Direct Observation of the Thickness-Induced Crystallization and Stress Build-Up during Sputter-Deposition of Nanoscale Silicide Films. *ACS Appl. Mater. Interfaces* **8,** 34888–34895 (2016).

82. Chelvanathan, P., Zakaria, Z., Yusoff, Y., Akhtaruzzaman, M., Alam, M. M., Alghoul, M. A., Sopian, K. & Amin, N. Annealing effect in structural and electrical properties of sputtered Mo thin film. *Applied Surface Science* **334,** 129–137 (2015).

83. Wang, H., Zhang, Z., Wong, L. M., Wang, S., Wei, Z., Li, G. P., Xing, G., Guo, D., Wang, D. & Wu, T. Shape-Controlled Fabrication of Micro/Nanoscale Triangle, Square, Wire-like, and Hexagon Pits on Silicon Substrates Induced by Anisotropic Diffusion and Silicide Sublimation. *ACS Nano* **4,** 2901–2909 (2010).

84. Zhang, Z., Wong, L. M., Ong, H. G., Wang, X. J., Wang, J. L., Wang, S. J., Chen, H. & Wu, T. Self-Assembled Shape- and Orientation-Controlled Synthesis of Nanoscale Cu $_3$$ Si Triangles, Squares, and Wires. *Nano Lett.* **8,** 3205–3210 (2008).

85. Jaccodine, R. J. Surface Energy of Germanium and Silicon. *J. Electrochem. Soc.* **110,** 524 (1963).

86. Hesketh, P. J., Ju, C., Gowda, S., Zanoria, E. & Danyluk, S. Surface Free Energy Model of Silicon Anisotropic Etching. *J. Electrochem. Soc.* **140,** 1080–1085 (2019).

87. Zhou, H., Fu, J. & Silver, R. M. The Influence of Defects on the Morphology of Si (111) Etched in NH $_4$ F. *J. Phys. Chem. B* **109,** 23386–23394 (2005).

88. Cabral Jr, C., Lavoie, C., Harper, J. M. E. & Jordan-Sweet, J. The use of in situ X-ray diffraction, optical scattering and resistance analysis techniques for evaluation of copper diffusion barriers in blanket films and damascene structures. *Thin Solid Films* **397,** 194–202 (2001).

89. Giermann, A. L. & Thompson, C. V. Solid-state dewetting for ordered arrays of crystallographically oriented metal particles. *Appl. Phys. Lett.* **86,** 121903 (2005).

90. Motorin, V. I. Vitrification kinetics of pure metals. *Phys. Stat. Sol. (a)* **80,** 447–455 (1983).

91. Zhong, L., Wang, J., Sheng, H., Zhang, Z. & Mao, S. X. Formation of monatomic metallic glasses through ultrafast liquid quenching. *Nature* **512,** 177–180 (2014).

92. Jean-Pierre Hansen and Ian R. McDonald. *Theory of Simple Liquids (Fourth Edition)* (Academic Press, 2013).

93. Salmon, P. S. Order within disorder. *Nature Mater* **1,** 87–88 (2002).

94. Poate, J. M., Peercy, P. S. & Thompson, M. O. The Melting of Amorphous Si. *MRS Proc.* **57,** 465 (1985).

95. Greer, A. L. Metallic Glasses. *Science* **267,** 1947–1953 (1995).

96. Gaskell, P. H. & Smith, D. J. Investigations of the structure of amorphous and partially crystalline metallic alloys by high resolution electron microscopy. *Journal of Microscopy* **119,** 63–72 (1980).

97. Gupta, P. K. Non-crystalline solids: glasses and amorphous solids. *Journal of Non-Crystalline Solids* **195,** 158–164 (1996).

98. Hu, X., Ng, S. C., Feng, Y. P. & Li, Y. Cooling-rate dependence of the density of Pd 40 Ni 10 Cu 30 P 20 bulk metallic glass. *Phys. Rev. B* **64,** 172201 (2001).

99. Greer, A. L. in *Physical Metallurgy* 305–385 (Elsevier, 2014).

100. Duwez, P., Willens, R. H. & Klement, W. Continuous Series of Metastable Solid Solutions in Silver-Copper Alloys. *Journal of Applied Physics* **31,** 1136–1137 (1960).

101. Klement, W., Willens, R. H. & Duwez, P. Non-crystalline Structure in Solidified Gold–Silicon Alloys. *Nature* **187,** 869–870 (1960).

102. Chen, H. S. & Turnbull, D. Evidence of a Glass–Liquid Transition in a Gold–Germanium–Silicon Alloy. *The Journal of Chemical Physics* **48,** 2560–2571 (1968).

103. Chen, H. S. Thermodynamic considerations on the formation and stability of metallic glasses. *Acta Metallurgica* **22,** 1505–1511 (1974).

104. Drehman, A. J., Greer, A. L. & Turnbull, D. Bulk formation of a metallic glass: $Pd_{40}Ni_{40}P_{20}$. *Appl. Phys. Lett.* **41,** 716–717 (1982).

105. Kui, H. W., Greer, A. L. & Turnbull, D. Formation of bulk metallic glass by fluxing. *Appl. Phys. Lett.* **45,** 615–616 (1984).

106. Inoue, A., Nishiyama, N. & Kimura, H. Preparation and Thermal Stability of Bulk Amorphous Pd40Cu30Ni10P20 Alloy Cylinder of 72 mm in Diameter. *Materials Transactions, JIM* **38,** 179–183 (1997).

107. Leamy, H. J. & Dirks, A. G. Microstructure and magnetism in amorphous rare-earth–transition-metal thin films. I. Microstructure. *Journal of Applied Physics* **49,** 3430–3438 (1978).

108. Rivory, J., Frigerio, J. M., Harmelin, M., Quivy, A., Calvayrac, Y. & Bigot, J. Preperation of CuZr Metallic glasses by sputtering and their thermal stability, electrical and optical properties.

109. Chu, J. P., Jang, J. S. C., Huang, J. C., Chou, H. S., Yang, Y., Ye, J. C., Wang, Y. C., Lee, J. W., Liu, F. X., Liaw, P. K., Chen, Y. C., Lee, C. M., Li, C. L. & Rullyani, C. Thin film metallic glasses: Unique properties and potential applications. *Thin Solid Films* **520,** 5097–5122 (2012).

110. Chou, H. S., Huang, J. C. & Chang, L. W. Mechanical properties of ZrCuTi thin film metallic glass with high content of immiscible tantalum. *Surface and Coatings Technology* **205,** 587–590 (2010).

111. Ma, E. Alloys created between immiscible elements. *Progress in Materials Science* **50,** 413–509 (2005).

112. Chen, C. J., Huang, J. C., Chou, H. S., Lai, Y. H., Chang, L. W., Du, X. H., Chu, J. P. & Nieh, T. G. On the amorphous and nanocrystalline Zr–Cu and Zr–Ti co-sputtered thin films. *Journal of Alloys and Compounds* **483,** 337–340 (2009).

113. Turnbull, D. Under what conditions can a glass be formed? *Contemporary Physics* **10,** 473–488 (1969).

114. Johnson, W. L. Bulk Glass-Forming Metallic Alloys: Science and Technology. *MRS Bull.* **24,** 42–56 (1999).

115. Lu, Z. P. & Liu, C. T. A new glass-forming ability criterion for bulk metallic glasses. *Acta Materialia* **50,** 3501–3512 (2002).

116. Qing-Jun et al. - Glass-Forming Ability of an Iron-Based Alloy Enhanced by Co Addition and Evaluated by a New Criterion, Chinese Physics Letters **22**, 1736 (2005).

117. Fan, G. J., Choo, H. & Liaw, P. K. A new criterion for the glass-forming ability of liquids. *Journal of Non-Crystalline Solids* **353,** 102–107 (2007).

118. Ji, X., Pan, Y. & Ni, F. A thermodynamic criterion for predicting glass-forming ability in binary metallic glasses. *Materials & Design* **30,** 842–845 (2009).

119. Guo, S. & Liu, C. T. New glass forming ability criterion derived from cooling consideration. *Intermetallics* **18,** 2065–2068 (2010).

120. Inoue, A., Zhang, T. & Masumoto, T. Glass-forming ability of alloys. *Journal of Non-Crystalline Solids* **156–158,** 473–480 (1993).

121. Inoue, A., Zhang, T. & Takeuchi, A. Ferrous and Nonferrous Bulk Amorphous Alloys. *MSF* **269–272,** 855–864 (1998).

122. Greer, A. L. Confusion by design. *Nature* **366,** 303–304 (1993).

123. Inoue, A. & Takeuchi, A. Recent Progress in Bulk Glassy Alloys. *Mater. Trans.* **43,** 1892–1906 (2002).

124. Inoue, A. & Takeuchi, A. Recent progress in bulk glassy, nanoquasicrystalline and nanocrystalline alloys. *Materials Science and Engineering: A* **375–377,** 16–30 (2004).

125. Guo, F. Q., Poon, S. J. & Shiflet, G. J. Glass Formability in Al-based Multinary Alloys. *MSF* **331–337,** 31–42 (2000).

126. Xia, L., Li, W. H., Fang, S. S., Wei, B. C. & Dong, Y. D. Binary Ni–Nb bulk metallic glasses. *J. Appl. Phys.* 4 (2014).

127. Xu, D., Lohwongwatana, B., Duan, G., Johnson, W. L. & Garland, C. Bulk metallic glass formation in binary Cu-rich alloy series – Cu100−xZrx (x=34, 36, 38.2, 40 at.%) and mechanical properties of bulk Cu64Zr36 glass. *Acta Materialia* **52,** 2621–2624 (2004).

128. Guthrie, F. On Eutexia. *Proc. Phys. Soc. London* **6,** 124–146 (1884).

129. Edler, F., Kim, Y. G., Machin, G., Pearce, J. & White, D. R. Specialized Fixed Points above 0 °C, Guide on Secondary Thermometry. at (2017)

130. Cohen, M. H. & Turnbull, D. Composition Requirements for Glass Formation in Metallic and Ionic Systems. *Nature* **189,** 131–132 (1961).

131. Predel, B. Thermodynamic investigations on the formation and decomposition of metallic glasses. *Physica B+C* **103,** 113–122 (1981).

132. Boettinger, W. J. Growth Kinetic Limitations During Rapid Solidification. *MRS Proc.* **8,** 15 (1981).

133. Rawson, H. *Inorganic Glass-forming Systems*. (Academic Press, 1967).

134. Chen, H. S. Glassy metals. *Rep. Prog. Phys.* **43,** 353–432 (1980).

135. Minaev, V., Timoshenkov, S., Oblozhko, S. & Rodionov, P. Glass formation ability: Is the Rawson's 'liquidus temperature effect' always effective? *Journal of Optoelectronics and Advanced Materials* **6,** 791–798 (2004).

136. Wang, D., Li, Y., Sun, B. B., Sui, M. L., Lu, K. & Ma, E. Bulk metallic glass formation in the binary Cu–Zr system. *Appl. Phys. Lett.* **84,** 4029–4031 (2004).

137. Tan, H., Zhang, Y., Ma, D., Feng, Y. P. & Li, Y. Optimum glass formation at off-eutectic composition and its relation to skewed eutectic coupled zone in the La based La–Al–(Cu,Ni) pseudo ternary system. *Acta Materialia* **51,** 4551–4561 (2003).

138. Li, Y. Bulk metallic glasses: Eutectic coupled zone and amorphous formation. *JOM* **57,** 60–63 (2005).

139. Elliott, R. *Eutectic solidification processing: crystalline and glassy alloys*. (Butterworths, 1983).

140. Ma, D., Tan, H., Zhang, Y. & Li, Y. Correlation between Glass Formation and Type of Eutectic Coupled Zone in Eutectic Alloys. *Mater. Trans.* **44,** 2007–2010 (2003).

141. Suryanarayana, C. & Inoue, A. in *Ullmann's Encyclopedia of Industrial Chemistry* (ed. Wiley-VCH Verlag GmbH & Co. KGaA) a16_335.pub2 (Wiley-VCH Verlag GmbH & Co. KGaA, 2012). doi:10.1002/14356007.a16_335.pub2

142. Shechtman, D., Blech, I., Gratias, D. & Cahn, J. W. Metallic Phase with Long-Range Orientational Order and No Translational Symmetry. *Phys. Rev. Lett.* **53,** 1951–1953 (1984).

143. Haasen, P. & Mordike, B. L. *Physical Metallurgy, 3rd Edition*. (Cambridge University Press, 1996).

144. Li, C., Saida, J., Matsushita, M. & Inoue, A. Precipitation of icosahedral quasicrystalline phase in Hf65Al7.5Ni10Cu12.5Pd5 metallic glass. *Appl. Phys. Lett.* **77,** 528–530 (2000).

145. Hirata, A., Guan, P., Fujita, T., Hirotsu, Y., Inoue, A., Yavari, A. R., Sakurai, T. & Chen, M. Direct observation of local atomic order in a metallic glass. *Nature Mater* **10,** 28–33 (2011).

146. Hirata, A., Kang, L. J., Fujita, T., Klumov, B., Matsue, K., Kotani, M., Yavari, A. R. & Chen, M. W. Geometric Frustration of Icosahedron in Metallic Glasses. **341,** 5 (2013).

147. Nakamura, T., Matsubara, E., Imafuku, M., Koshiba, H., Inoue, A. & Waseda, Y. Structural Study of Amorphous FE70M10B20 (M=CR, W, NB, ZR and HF) Alloys by X-ray Diffraction. *Materials Transactions* **42,** 1530–1534 (2001).

148. Duwez, P., Willens, R. H. & Klement, W. Continuous Series of Metastable Solid Solutions in Silver-Copper Alloys. *Journal of Applied Physics* **31,** 1136–1137 (1960).

149. Anantharaman, T. R. & Suryanarayana, C. Review: A decade of quenching from the melt. *J Mater Sci* **6,** 1111–1135 (1971).

150. Schwarz, R. B. & Johnson, W. L. Formation of an Amorphous Alloy by Solid-State Reaction of the Pure Polycrystalline Metals. *Phys. Rev. Lett.* **51,** 415–418 (1983).

151. Chu, J. P., Liu, C. T., Mahalingam, T., Wang, S. F., O'Keefe, M. J., Johnson, B. & Kuo, C. H. Annealing-induced full amorphization in a multicomponent metallic film. *Phys. Rev. B* **69,** 113410 (2004).

152. Wei, X., Han, F., Wang, X., Wang, X. & Wen, C. Fabrication of Al-based bulk metallic glass by mechanical alloying and vacuum hot consolidation. *Journal of Alloys and Compounds* **501,** 164–167 (2010).

153. Suryanarayana, C. Mechanical alloying and milling. *Progress in Materials Science* 184 (2001).

154. Smith, D. *Thin-film Deposition: Principles and Practice*. (McGraw Hill, 1995).

155. Qing-Ming, C., Yu-Dian, F. & Heng-De, L. Amorphization of binary alloys by magnetron co-sputtering. *Materials Letters* **6,** 311–315 (1988).

156. Folch, A., Tejada, J., Peters, C. H. & Wrighton, M. S. Electron beam deposition of gold nanostructures in a reactive environment. 4

157. van Dorp, W. F. & Hagen, C. W. A critical literature review of focused electron beam induced deposition. *Journal of Applied Physics* **104,** 081301 (2008).

158. Nastasi, M., Saris, F. W., Hung, L. S. & Mayer, J. W. Stability of amorphous Cu/Ta and Cu/W alloys. *Journal of Applied Physics* **58,** 3052–3058 (1985).

159. Eason, R. *Pulsed Laser Deposition of Thin Films: Applications-Led Growth of Functional Materials*. (John Wiley & Sons, 2007).

160. Bloembergen, N. Fundamentals of laser-solid interactions. *AIP Conference Proceedings* **50,** 1–9 (1979).

161. Choy, K. Chemical vapour deposition of coatings. *Progress in Materials Science* **48,** 57–170 (2003).

162. Dobkin, D. M. & Zuraw, M. K. *Principles of Chemical Vapor Deposition*. (Springer Netherlands, 2003).

163. Ashby, M. & Greer, A. Metallic glasses as structural materials. *Scripta Materialia* **54,** 321–326 (2006).

164. Nishiyama, N., Amiya, K. & Inoue, A. Novel applications of bulk metallic glass for industrial products. *Journal of Non-Crystalline Solids* **353,** 3615–3621 (2007).

165. Jiang, Q. K., Liu, P., Ma, Y., Cao, Q. P., Wang, X. D., Zhang, D. X., Han, X. D., Zhang, Z. & Jiang, J. Z. Super elastic strain limit in metallic glass films. *Sci Rep* **2,** 852 (2012).

166. Inoue, A. Stabilization of metallic supercooled liquid and bulk amorphous alloys. *Acta Mater* 279 (2000).

167. Greer, A. L. Metallic glasses…on the threshold. *Materials Today* **12,** 14–22 (2009).

168. Yousfi, M. A., Panagiotopoulos, N. T., Jorge Junior, A. M., Georgarakis, K. & Yavari, A. R. Novel micro-flat springs using the superior elastic properties of metallic glass foils. *Scripta Materialia* **131,** 84–88 (2017).

169. Shiflet, G. J., Leng, Y. & Hawk, J. W. in *Ullmann's Encyclopedia of Industrial Chemistry* (Wiley-VCH Verlag GmbH & Co. KGaA, 2000).

170. Duwez, P. Structure and Properties of Glassy Metals. *Annual Review of Materials Science* **6,** 83–117 (1976).

171. Zeman, P., Zítek, M., Zuzjaková, Š. & Čerstvý, R. Amorphous Zr-Cu thin-film alloys with metallic glass behavior. *Journal of Alloys and Compounds* **696,** 1298–1306 (2017).

172. Cowell, E. W., Alimardani, N., Knutson, C. C., Conley, J. F., Keszler, D. A., Gibbons, B. J. & Wager, J. F. Advancing MIM Electronics: Amorphous Metal Electrodes. *Adv. Mater.* **23,** 74–78 (2011).

173. Kumar, G. & Schroers, J. Write and erase mechanisms for bulk metallic glass. *Appl. Phys. Lett.* **92,** 031901 (2008).

174. Yiu, P., Diyatmika, W., Bönninghoff, N., Lu, Y.-C., Lai, B.-Z. & Chu, J. P. Thin film metallic glasses: Properties, applications and future. *Journal of Applied Physics* **127,** 030901 (2020).

175. Kimura, H. & Masumoto, T. Fracture toughness of amorphous metals. *Scripta Metallurgica* **9,** 211–221 (1975).

176. Gilbert, C. J., Ritchie, R. O. & Johnson, W. L. Fracture toughness and fatigue-crack propagation in a Zr–Ti–Ni–Cu–Be bulk metallic glass. *Appl. Phys. Lett.* **71,** 476–478 (1997).

177. Lowhaphandu, P. & Lewandowski, J. J. Fracture toughness and notched toughness of bulk amorphous alloy: Zr-Ti-Ni-Cu-Be. *Scripta Materialia* **38,** 1811–1817 (1998).

178. Rafique, M. M. A. *Bulk metallic glasses and their composites: additive manufacturing and modeling and simulation*. (2018).

179. Greer, A. L., Cheng, Y. Q. & Ma, E. Shear bands in metallic glasses. *Materials Science and Engineering: R: Reports* **74,** 71–132 (2013).

180. Sun, B. A. & Wang, W. H. The fracture of bulk metallic glasses. *Progress in Materials Science* **74,** 211–307 (2015).

181. Hays, C. C., Kim, C. P. & Johnson, W. L. Microstructure Controlled Shear Band Pattern Formation and Enhanced Plasticity of Bulk Metallic Glasses Containing *in situ* Formed Ductile Phase Dendrite Dispersions. *Phys. Rev. Lett.* **84,** 2901–2904 (2000).

182. Hebert, R. J. in *Nanocrystal* (ed. Masuda, Y.) (IntechOpen, 2011).

183. Tian, L., Wang, X.-L. & Shan, Z.-W. Mechanical Behavior of Micronanoscaled Metallic Glasses. *Materials Research Letters* **4,** 63–74 (2016).

184. Yu, C.-C., Lee, C. M., Chu, J. P., Greene, J. E. & Liaw, P. K. Fracture-resistant thin-film metallic glass: Ultra-high plasticity at room temperature. *APL Materials* **4,** 116101 (2016).

185. Glushko, O., Mühlbacher, M., Gammer, C., Cordill, M. J., Mitterer, C. & Eckert, J. Exceptional fracture resistance of ultrathin metallic glass films due to an intrinsic size effect. *Sci Rep* **9,** 8281 (2019).

186. Hata, S., Sakurai, J. & Shimokohbe, A. Thin film metallic glasses as new mems materials. in *18th IEEE International Conference on Micro Electro Mechanical Systems, 2005. MEMS 2005.* 479–482 (IEEE, 2005).

187. Tammann, G. & Jenckel, E. Die Kristallisationsgeschwindigkeit und die Kernzahl des Glycerins in Abhängigkeit von der Temperatur. *Zeitschrift für anorganische und allgemeine Chemie* **193,** 76–80 (1930).

188. Tammann, G. Ueber die Abhängigkeit der Zahl der Kerne, welche sich in verschiedenen unterkühlten Flüssigkeiten bilden, von der Temperatur. *Zeitschrift für Physikalische Chemie* **25U,** 441–479 (1898).

189. Turnbull, D. Formation of Crystal Nuclei in Liquid Metals. *Journal of Applied Physics* **21,** 1022–1028 (1950).

190. Pound, G. M. & Mer, V. K. L. Kinetics of Crystalline Nucleus Formation in Supercooled Liquid Tin1,2. *J. Am. Chem. Soc.* **74,** 2323–2332 (1952).

191. Auer, S. & Frenkel, D. Prediction of absolute crystal-nucleation rate in hard-sphere colloids. *Nature* **409,** 1020–1023 (2001).

192. Dabenedetti, P. G. *Metastable Liquids: Concepts and Principles*. (Princeton University Press, 2020, 1997).

193. Pruppacher, H. R. & Klett, J. D. *Microphysics of Clouds and Precipitation*. (Kluwer Academic Publishers, 1997).

194. Kelton, K. F. A new model for nucleation in bulk metallic glasses. *Philosophical Magazine Letters* **77,** 337–344 (1998).

195. Assadi, H. & Schroers, J. Crystal nucleation in deeply undercooled melts of bulk metallic glass forming systems. *Acta Materialia* **50,** 89–100 (2002).

196. Wang, X.-L., Almer, J., Liu, C. T., Wang, Y. D., Zhao, J. K., Stoica, A. D., Haeffner, D. R. & Wang, W. H. In situ Synchrotron Study of Phase Transformation Behaviors in Bulk Metallic Glass by Simultaneous Diffraction and Small Angle Scattering. *Phys. Rev. Lett.* **91,** 265501 (2003).

197. Gránásy, L., Pusztai, T., Börzsönyi, T., Tóth, G., Tegze, G., Warren, J. A. & Douglas, J. F. Phase field theory of crystal nucleation and polycrystalline growth: A review. *Journal of Materials Research* **21,** 309–319 (2006).

198. Sekerka, R. F. in *Advances in Crystal Growth Research* (eds. Sato, K., Furukawa, Y. & Nakajima, K.) 21–41 (Elsevier Science B.V., 2001).

199. Gebauer, D., Kellermeier, M., Gale, J. D., Bergström, L. & Cölfen, H. Pre-nucleation clusters as solute precursors in crystallisation. *Chem. Soc. Rev.* **43,** 2348–2371 (2014).

200. M. Minić, D. & M. Vasić, M. in *Metallic Glasses* (eds. Minić, D. & Vasić, M.) (IntechOpen, 2020).

201. Suryanarayana, C. & Inoue, A. in *Ullmann's Encyclopedia of Industrial Chemistry* (Wiley-VCH Verlag GmbH & Co. KGaA, 2012).

202. Shiflet, G. J., Leng, Y. & Hawk, J. W. in *Ullmann's Encyclopedia of Industrial Chemistry* (ed. Wiley-VCH Verlag GmbH & Co. KGaA) a16_335 (Wiley-VCH Verlag GmbH & Co. KGaA, 2000). doi:10.1002/14356007.a16_335

203. Abrosimova, G. E., Zhukov, A. P. & Ponomarev, B. K. Effect of Heat Treatment on Some Properties of Fe- and Co-Based Amorphous Alloys. *Phys. Stat. Sol. (a)* **111,** K237–K241 (1989).

204. Cremaschi, V., Arcondo, B., Sirkin, H., Vázquez, M., Asenjo, A., Garcia, J. M., Abrosimova, G. & Aronin, A. Huge magnetic hardening ascribed to metastable crystallites during first stages of devitrification of amorphous FeSiBNbSn alloys. *J. Mater. Res.* **15,** 1936–1942 (2000).

205. Wang, G., Jiang, B., Zhang, X., Zhou, B., Meng, L., Wang, G., Jiang, B., Zhang, X., Zhou, B. & Meng, L. Crystallization Behavior and Mechanical Properties of Cu-based Bulk Metallic Glass Composites. *Materials Research* **22,** (2019).

206. Ketkaew, J., Liu, Z., Chen, W. & Schroers, J. Critical Crystallization for Embrittlement in Metallic Glasses. *Phys. Rev. Lett.* **115,** 265502 (2015).

207. Weeber, A. W. & Bakker, H. Amorphous Ni□Zr powders by milling the crystalline alloys. *Journal of the Less Common Metals* **141,** 93–102 (1988).

208. Lee, P. Y., Jang, J. & Koch, C. C. Amorphization by mechanical alloying: The role of mixtures of intermetallics. *Journal of the Less Common Metals* **140,** 73–83 (1988).

209. Lu, K., Wang, J. T. & Wei, W. D. A new method for synthesizing nanocrystalline alloys. *Journal of Applied Physics* **69,** 522–524 (1991).

210. Rastogi, P. K. & Duwez, P. Rate of crystallization of an amorphous Fe□P□C alloy. *Journal of Non-Crystalline Solids* **5,** 1–16 (1970).

211. Vitek, J. M., Vander Sande, J. B. & Grant, N. J. Crystallization of an amorphous Cu-Zr alloy. *Acta Metallurgica* **23,** 165–176 (1975).

212. Duhaj, P., Barančok, D. & Ondrejka, A. The study of transformation kinetics of the amorphous Pd□Si alloys. *Journal of Non-Crystalline Solids* **21,** 411–428 (1976).

213. Abrosimova, G. & Aronin, A. in *Progress in Metallic Alloys* (ed. Glebovsky, V.) (InTech, 2016).

214. Mukai, T., Suresh, S., Kita, K., Sasaki, H., Kobayashi, N., Higashi, K. & Inoue, A. Nanostructured Al–Fe alloys produced by e-beam deposition: static and dynamic tensile properties. *Acta Materialia* **51,** 4197–4208 (2003).

215. Cao, C. R., Huang, K. Q., Zhao, N. J., Sun, Y. T., Bai, H. Y., Gu, L., Zheng, D. N. & Wang, W. H. Ultrahigh stability of atomically thin metallic glasses. *Appl. Phys. Lett.* **105,** 011909 (2014).

216. Huang, K. Q., Cao, C. R., Sun, Y. T., Li, J., Bai, H. Y., Gu, L., Zheng, D. N. & Wang, W. H. Direct observation of atomic-level nucleation and growth processes from an ultrathin metallic glass films. *Journal of Applied Physics* **119,** 014305 (2016).

217. Wasa, K. & Hayakawa, S. *Handbook of sputter deposition technology*. (Noyes Publications, 1992).

218. Horwat, D., Dehmas, M., Aubry, E., Zollinger, J., Migot, S. & Pierson, J. F. Properties of nanocrystalline and nanocomposite WxZr1−x thin films deposited by co-sputtering. *Intermetallics* **17,** 421–426 (2009).

219. Ketov, S. V., Shi, X., Xie, G., Kumashiro, R., Churyumov, A. Y., Bazlov, A. I., Chen, N., Ishikawa, Y., Asao, N., Wu, H. & Louzguine-Luzgin, D. V. Nanostructured Zr-Pd Metallic Glass Thin Film for Biochemical Applications. *Scientific Reports* **5,** 7799 (2015).

220. Ketov, S. V., Joksimovic, R., Xie, G., Trifonov, A., Kurihara, K. & Louzguine-Luzgin, D. V. Formation of nanostructured metallic glass thin films upon sputtering. *Heliyon* **3,** e00228 (2017).

221. Chou, H. S., Huang, J. C. & Chang, L. W. Mechanical properties of ZrCuTi thin film metallic glass with high content of immiscible tantalum. *Surface and Coatings Technology* **205,** 587–590 (2010).

222. Tao, N. R., Sui, M. L., Lu, J. & Lua, K. Surface nanocrystallization of iron induced by ultrasonic shot peening. *Nanostructured Materials* **11,** 433–440 (1999).

223. Tao, N. R., Wang, Z. B., Tong, W. P., Sui, M. L., Lu, J. & Lu, K. An investigation of surface nanocrystallization mechanism in Fe induced by surface mechanical attrition treatment. *Acta Materialia* **50,** 4603–4616 (2002).

224. Li, F. C., Liu, T., Zhang, J. Y., Shuang, S., Wang, Q., Wang, A. D., Wang, J. G. & Yang, Y. Amorphous–nanocrystalline alloys: fabrication, properties, and applications. *Materials Today Advances* **4,** 100027 (2019).

225. H. R. Peng, M. M. Gong, Y. Z. Chen & F. Liu. Thermal stability of nanocrystalline materials: thermodynamics and kinetics: International Materials Reviews **62**, 303-333 (2017)

226. Higgins, G. T. Grain-Boundary Migration and Grain Growth. *null* **8,** 143–150 (1974).

227. Kumar, K. S., Van Swygenhoven, H. & Suresh, S. Mechanical behavior of nanocrystalline metals and alloys11The Golden Jubilee Issue—Selected topics in Materials Science and Engineering: Past, Present and Future, edited by S. Suresh. *Acta Materialia* **51,** 5743–5774 (2003).

228. Ma, E. Instabilities and ductility of nanocrystalline and ultrafine-grained metals. *Scripta Materialia* **49,** 663–668 (2003).

229. Meyers, M. A., Mishra, A. & Benson, D. J. Mechanical properties of nanocrystalline materials. *Progress in Materials Science* **51,** 427–556 (2006).

230. Bae, D. H., Lee, M. H., Kim, D. H. & Sordelet, D. J. Plasticity in Ni59Zr20Ti16Si2Sn3 metallic glass matrix composites containing brass fibers synthesized by warm extrusion of powders. *Appl. Phys. Lett.* **83,** 2312–2314 (2003).

231. Kim, Y.-H., Inoue, A. & Masumoto, T. Ultrahigh Mechanical Strengths of Al88Y2Ni10-xMx (M=Mn, Fe or Co) Amorphous Alloys Containing Nanoscale fcc-Al Particles. *Materials Transactions, JIM* **32,** 599–608 (1991).

232. Inoue, A., Tomioka, H. & Masumoto, T. Mechanical properties of ductile Fe-Ni-Zr and Fe-Ni-Zr (Nb or Ta) amorphous alloys containing fine crystalline particles. *J Mater Sci* **18,** 153–160 (1983).

233. Kim, Y. H., Hiraga, K., Inoue, A., Masumoto, T. & Jo, H. H. Crystallization and High Mechanical Strength of Al-Based Amorphous Alloys. *Materials Transactions, JIM* **35,** 293–302 (1994).

234. Choi, G. S., Kim, Y. H., Cho, H. K., Inoue, A. & Masumoto, T. Ultrahigh tensile strength of amorphous Al-Ni-(Nd,Gd)-Fe alloys containing nanocrystalline Al particles. *Scripta Metallurgica et Materialia* **33,** 1301–1306 (1995).

235. Kim, Y.-H., Inoue, A. & Masumoto, T. Increase in Mechanical Strength of Al–Y–Ni Amorphous Alloys by Dispersion of Nanoscale fcc-Al Particles. *Materials Transactions, JIM* **32,** 331–338 (1991).

236. Fan, C. & Inoue, A. Improvement of Mechanical Properties by Precipitation of Nanoscale Compound Particles in Zr–Cu–Pd–Al Amorphous Alloys. *Materials Transactions, JIM* **38,** 1040–1046 (1997).

237. Fan, C. & Inoue, A. Improvement of Mechanical Properties by Precipitation of Nanoscale Compound Particles in Zr–Cu–Pd–Al Amorphous Alloys. *Materials Transactions, JIM* **38,** 1040–1046 (1997).

238. Fan, C., Takeuchi, A. & Inoue, A. Preparation and Mechanical Properties of Zr-based Bulk Nanocrystalline Alloys Containing Compound and Amorphous Phases. *Materials Transactions, JIM* **40,** 42–51 (1999).

239. Diserens, M., Patscheider, J. & Lévy, F. Improving the properties of titanium nitride by incorporation of silicon. *Surface and Coatings Technology* **108–109,** 241–246 (1998).

240. Pavlatou, E. A., Stroumbouli, M., Gyftou, P. & Spyrellis, N. Hardening effect induced by incorporation of SiC particles in nickel electrodeposits. *J Appl Electrochem* **36,** 385–394 (2006).

241. Diserens, M., Patscheider, J. & Lévy, F. Mechanical properties and oxidation resistance of nanocomposite TiN–SiNx physical-vapor-deposited thin films. *Surface and Coatings Technology* **120–121,** 158–165 (1999).

242. Raub, E. Die hegierungen der Platinmetalle mit Molybdan. *Ztsch. tilT Metallkunde* **45,** 23 (1954).

243. Bloom, D. S. Sigma Phase in the Molybdenum-Ruthenium System. *JOM* **7,** 420–420 (1955).

244. Grånäs, O., Korzhavyi, P. A., Kissavos, A. E. & Abrikosov, I. A. Theoretical study of the Mo–Ru sigma phase. *Calphad* **32,** 171–176 (2008).

245. Anderson, E. & Hume-Rothery, W. The equilibrium diagram of the system molybdenum-ruthenium. *Journal of the Less Common Metals* **2,** 443–450 (1960).

246. Kleykamp, H. The constitution of the Mo Ru system. *Journal of the Less Common Metals* **136,** 271–275 (1988).

247. Collver, M. M. & Hammond, R. H. Superconductivity in 'Amorphous' Transition-Metal Alloy Films. *Phys. Rev. Lett.* **30,** 92–95 (1973).

248. Wall, R. N., Basch, D. R. & Jacobson, D. L. High-temperature spectral emissivity of several refractory elements and alloys. *JMEP* **1,** 679–684 (1992).

249. Bajt, S., Dai, Z. R., Nelson, E. J., Wall, M. A., Alameda, J., Nguyen, N., Baker, S., Robinson, J. C., Taylor, J. S., Clift, M., Aquila, A., Gullikson, E. M. & Edwards, N. V. G. Oxidation resistance of Ru-capped EUV multilayers. in (ed. Mackay, R. S.) 118 (2005). doi:10.1117/12.597443

250. Naulleau, P. P., Liddle, J. A., Salmassi, F., Anderson, E. H. & Gullikson, E. M. Design, fabrication, and characterization of high-efficiency extreme-ultraviolet diffusers. *Appl. Opt.* **43,** 5323 (2004).

251. Bramman, J. I., Sharpe, R. M., Thom, D. & Yates, G. Metallic fission-product inclusions in irradiated oxide fuels. *Journal of Nuclear Materials* **25,** 201–215 (1968).

252. Jahanmir, S., Abrahamson, E. P. & Suh, N. P. Sliding wear resistance of metallic coated surfaces. *Wear* **40,** 75–84 (1976).

253. Kondratiuk, J. & Kuhn, P. Tribological investigation on friction and wear behaviour of coatings for hot sheet metal forming. *Wear* **270,** 839–849 (2011).

254. Cihan, E., Störmer, H., Leiste, H., Stüber, M. & Dienwiebel, M. Low friction of metallic multilayers by formation of a shear-induced alloy. *Sci Rep* **9,** 9480 (2019).

255. Yang, G. & Park, S.-J. Deformation of Single Crystals, Polycrystalline Materials, and Thin Films: A Review. *Materials* **12,** 2003 (2019).

256. O'Connor, B., Haughn, C., An, K.-H., Pipe, K. P. & Shtein, M. Transparent and conductive electrodes based on unpatterned, thin metal films. *Appl. Phys. Lett.* **93,** 223304 (2008).

257. Zhang, C., Zhao, D., Gu, D., Kim, H., Ling, T., Wu, Y.-K. R. & Guo, L. J. An Ultrathin, Smooth, and Low-Loss Al-Doped Ag Film and Its Application as a Transparent Electrode in Organic Photovoltaics. *Adv. Mater.* **26,** 5696–5701 (2014).

258. Johnson, W. L. Bulk Glass-Forming Metallic Alloys: Science and Technology. *MRS Bull.* **24,** 42–56 (1999).

259. Wang, W. Roles of minor additions in formation and properties of bulk metallic glasses. *Progress in Materials Science* **52,** 540–596 (2007).

260. Guo, S., Hu, Q., Ng, C. & Liu, C. T. More than entropy in high-entropy alloys: Forming solid solutions or amorphous phase. *Intermetallics* **41,** 96–103 (2013).

261. Wagner, C. & Harned, N. Lithography gets extreme. *Nature Photon* **4,** 24–26 (2010).

262. Spiller, E. A., Baker, S. L., Parra, E. & Tarrio, C. Smoothing of mirror substrates by thin-film deposition. in (eds. MacDonald, C. A., Goldberg, K. A., Maldonado, J. R., Chen-Mayer, H. H. & Vernon, S. P.) 143–153 (1999).

263. Yoon, H. W., Lee, H. C., Shin, S. Y., Kwon, S. H. & Moon, K. I. Preparation of Zr-Al-Mo-Cu Single Targets with Glass Forming Ability and Deposition of Thin Film Metallic Glass. *Coatings* **10,** 398 (2020).

264. Grånäs, O., Korzhavyi, P. A., Kissavos, A. E. & Abrikosov, I. A. Theoretical study of the Mo–Ru sigma phase. *Calphad* **32,** 171–176 (2008).

265. Gingrich, N. S. The Diffraction of X-Rays by Liquid Elements. *Rev. Mod. Phys.* **15,** 90–110 (1943).

266. Braeckman, B. R. & Depla, D. On the amorphous nature of sputtered thin film alloys. *Acta Materialia* **109,** 323–329 (2016).

267. Bajt, S., Alameda, J., Jr, T. B., Clift, W. M., Folta, J. A., Kaufmann, B. & Spiller, E. Improved reflectance and stability of Mo/Si multilayers. **4506,** 11

268. Bajt, S., Chapman, H. N., Nguyen, N., Alameda, J., Robinson, J. C., Malinowski, M., Gullikson, E., Aquila, A., Tarrio, C. & Grantham, S. Design and performance of capping layers for extreme-ultraviolet multilayer mirrors. *Appl. Opt.* **42,** 5750 (2003).

269. Platschorre, L. *Tremani*. at <https://tremani.nl/over-ons>

270. Rodriguez-Tinoco, C., Gonzalez-Silveira, M., Ramos, M. A. & Rodriguez-Viejo, J. Ultrastable glasses: new perspectives for an old problem. *Riv. Nuovo Cim.* **45,** 325–406 (2022).

271. Gibbs, J. H. & DiMarzio, E. A. Nature of the Glass Transition and the Glassy State. *The Journal of Chemical Physics* **28,** 373–383 (1958).

272. Tool, A. Q. Effect of heat-treatment on the density and constitution of high-silica glasses of the borosilicate type*. *J American Ceramic Society* **31,** 177–186 (1948).

273. Kaur, A., Khanna, A., Kaur, A., Hirdesh, Gonzàlez-Barriuso, M. & Gonzàlez, F. Effects of annealing on density, glass transition temperature and structure of tellurite, silicate and borate glasses. *Journal of Non-Crystalline Solids* **500,** 443–452 (2018).

274. Troglia, A., van Vliet, S., Yetik, G., Wakil, I. E., Momand, J., Kooi, B. J. & Bliem, R. Free-standing nanolayers based on Ru silicide formation on Si(100). *Phys. Rev. Materials* **6,** 043402 (2022).

275. Louzguine-Luzgin, D. V. Early stage crystallization kinetics in metallic glass-forming alloys. *Journal of Alloys and Compounds* **586,** 216–219 (2014).

276. Köster, U. Surface crystallization of metallic glasses. *Materials Science and Engineering* **97,** 233–239 (1988).

Summary

One of the elements of modern technology that plays an ever more important role in our society is formed by microchips. To date, these integrated circuits are essential components of nearly every technological product. Further increases in microchip process power require continued miniaturization of the dimensions of the transistors that make up these devices. This is currently achieved by state-of-the-art photolithography machines that make use of extreme ultraviolet (EUV) light. These machines establish one of the most advanced technologies, ever developed. Their complexity is accompanied by a number of scientific challenges that need to be addressed in the context of further developments. Some of these concern the multilayer mirrors and pellicles. These critical, optical components consist of stacks of ultrathin layers of materials of no more than a few nanometers thickness. The harsh operating conditions within the lithography machines, in particular the cocktail of highly energetic EUV photons and hydrogen gas plus the resulting plasma, can lead to progressive degradation of these thin-layer components. Unraveling these degradation phenomena requires basic surface- and material-science investigations at the very forefront of our current knowledge.

The optical lifetime of EUV mirrors and pellicles forms the motivation for the particular focus in this thesis on nanolayers made of Si, Mo and Ru. We concentrated on the thermal consequences of the operation conditions on the stability of these materials. On the nanometer and the atomic scale, this requires us to understand *dewetting*, the phenomenon that a layered structure breaks up into agglomerates. We combine our investigations with a keen eye for potential solutions.

In Chapter 2, I investigate the thermal evolution of ultra-thin nanolayers of elemental Mo and Ru as well as bilayers of Ru on top of Mo on Si(100) substrates with a native oxide. While Ru nanolayers already show the first signs of dewetting, in the form of hole formation, at 600°C, Mo thin films are found to exhibit somewhat better thermal stability and only dewet at 800°C. Based on its infrared optical properties and its good resistance against oxidation, Ru top layer is required for application in many EUV optics elements. In an attempt to implement the benefits of both materials, Ru and Mo, we introduce an ultrathin Mo film as an interlayer between a Ru top layer and a naturally oxidized Si wafer. As we hoped, the silicide formation at the Mo-Si interface provides a better adhesion that improves the thermal stability, not only of an individual Mo nanolayer but also of the Ru-on-Mo bilayer. We further find that both the elemental Mo nanolayers and the bilayer thin films exhibit unusual morphologies after annealing to sufficiently high temperatures. For the individual Mo-layer and bilayer systems, we observe structures that we refer to as double-layer dewetting and nano-flowers, respectively.

On a microscopic scale, metal films are usually polycrystalline, i.e. they consist of crystalline grains that are each internally ordered but all have different orientations. The macroscopic film properties are often affected or even dominated by the boundaries between these grains that influence the thermal, chemical and mechanical properties and stability of polycrystalline layers. A simple but effective structural alternative, a metallic glass, should avoid the detrimental effects of grain boundaries, simply by avoiding crystallinity altogether. In Chapter 3, I provide an overview of the thermodynamic considerations that are used to interpret the thermal evolution of amorphous and polycrystalline materials. While the non-equilibrium character of glassy arrangements makes these very difficult to achieve and maintain for pure, elemental metals, they can be obtained for a number of metal alloys, for example by applying extremely high cooling rates from the melt.

In Chapter 4, I show that an amorphous arrangement can be achieved readily for a binary metal alloy of Mo and Ru, by employing the straightforward, industrial technique of sputter deposition. We find that the amorphous films display superior smoothness with respect to traditional, polycrystalline films. Finally, in Chapter 5, I demonstrate that the thermal stability of the amorphous alloy films is surprisingly good, qualifying them as a promising material to consider for a variety of applications.

Samenvatting

Een van de elementen van moderne technologie die een steeds belangrijkere rol speelt in onze samenleving wordt gevormd door microchips. Tegenwoordig zijn deze geïntegreerde schakelingen essentiële componenten van bijna elk technologisch product. Verdere verbetering van de rekenkracht van microchips vereist voortdurende miniaturisatie van de afmetingen van de transistoren, waaruit deze bestaan. Dit wordt momenteel bereikt door ultramoderne fotolithografiemachines die gebruik maken van extreem ultraviolet (EUV) licht. Deze machines vertegenwoordigen een van de meest geavanceerde technologieën die ooit zijn ontwikkeld. Hun complexiteit komt met een aantal wetenschappelijke uitdagingen die moeten worden aangegaan om verdere ontwikkelingen mogelijk te maken. Sommige hiervan hebben betrekking op de multilaag-spiegels en de zogenaamde 'pellicles'. Deze essentiële, optische componenten bestaan uit stapelingen van ultradunne materiaallagen, elk niet meer dan enkele nanometers dik. De aggressieve bedrijfsomstandigheden in de lithografiemachines, met name de cocktail van hoogenergetische EUV-fotonen en waterstofgas plus het resulterende plasma, kunnen leiden tot voortschrijdende degradatie van deze dunnelaag-componenten. Het ontrafelen van deze degradatieverschijnselen vereist fundamenteel oppervlakte- en materiaalwetenschappelijk onderzoek aan de grens van onze huidige kennis**.**

De optische levensduur van EUV-spiegels en -pellicles vormt de motivatie voor de specifieke focus in dit proefschrift op nanolagen gemaakt van Si, Mo en Ru. We concentreren ons op de thermische gevolgen van de bedrijfs-omstandigheden op de stabiliteit van deze materialen. Op de nanometer- en de atomaire schaal vereist dit dat we *ontvochtiging* (Eng. dewetting) begrijpen, het verschijnsel dat een gelaagde structuur uiteenvalt in agglomeraten. We combineren ons onderzoek met een scherp oog voor mogelijke oplossingen.

In Hoofdstuk 2 onderzoek ik de thermische evolutie van ultradunne nanolagen van elementair Mo en Ru, evenals dubbellagen van Ru bovenop Mo op Si(100)-substraten met een natuurlijk oxide. Terwijl Ru-nanolagen al de eerste tekenen van ontvochtiging vertonen, via de vorming van gaatjes, bij 600°C, blijken Mo dunne films een wat betere thermische stabiliteit te vertonen en pas te ontvochtigen bij 800°C. Op basis van zijn infrarood-optische eigenschappen en zijn goede weerstand tegen oxidatie, is een Ru toplaag vereist voor toepassing in veel EUV-optische elementen. In een poging om de voordelen van beide materialen, Ru en Mo, te combineren, introduceren we een ultradunne Mo-film als tussenlaag tussen een Ru-toplaag en een natuurlijk geoxideerde Si-plak. Zoals we hoopten, zorgt de vorming van silicide op het Mo-Si-grensvlak voor een betere hechting die de thermische stabiliteit verbetert, niet alleen van een individuele Mo-nanolaag, maar ook van de

Ru-op-Mo-dubbellaag. We vinden verder dat zowel de elementaire Mo-nanolagen als de tweelagige dunne films ongebruikelijke morfologieën vertonen na verhitting tot voldoende hoge temperaturen. Voor de individuele Mo-laag en het dubbellaagsysteeem nemen we structuren waar, die we respectievelijk dubbellaag-ontvochtiging noemen en nanobloemen.

Op microscopische schaal zijn metaalfilms meestal polykristallijn, d.w.z. ze bestaan uit kristallijne korrels die elk intern geordend zijn maar allemaal verschillende oriëntaties hebben. De macroscopische eigenschappen van zo'n metaallaag worden vaak beïnvloed of zelfs gedomineerd door de grenzen tussen deze korrels die de thermische, chemische en mechanische eigenschappen en stabiliteit van polykristallijne lagen beïnvloeden. Een eenvoudig maar effectief structureel alternatief, een metallisch glas, zou de schadelijke effecten van korrelgrenzen moeten vermijden, simpelweg door kristalliniteit helemaal te vermijden. In Hoofdstuk 3 geef ik een overzicht van de thermodynamische overwegingen die worden gebruikt om de thermische evolutie van amorfe en polykristallijne materialen te interpreteren. Hoewel het niet-evenwichtskarakter van glasachtige structuren het zeer moeilijk maakt om deze te bereiken en handhaven voor zuivere, elementaire metalen, kunnen ze voor een aantal metaallegeringen worden verkregen, bijvoorbeeld door extreem hoge afkoelsnelheden uit de smelt toe te passen.

In Hoofdstuk 4 laat ik zien dat een amorfe structuur gemakkelijk kan worden bereikt voor een binaire metaallegering van Mo en Ru, door gebruik te maken van de industriële standaardtechniek van sputterdepositie. We vinden dat de amorfe films een superieure gladheid vertonen in vergelijking met traditionele, polykristallijne films. Tot slot laat ik in Hoofdstuk 5 zien dat de thermische stabiliteit van de amorfe legeringsfilms verrassend goed is, hetgeen ze kwalificeert als een veelbelovend materiaal om in overweging te nemen voor een verscheidenheid aan toepassingen.

List of publications

This thesis is based on the following publications:

- **G. Yetik**, C. Sfiligoj, J.W.M. Frenken, The influence of a molybdenum interlayer on the wetting properties of ruthenium thin films. In preparation (2023). (Chapter 2)

- **G. Yetik**, A. Troglia, S. Farokhipoor, S. van Vliet, J. Momand, B.J. Kooi, R. Bliem, J.W.M. Frenken, Ultrathin, sputter-deposited, amorphous alloy films of ruthenium and molybdenum. Surface and Coatings Technology 445, 128729 (2022). (Chapter 4)

- **G. Yetik**, A. Troglia, S. Farokhipoor, S. van Vliet, J. Momand, B.J. Kooi, R. Bliem, J.W.M. Frenken, Thermal stability of amorphous ruthenium and molybdenum alloys.. In preparation (2023). (Chapter 5)

The author contributed to the following publications:

- Ö. Sağlam, **G. Yetik**, J. Reichert, J. V. Barth, A. C. Papageorgiou, On-surface reaction of tetraphenylporphyrins with $Os_3(CO)_{12}$ precursors and Os clusters: A scanning tunneling microscopy investigation.
  Surface Science 646, 396028 (2016).

- A. Troglia, S. van Vliet, **G. Yetik**, I. El Wakil J. Momand, B.J. Kooi, R. Bliem, Freestanding nanolayers based on Ru silicide formation on Si(100). Phys. Rev. Materials 6, 043402 (2022).

Acknowledgments

After a long and challenging journey, I have reached the finish line, and I am grateful to have had the support of so many remarkable individuals who made this research possible.

First and foremost, I express my deepest gratitude to my supervisor, Joost. Your guidance and unwavering optimism have been invaluable throughout this endeavor. Despite the numerous obstacles encountered, your support has consistently motivated and inspired me. Your profound knowledge and extensive experience have equipped me for this remarkable journey. Our meaningful and extensive discussions have contributed immensely to my growth. I am also incredibly fortunate to be a part of the ARCNL family, and I extend my heartfelt appreciation to our director, Joost, and manager, Marjan. Marjan, your enduring presence and strong support have made a significant impact on everyone. I would also like to extend special thanks to my co-supervisor, Roland. I am delighted that you joined ARCNL during my final years, and I am grateful for your support throughout my research. Your analysis and feedback have been instrumental in shaping my work.

I would like to express my deepest gratitude to Silvester for his instrumental role in introducing me to ASML research and engaging in insightful discussions throughout this journey. One chapter of this thesis would not have been possible without our fruitful collaboration. I am also grateful to Arend-Jan for being my reliable partner whenever there were issues in the lab or with the setup. Jan, your discussions and knowledge transfer have been immensely valuable. Special thanks go to Cristina, my paranymph. Being in the same group as you has been an incredible experience. You have not only been a colleague but also a dear friend. Throughout the highs and lows of this journey, we stood together, and I sincerely appreciate your unshaken support as my paranymph, as well as your assistance in analyzing my AFM data. And let's not forget the friendly and sweet competition we shared. Ale, I am overjoyed that you joined ARCNL. Working with you has been a pleasure, and I thank you for your contributions to this research, particularly in the XPS measurements and analysis. Your presence as my paranymph is also greatly appreciated. I would like to extend my thanks to the entire Nanolayers group for creating an inspiring and stimulating research environment. I would also like to extend my sincere thanks to Dirk for his support during the kick-off phase of this journey. I am grateful for the knowledge transfer on VT-STM, even though it may not be directly related to this thesis. Your assistance has been invaluable in broadening my understanding and enhancing my research experience.

Lastly, I extend my gratitude to Wim, the new director of ARCNL, for facilitating a smooth end to my PhD journey through your enthusiasm and support. I would also like to express my appreciation to all the staff members at ARCNL and AMOLF for their friendly support. I am deeply thankful to my friends and family for their continuous support throughout this journey.